CLOUD AND ICE IN THE PLANETARY SCALE CIRCULATION AND IN CLIMATE

Final Report

(1 January 1977 - 30 January 1983)

for

National Aeronautics and Space Administration

Grant NSG-5152

by

Co-Principal Investigators

David D. Houghton
John E. Kutzbach
Verner E. Suomi

Principal Scientist

Gerald F. Herman

(NASA-CR-173992) CLOUD AND ICE IN THE PLANETARY SCALE CIRCULATION AND IN CLIMATE Final Report, 1 Jan. 1977 - 30 Jan. 1983 (Wisconsin Univ.) 96 p HC A05/MF A01 CSCL 03B

N84-35244

Unclas G3/91 23149

SUMMARY

During the period 1 January 1977 - 30 January 1983 research was conducted to investigate 1) The role of sea ice in weather and climate, and 2) The nature of cloud-radiative interactions in the general circulation. The principal accomplishments of this research were

1) The execution and analysis of GCM experiments to understand the role of clouds in climate.
2) The development of a parameterization for infrared radiation in the presence of partial cloudiness.
3) Analysis of the high latitude climatology of the GLAS GCM.
4) The design, execution, and analysis of general circulation model (GCM) experiments which illustrated the role of Arctic sea ice anomalies in climate variability.
5) The execution of experiments with a coupled sea ice model to determine the adequacy of both the ice and atmospheric models for climate simulations.
6) A review of the cloud and radiation budgets for several of the GLAS second order GCMs.
7) Contributions toward the planning of a major Arctic field program.
8) A series of GCM experiments investigating the dynamics of the Siberian High.
9) Analysis of winter and summer simulation with the GLAS GCM.

During the period of the grant the principal scientist (Dr. G.F. Herman) was jointly a Faculty Research Associate at the Goddard Laboratory for Atmospheric Science, and a regular faculty member in the University of Wisconsin Meteorology Department.

1. INTRODUCTION

The research carried out under NASA NSG-5152 was done so with two objectives in mind. The principal objective was to conduct a long-term, in depth study of two aspects of climate dynamics, namely, the respective roles of the cryosphere, and of cloud-radiative interactions. The secondary objective was to establish a collaborative relationship between the modeling group at GLAS and the University of Wisconsin Meteorology Department. This report documents our progress in attacking several important issues involving clouds and ice in the climate system. It is somewhat more difficult to gauge the net benefits that accrued to GLAS and to the U.W. Meteorology Department from this collaborative program. However, the large number of publications by Wisconsin scientists that grew out of the initial contact made through this program is a clear indication of the program's net impact.

2. DISCUSSION OF SCIENTIFIC RESULTS

A. Cloud-radiative interactions

The principal objective of the cloud radiation research has been to understand the modes of interaction ("feedback") between radiative transfer, cloud formation, and atmospheric dynamics. The problem areas that were investigated are the following:

i. Infrared and solar radiation feedback in climate simulations

The interaction between global cloudiness and the solar and infrared components of the earth's radiation budget was studied in general circulation model experiments with a version of the GLAS GCM (see Herman et al., 1980). A wintertime simulation was conducted in which cloud radiative transfer calculations used realistic cloud optical properties, and were fully interactive with model-generated cloudiness. This simulation was compared with others in which the clouds were

alternatively non-interactive with respect to the solar or thermal radiation calculations. Other cloud processes (formation, latent heat release, precipitation, vertical mixing) were accurately simulated in these experiments.

It was concluded that on a global basis clouds increased the global radiation balance by 40 W m^{-2} by absorbing longwave radiation, but decreased it by 56 W m^{-2} by reflecting solar radiation to space. The net cloud effect was therefore a reduction of the radiation balance by 16 W m^{-2}, and was dominated by the cloud albedo effect.

It is possible to draw inferences about the nature of global cloud feedback mechanisms from the changes in cloud frequency and distribution in the transparent cloud experiments. Over oceans, both convective and stratiform clouds behaved as positive feedback components. Since ocean surface temperatures were fixed, an increase in cloudiness reduced the radiation balance (and thus the temperature) of the atmosphere relative to the ocean surface because of the dominating cloud albedo effect. This, in turn, enhanced convection and evaporation, and caused more clouds to form. Over land, convective clouds behaved as a negative feedback component since their formation decreased the radiation balance of the surface, which suppressed convection and evaporation, and was unfavorable for further cloud development.

Cloud effects on the Siberian High. It was also demonstrated in GCM experiments that the strength of the Siberian high was dependent on the cloud cover of the northeast Soviet Union. Maintenance of the high was strongly affected by the radiatively-generated dome of cold air near the surface, which formed or dissipated as the cloud cover decreased or increased.

B. Fractional cloudiness and variable cloud emissivity

The analysis of the cloud-radiation experiments clearly pointed to the fact that the average infrared opacity of the GLAS model atmosphere was too large. This was attributed to two factors: First, since all model clouds,

including those which were intended to represent cirrus clouds, were assumed to have unit emissivity (zero transmissivity), the model did not transmit enough longwave radiation to space. Second, all model clouds, including those intended to represent subgrid scale cumulus convection, were assumed in the radiation calculation to occupy the entire 4° latitude by 5° longitude grid area. The net result of both of these features of the radiation calculation was to maintain an unrealistically positive global radiation balance.

A solution to this problem was developed in collaboration with V. Krishnamurthy (see Appendix) which provided a more realistic treatment of the cloud infrared optical properties. A parameterization was developed based on the multiplicative property of cloud and gas transmissivities which allowed the variable emissivity of cirrus clouds, and the fractional cloud amounts of other cloud types to be specified. There was a significant improvement in the model's infrared radiation balance when these changes were implemented in test runs.

C. High latitude model climatology

The sensitivity of the circulation to high latitude boundary conditions raised a further question concerning general circulation modelling strategy: Are general circulation models reliable tools for investigating climatic processes at high latitudes? Are fully-coupled ice-atmosphere-ocean models feasible constructs in view of all of the known limitations of ice, atmospheric, and oceanic circulation models?

To answer the questions of model reliability, the performance of a version of the general circulation model used at GLAS was evaluated with particular emphasis on its behavior at high latitudes of the Northern and Southern Hemispheres (see Herman and Johnson, 1980). A January-February climatology for the model was constructed by averaging eight 30-day means, each of which spanned

the period from 15 January to 14 February. A mean July climatology was similarly defined on the basis of seven 30-day averages, each spanning the period 1-31 July.

Model-generated sea level pressure, 500 mb geopotential, and surface air temperature were compared with observed long-term climatologies. Sensible heat, evaporative, and radiative fluxes at the surface, and radiative fluxes at the top of the atmosphere also were compared with observed data.

In the Northern Hemisphere the major features that were satisfactorily simulated included the position and intensity of the Aleutian and Icelandic lows in winter; the central Arctic pressure distribution during winter and summer; and the summertime North Atlantic and North Pacific high pressure regimes. Sensible and evaporative heat fluxes and radiation budget parameters were not unreasonable, but a rigorous comparison was difficult because of data deficiencies. The most notable shortcomings of the model included its weak wintertime Asiatic high, and missing meridionality of the 500 mb flow over the North Pacific.

The GCM was less successful in simulating the observed climatology of the Southern Hemisphere. The 500 mb circumpolar flow was adequate, but the model did not successfully reproduce the stationary low pressure centers at the surface around the Antarctic continent. Simulated energy flux components did not disagree in any substantial way with the sparse observations that exist.

On the basis of this analysis it was concluded that there were no significant limitations to using the model in high latitude sensitivity studies. However, the systematic errors in surface temperature and radiation conditions raise concerns about the GCM's ability to provide accurate thermodynamic forcing for a sea ice model.

D. Ice margin sensitivity experiments

Relationships between ice distribution anomalies and atmospheric anomalies had been suggested since the beginning of this century. More recent studies have confirmed some correlations between the two anomalies on scales ranging from the synoptic to the hemispheric. An important scientific question that remained concerned cause and effect: Was it the sea ice anomalies which caused the atmospheric anomalies, or vice versa?

Herman and Johnson (1978) imposed observed ice margin variations in a monthly climatic simulation and concluded that ice margin anomalies were capable of altering local climates in certain regions of the high and mid-latitudes, and that there was the possibility of interactions between high latitudes and subtropical regions.

The GCM experiments of Fletcher et al., Warshaw and Rapp, and Williams et al. imposed catastrophic variations of ice extent (e.g., complete removal of the Arctic ice cover, or ice age conditions). A basic question that arose in applying GCM's to the study of the atmosphere's response to seasonal ice anomalies was whether the signal produced by these relatively small anomalies could be distinguished above the natural variability in the model caused by baroclinic, barotropic, and convective instabilities.

To perform an initial sensitivity test of the model, two different January-February climatologies were computed with hypothetical maximum and minimum sea ice conditions in the north and south polar regions (Herman and Johnson, 1980). The imposed differences were less extreme than the complete removal of all Arctic ice, but were approximately twice as large as observed year-to-year variations. Large differences were obtained between the two climatologies: In the Northern Hemisphere zonally-averaged temperatures were up to 5°C cooler in the lower troposphere between 50°N and 70°N, the vertically-integrated eddy

energy flux was approximately 13% greater at 50°N with maximum ice conditions. In the surface energy balance, sensible and latent heat fluxes and the solar radiation absorbed at the surface were greatly reduced where the ice margin was increased. With the maximum ice, storage terms in the atmospheric energy cycle were increased up to 10%, and conversion terms up to 17%, although these differences are smaller than the uncertainty associated with their calculation from observations. There were also local differences in the 500 mb geopotential height field and 850 mb temperature field that were more than twice as large as the standard deviations of these fields obtained in GCM predictability experiments. It was concluded that the calculated differences between model simulations for the two ice conditions were greater than the inherent variability of the model.

The next step was to test the model's sensitivity to realistic variations of sea ice conditions, and to examine critically the statistical reliability of the results. A set of experiments was thus conducted (see Herman and Johnson, 1978; 1979) to test the influence on the model climatology of sea ice variations based on recent observations. A control was defined as the mean of six January-February simulations with ice boundaries corresponding to climatologically minimum ice cover occurring simultaneously in the Davis Strait, East Greenland Sea, Barents Sea, Sea of Okhotsk, and Bering Sea. An anomaly was similarly defined as the mean of two simulations with maximum ice conditions occurring simultaneously in the same regions. (The extremes were estimated from 17 years of observed conditions in the Atlantic sector, and from five years of data in the Pacific sector.)

When sea ice boundaries were at their maximum extent the following differences resulted in the January-February climatology as compared with minimum boundaries: Sea level pressure was higher by as much as 8 mb over the Barents

Sea, by more than 4 mb in Davis Strait, and by slightly less than 4 mb in the Sea of Okhotsk. Pressure was lower by as much as 8 mb in the North Atlantic between Iceland and the British Isles, and in the Gulf of Alaska. Pressure rises of as much as 4 mb in the eastern subtropical regions of the North Atlantic and North Pacific accompanied pressure falls in the Gulf of Alaska and Icelandic region. Pressure also increased over the Mediterranean region. Geopotential heights at 700 mb were more than 80 gpm lower in the Gulf of Alaska, and more than 100 gpm lower in the Icelandic region. Changes of opposite sign occurred over the subtropics. Zonally averaged temperatures were cooler by 2°C below 800 mb between 50 and 70°N with little change elsewhere. The poleward flux of total energy was a maximum of 13% greater between latitudes 40 and 53°N.

The computed 700 mb geopotential differences were more than twice the inherent variability or "noise" of the model over a broad region of the North Pacific, and between Iceland and the British Isles. Pressure differences were more than twice the inherent variability in the Davis Strait, Gulf of Alaska and Barents Sea, and in the eastern subtropical Atlantic and Pacific. Statistical significance of zonally averaged differences was largest between 50 and 70°N where the confidence levels were as follows: for geopotential height differences, 99% (850 mb), 99% (77 mb) and 97% (500 mb); for temperature, 97% (850 mb) and 92% (700 mb); and sea level pressure, 94%. Confidence levels were high for changes in the Azores region.

On the basis of model results it was concluded that ice margin anomalies are capable of altering local climates in certain regions of the high and mid-latitudes. Possible interactions between high latitudes and subtropical regions also were suggested.

E. Coupled sea ice simulations

In order to test the sensitivity of an ice model to the GCM input, a four-month simulation of the thermodynamic portion of the Parkinson-Washington sea ice model was conducted using atmospheric boundary conditions that were obtained from a pre-computed seasonal simulation of the GLAS GCM. The sea ice thickness and distribution were predicted for the 1 January - 30 April period based on the GCM-generated fields of solar and infrared radiation, specific humidity and air temperature at the surface, and snow accumulation. The sensible heat and evaporative fluxes at the surface were mutually consistent with the ground temperatures generated by the ice model and the air temperatures generated by the atmospheric model.

In general, in the Northern Hemisphere the predicted ice distributions and the wintertime accretion and southward advance of the pack ice were well simulated. The computed ice thickness in the Southern Hemisphere appeared reasonable, but the Antarctic melt season was extended, causing ice coverage to be less than observed in late March and April. During the Northern Hemisphere winter, the simulated ice accretion was the result of the net deficit of longwave radiation, heat gained from the ocean, and sensible heat loss to the atmosphere. In the early part of the Southern Hemisphere summer, the melting essentially balanced the excess of solar over longwave radiation at the surface, while later in the simulation accretion balanced the longwave and convective heat losses.

The results showed that the Parkinson-Washington sea ice model produced acceptable ice concentrations and thicknesses when used in conjunction with the GLAS GCM for the January to April transition period. These results suggest the feasibility of fully coupled ice-atmosphere simulations with these two models. However, the ability of these two models to produce a realistic annual cycle of sea ice distribution is yet uncertain. (See Parkinson and Herman, 1980, for additional details.)

F. Analysis of winter and summer simulations with the GLAS GCM

This work was done collaboratively with Halem, Mintz, Shukla and others at GLAS (see Halem et al., 1975). The monthly mean fields for an ensemble of integrations were compared with the observed geographical distribution and zonal averages. The results were presented at a WMO-JOC Study Conference.

G. Cloud and radiation budgets for the second order GLAS GCM

A review was undertaken for the Workshop on Radiation and Cloud-Radiation Interaction in Numerical Modeling, held at the European Center for Medium Range Weather Forecasting in October, 1980. Here the cloud and radiation budget climatologies of several GLAS second order models were assessed for the January-February and July periods, and the model's radiation and cloud parameterizations were briefly reviewed. Systematic errors in the computed infrared radiation budget were attributed to difficulties in testing the infrared optical properties of the clouds, and in predicting sub-grid scale fractional cloudiness. The solar radiation balance was generally reasonable, although some discrepancies with observations were obtained during the Southern Hemisphere summer. Problems with the model's cloud climatology included excessive low cloudiness during the Northern Hemisphere winter, and a failure to simulate adequately the advance and retreat of the ITCZ.

Four cloud feedback experiments that were conducted with GLAS GCMs were reviewed. These included transparent cloud experiments, fixed vs. variable cloud experiments, and desert albedo feedback experiments. The role of radiation in the Siberian high was also investigated.

H. Development of a high latitude research program

As a complement to the numerical and theoretical work described above, an effort was undertaken to develop the scientific plan for research in the East Greenland Sea and Marginal Ice Zone during the 1980's. (This program is reviewed in detail in World Climate Program Rept. #77 - Report of the Meeting of Experts on Sea Ice and Climate Modelling, Appendix J.)

Publications and Reports Published under NSG-5152

A. Journal and Book Articles

1. Herman, G.F. and W.T. Johnson, 1978: The sensitivity of the general circulation to Arctic sea ice boundaries. Mon. Wea. Rev., 106, 1649-1664.

2. Baker, D.J., G.E. Weller (and others), with G.F. Herman, 1980: Polar atmosphere ice-ocean processes: A review of problems in climatic research. Rev. Geophys. Space Phys., 18, 525-543.

3. Herman, G.F., M.C. Wu, and W.T. Johnson, 1980: The effect of clouds on the Earth's solar and infrared radiation budgets. J. Atmos. Sci., 37, 1251-1261.

4. Herman, G.F. and W.T. Johnson, 1980: Arctic and Antarctic climatology of a GLAS general circulation model. Mon. Wea. Rev., 108, 1974-1991.

5. Parkinson, C.L. and G.F. Herman, 1980: Sea ice simulations based on fields generated by the GLAS GCM. Mon. Wea. Rev., 108, 2080-2091.

6. Herman, G.F. and W.T. Johnson, 1980: "The effect of extreme sea ice variations on the climatology of the Goddard General Circulation Model. In: Sea Ice Processes and Models. U. Washington Press.

7. Herman, G.F., 1984: Atmospheric modelling and air-sea-ice interaction. In: The Geophysics of Sea Ice. Plenum.

B. Special Reports

1. Halem, M., J. Shukla, Y. Mintz, M.L. Wu, R. Godbole, G.F. Herman, and Y. Sud, 1979: "Comparisons of observed seasonal climate feature with a winter and summer numerical simulation produced with the GLAS general circulation model." Rept. JOC Study Conf. on Climate Models, Performance, Intercomparison, and Sensitivity Studies, GARP Publ. Ser., 22, 538-562. (Also appears on World Meteorological Organization Technical Note.)

2. Herman, G.F. and W.T. Johnson, 1979: "The response of the Goddard GCM to sea ice boundary conditions." Rept. Study Conf. on Climate Models, Performance, Intercomparison, and Sensitivity Studies, GARP Publ. Ser., 22, 538-562. (Also appears as World Meteorological Organization Technical Note.)

3. Herman, G.F., 1981: "Cloud-radiation experiments conducted with GLAS general circulation models." Workshop on Radiation and Cloud-Radiative Interactions in Numerical Modelling. European Center for Medium Range Weather Forecasts.

4. Herman, G.F., 1983: The interaction of sea ice and climate as inferred from global general circulation models. Int. Council Sci. Unions./WMO Rept. of the Meeting of Experts on Sea Ice and Climatic Modelling. Geneva. pp. C-1-19.

Appendix

Selected significant publications and reports.

Reprinted from MONTHLY WEATHER REVIEW, Vol. 106, No. 12, December 1978
American Meteorological Society
Printed in U. S. A.

The Sensitivity of the General Circulation to Arctic Sea Ice Boundaries: A Numerical Experiment

GERALD F. HERMAN

Department of Meteorology, University of Wisconsin, Madison 53706
NASA Goddard Space Flight Center, Greenbelt, MD 20771

WINTHROP T. JOHNSON

Sigma Data Services, NASA Goddard Space Flight Center, Greenbelt, MD 20771

(Manuscript received 28 July 1978, in final form 13 September 1978)

ABSTRACT

A series of experiments were conducted with the Goddard general circulation model to determine the effect of variation in the location of Arctic sea ice boundaries on the model's mean monthly climatology. A control was defined as the mean of six January–February simulations with ice boundaries corresponding to climatologically minimum ice cover occurring simultaneously in the Davis Strait, East Greenland Sea, Barents Sea, Sea of Okhotsk and Bering Sea. An anomaly was similarly defined as the mean of two simulations with maximum ice conditions occurring simultaneously in the same regions. The extremes were estimated from 17 years of observed conditions in the Atlantic sector, and from five years of data in the Pacific sector.

When sea ice boundaries were at their maximum extent the following differences resulted in the January–February climatology as compared with minimum boundaries: Sea level pressure was higher by as much as 8 mb over the Barents Sea, by more than 4 mb in Davis Strait, and by slightly less than 4 mb in the Sea of Okhotsk. Pressure was lower by as much as 8 mb in the north Atlantic between Iceland and the British Isles, and in the Gulf of Alaska. Pressure rises of as much as 4 mb in the eastern subtropical regions of the North Atlantic and North Pacific accompanied pressure falls in the Gulf of Alaska and Icelandic region. Pressure also increased over the Mediterranean region. Geopotential heights at 700 mb were more than 80 gpm lower in the Gulf of Alaska, and more than 100 gpm lower in the Icelandic region. Changes of opposite sign occurred over the subtropics. Zonally averaged temperatures were cooler by 2°C below 800 mb between 50 and 70°N with little change elsewhere. The poleward flux of total energy was a maximum of 13% greater between latitudes 40 and 53°N.

The computed 700 mb geopotential differences were more than twice the inherent variability or "noise" of the model over a broad region of the North Pacific, and between Iceland and the British Isles. Pressure differences were more than twice the inherent variability in the Davis Strait, Gulf of Alaska and Barents Sea, and in the eastern subtropical Atlantic and Pacific. Statistical significance of zonally averaged differences was largest between 50 and 70°N where the confidence levels were as follows: for geopotential height differences, 99% (850 mb), 99% (700 mb) and 97% (500 mb); for temperature, 97% (850 mb) and 92% (700 mb); and sea level pressure, 94%. Confidence levels were high for changes in the Azores region.

On the basis of model results we conclude that ice margin anomalies are capable of altering local climates in certain regions of the high and mid-latitudes. Possible interactions between high latitudes and subtropical regions also are suggested.

1. Introduction

Are interannual variations of the wintertime ice cover in the seas of the North Atlantic and North Pacific responsible for any significant changes in large-scale circulation features? Large excursions about the mean limit of the Arctic pack ice boundary are commonly observed in the Barents and Greenland Seas, the Davis Strait, the Sea of Okhotsk and the Bering Sea. Table 1 shows the mean values, extreme limits and standard deviations of the ice extent for the winter months of January–March for the period 1961–77 in the North American and Eurasian sectors. The difference between the extremes can be greater than the approximate area of the average total ice cover, as in the Davis Strait and Labrador Sea.

The predominant effect of ice-cover variation is to alter the exchange of heat and moisture between the atmosphere and the surface of the ocean. This is due to the strong insulating property of a sufficiently thick layer of sea ice. As an example of the large difference in sensible heating between ice-covered and open ocean, Vowinckel and Taylor (1965) computed a surface sensible heat flux of about 220 W m^{-2} over open water for January in the west Eurasian Arctic, as compared with a value of about

0027-0644/78/1649-1664$08.00

TABLE 1. Sea ice cover* in the Atlantic sector, 1961–77 (10^6 km^2).

	Average cover	Standard deviation	Maximum	Minimum
Davis Straits and Labrador Sea	0.76	0.23	1.28 (Feb 1972)	0.15 (Jan 1974)
East Greenland Sea	1.09	0.18	1.52 (Feb 1967)	0.83 (Jan 1972)
Norwegian-Barents Sea	1.42	0.16	1.82 (Mar 1966)	0.99 (Jan 1965)

* Obtained from the *Monthly Ice Charts* of the British Climatological Service, Bracknell.

-3 W m^{-2} over ice in the same region. There is an additional effect on the radiation balance due to the larger albedo of ice as compared with ocean, but it is of secondary importance during the winter because the insolation at high latitudes is so small.

There have been many attempts to determine the relationship between local synoptic features and year-to-year variations in the sea ice margin. Because variations in sea ice are themselves forced by atmospheric and oceanic parameters, it has been difficult to prove unambiguously whether an atmospheric feature that correlated with an ice anomaly was the cause rather than an effect of the anomaly. For example, the early work of Brennecke (1904) and Meinardus (1906) showed that colder than average temperatures at Icelandic stations were associated with more southerly boundaries of the pack ice in the East Greenland Sea. Were the colder temperatures the result of the southerly extension of the ice, or were both the ice limits and cold air advection a consequence of the large-scale atmospheric pressure distribution?

There were many subsequent efforts to show that sea ice was the cause of climatic variation. On the basis of ice extent and meteorological data collected at the end of the nineteenth century, Hildebrandsson (1914) hypothesized that average wintertime conditions in Europe and, in fact, throughout the Northern Hemisphere, depended on the summer ice content of the East Greenland Sea. Wiese (1924) found correlations between the ice margin in the East Greenland and Norwegian Seas and subsequent storm frequency and precipitation over northern Europe and Scandinavia. Severe ice in the April–July period was associated with a more southerly track of North Atlantic cyclones during the fall. Wiese also found a good correlation between the mean air temperature in the May-June period in northern Europe and concurrent ice conditions in the Barents Sea. Scherhag (1936) argued that the anomalously warm temperatures at North Atlantic stations during 1932–35 winters were connected with the recession of the ice margin in the East Greenland Sea. Defant (1961, p. 283) suggested a positive feedback between ice extent and atmospheric pressure: southerly ice drift associated with positive pressure anomalies over the polar oceans causes an expansion of the ice margin and a further increase in surface pressure. Ice margin was thus viewed as a mechanism for perpetuating high pressure anomalies in the central Arctic.

There have also been attempts to relate Arctic sea ice to global-scale weather features. Walker (1947) found weak correlations between ice content of the Newfoundland region of the western North Atlantic, and Icelandic and north European pressures, but found no convincing relationships for ice in the East Greenland or Barents Seas. On the other hand, the recent analyses of Schell (1956, 1970), which used more extensive sea ice and meteorological data, have shown some correlation between ice margin and temperatures and pressures over Europe both for concurrent and for time-lagged fields. Schell (1964) conducted a similar study using ice data from a single station in northern Japan but found no significant correlation with subsequent North Pacific pressures.

Recent attempts to predict ice drift in the Alaskan Arctic with empirical orthogonal functions have suggested that there is a correlation between the dominant temperature and sea ice eigenvectors at a time lag of minus one month (cf. Walsh, 1979, Fig. 7). We infer from this that sea ice may cause atmospheric anomalies in the Alaskan Arctic because heavy ice in the Bering and Beaufort Seas leads to colder temperatures in the Alaskan sector one month later.

There has also been speculation concerning the consequences of catastrophic variations of Arctic sea ice, *viz*, the complete removal of the pack ice (cf. Fletcher, 1968) or the extreme ice surges of an ice age (cf. Williams *et al.*, 1974). Fletcher suggested on the basis of heat budget arguments that a hypothetical ice-free Arctic would cause weaker meridional temperature gradients and a weaker zonal circulation, and would be accompanied by more high-latitude snowfall due to increased evaporation over the Arctic Ocean. The Williams *et al.* January simulations with the NCAR general circulation model (GCM) found that ice age boundary conditions caused no significant difference in mean zonal wind strength as compared with the present, but there was a significant southward displacement of the Aleutian and Icelandic lows and the track of maximum midlatitude cyclone activity. However, it is not possible to isolate sea ice effects in this experiment because sea surface temperature, snowline and other boundary conditions were changed along with ice margin.

The early GCM experiments of Fletcher *et al.* (1971) and of Warshaw and Rapp (1973) confirmed the importance of sea ice in high-latitude climate but showed little hemispheric or global influence. Statistical validity of sea ice experiments was established in the Warshaw and Rapp experiments, and

the model results suggested that the stronger convective heating occurring in a hypothetical ice-free central Arctic would give rise to warmer temperatures in the lower troposphere north of about 55°N. The Fletcher *et al.* experiments showed that the complete removal of Arctic sea ice would cause the wintertime anticyclone in the central Arctic to be replaced by a deep low.

Herman and Johnson (1979) conducted a set of experiments to test the sensitivity of the Goddard GCM to extreme variations of sea ice margin in the North Atlantic and North Pacific Oceans. Margin variations nearly twice as large as those observed in recent times were imposed to ensure that there would be a significant difference between calculations carried out for minimum ice conditions, and maximal extent that perhaps represented ice age conditions. The important effect that ice margin had on the mass field (i.e., height of geopotential surfaces) was seen in the Aleutian and the Icelandic regions: 500 mb geopotential heights were as much as 120 gpm lower in the north Pacific corresponding to extreme ice margin changes in the Sea of Okhotsk and Bering Sea.

Here we report the results of a set of numerical experiments conducted with the Goddard (formerly GISS) general circulation model. The experiments were designed to test the model atmospheric response to a single fixed and specified parameter, the total ice cover in the Davis Strait, Barents Sea, East Greenland Sea, Sea of Okhotsk and Bering Sea. Ours differ from any earlier GCM ice experiments by considering margin variations that are substantially smaller than those involved in ice age or ice-free Arctic simulations. Variations imposed here represent approximately the observed conditions during the past 17 years in the three peripheral Arctic seas of the Atlantic sector, and during the years 1973–77 in the Pacific sector. The experiment *control* was the mean of six model calculations with identical ice boundary conditions corresponding to a climatological minimum, but differing from one another by small, random values in the initial temperature, pressure and wind fields. We are required to define our control in this fashion to ensure statistical significance of results (see Appendix B). Similarly, the *anomaly* was the mean of two runs corresponding to climatological maximum sea ice conditions.

The differences that we obtain between the respective means of the control and the anomaly represent to a high level of statistical significance the effect of ice boundary conditions on the *model calculations*. However, there is an important constraint in our model which limits the conclusions we may draw about the effect of sea ice on the true *atmospheric* circulation. Ocean temperatures and sea ice extent are fixed parameters in the model experiments, while their actual evolution is coupled closely to atmospheric processes. Large heat loss from ice-free margin regions could not continue indefinitely. Ocean temperatures would fall and heat

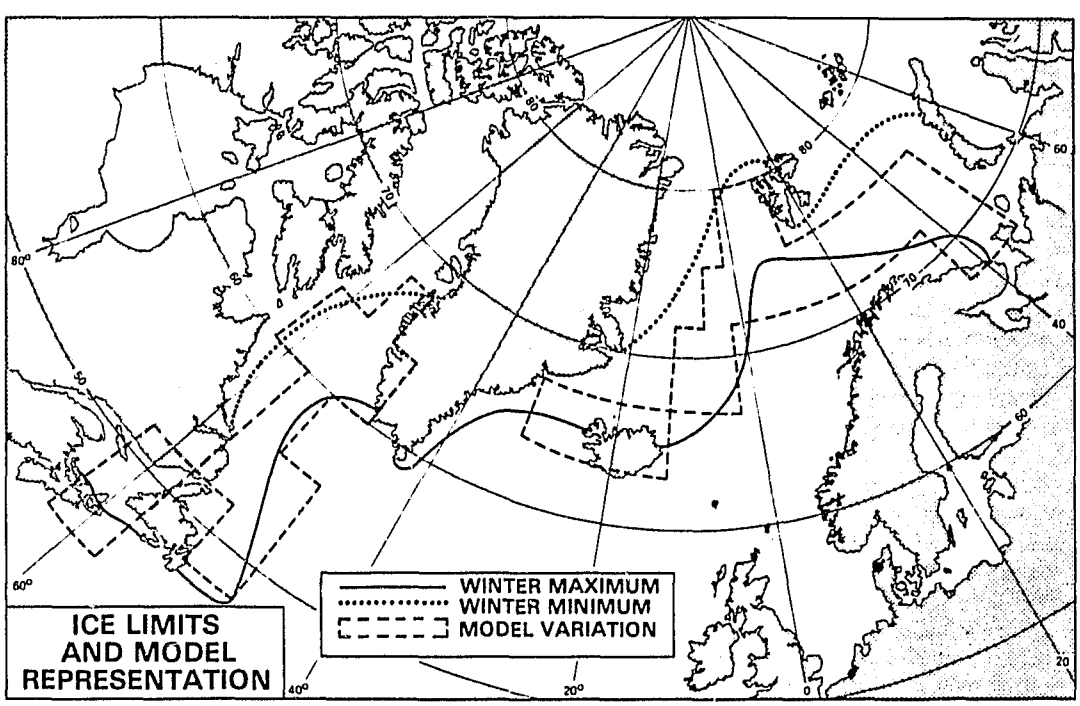

FIG. 1. Composite January–February–March sea ice maxima and minima for the North Atlantic, 1961–77. Dashed line is the Goddard GCM grid representation of the envelope of wintertime ice margin extremes.

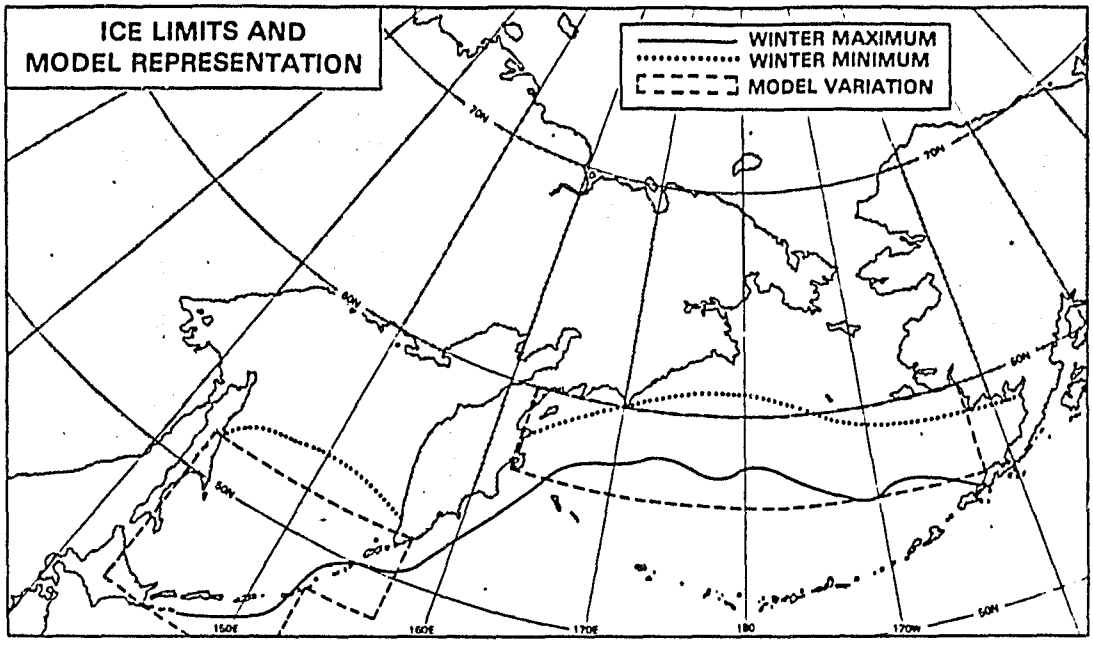

FIG. 2. As in Fig. 1 except for the North Pacific, 1973–77.

flux would diminish. A new layer of ice might even be sustained. For the simulation of monthly climate, however, fixing ice margin is less serious than fixing the sea surface temperature since actual month-to-month margin changes normally are smaller than the changes that occur from one year to the next.

2. Design of experiment

a. Ice specification

We have estimated the minimum and maximum extent of sea ice in the Davis Strait and Barents and East Greenland Seas based on the monthly ice charts available from the British Climatological Service, which date to 1961. Shown in Fig. 1 are the approximate maximum and minimum limits for 6/10 to 10/10 pack ice for the years 1961–77 for the composite January–February–March period.

The ice boundaries shown in Fig. 1 represent an *envelope* of extreme ice conditions over the 17-year period. Ice margin does not in general vary synchronously in all Arctic seas, and it is commonly observed (Sanderson, 1975) that maximum conditions in one region of the Arctic accompany minimum conditions in another.

Ice margin limits in the Bering Sea and Sea of Okhotsk determined on the basis of charts from the U.S. Navy Fleet Weather Facility are shown in Fig. 2. Availability of data in the North Pacific constrained us to a smaller number of seasons than in the North Atlantic. The true envelope of extreme conditions in the Pacific would probably be larger if we considered 17 years as we did in the Atlantic. Maximum ice conditions in most seas usually occur during March or April, although April limits were not considered in this experiment.

The rectangular regions in Figs. 1 and 2 represent the model grid areas in which the lower boundary was changed from ocean to ice corresponding to the difference between maximum and minimum conditions. The areal extent and number of grid points are, respectively: Barents Sea, 0.7×10^6 km^2 (9½ points); East Greenland Sea, 1.0×10^6 km^2 (13½ points); Davis Strait, 1.4×10^6 km^2 (10 points); Bering Sea, 0.9×10^6 km^2 (7 points); Sea of Okhotsk, 0.8×10^6 km^2 (5 points). One point in the Great Lakes and two in the Gulf of Bothnia were also changed.

Sea ice in the Goddard model is fixed as a 3 m slab with specified thermal and conductive properties. Sea ice influences the surface energy balance through its temperature, which is calculated from a surface energy balance equation involving net radiative, sensible and latent heat fluxes, heat conduction from the ocean and rate of melting. Its albedo is fixed at 0.70, and evaporation is computed assuming unit ground wetness. Variable ice concentration is not considered, and ice occupies the entire 4° latitude by 5° longitude grid element. All sea ice properties are constant throughout the central Arctic and peripheral Arctic seas.

b. Other data specifications

Model initial conditions were obtained from the 0000 GMT global National Meteorological Center

(NMC) analysis for 1 January 1975. This date was chosen so that recent model statistics could be combined with the earlier initial state perturbation experiments of Spar *et al.* (1978). The distribution of sea surface temperature and Antarctic ice conditions for the control followed closely the Rand Corporation analysis used in the extreme ice experiment of Herman and Johnson (1979).

c. Model calculations

The version of the Goddard model used here is essentially that described by Somerville *et al.* (1974) and Stone *et al.* (1977). Minor modifications that were made subsequent to these papers are briefly summarized in Appendix A.

A single realization of a January–February climate was simulated by integrating the model from 1 January initial conditions until 14 February. Model output at 12 h intervals (0000 and 1200 GMT) was averaged for the period 14 January–12 February. The first 14 calculated days did not enter the average because their fields have larger variances associated with the model's adjustment to initial conditions.

The ensemble mean control (i.e., minimum ice conditions) was estimated as the arithmetic average of six January–February realizations. The first consisted of 1 January 1975 initial conditions, and three others were obtained from the Spar *et al.* (1978) initial state experiments (see Appendix B). Two more runs were added to the ensemble using 1 January 1975 initial conditions but containing several trivial coding differences. The ensemble mean anomaly (i.e., maximum ice conditions) was estimated as the mean of two January–February realizations. One consisted of 1 January 1975 initial conditions but with maximum ice imposed. The second also had maximum ice, but initial temperature, wind and surface pressure that differed by small random amounts as described in Appendix B.

All *difference fields* referred to hereafter will represent the difference between the estimated ensemble mean control field, and the ensemble mean anomaly field, i.e., the average of six runs for minimum ice conditions minus the average of two runs for maximum ice conditions.

3. Results of calculation

a. Hemispheric fields

1) SEA LEVEL PRESSURE

The distribution of the difference (minimum minus maximum) of mean January–February sea level pressure is shown in Fig. 3. When ice is at its maximum extent in the North Atlantic, sea level pressure rises in the Barents Sea and in Davis Strait, and falls in the North Atlantic between Iceland and Great Britain. Maximum ice in the North Pacific causes a less pronounced pressure increase in the Sea of Okhotsk, and a 4 mb pressure fall in the Gulf of Alaska. The pattern of sea level pressure difference is straightforward to explain. When sea ice covers the Sea of Okhotsk, Barents Sea or Davis Straits, there is much less sensible and latent heating of the atmosphere than there would be if these seas were ice free. Less boundary layer heating results in less low-level convergence and generation of cyclonic vorticity, and leads to a comparatively higher pressure. Although there are no variations of sea ice in the Gulf of Alaska or between Iceland and Great Britain, sea level pressures over these seas were generally lower when ice margin was maximal. Lower pressure northwest of Britain accompanies high pressure in the Barents Sea and Davis Strait as a result of mass conservation. The more difficult question to explain is why the compensating pressure change occurs preferentially in the North Atlantic and not in some other region such as the central Arctic. It is interesting that several of Schell's (1970, Figs. 11–14) composite pressure differences show a similar pattern of lower pressure over Iceland and northern Scandinavia accompanied by high pressure over the North Atlantic-British Isles for light as compared with heavy ice seasons. Such a comparison is limited, however, because Schell had correlated winter synoptic conditions with ice conditions of the preceding April–September period. There is no time lag in the present study.

Sea level pressure differences in the North Pacific are not as systematically related to ice margin dif-

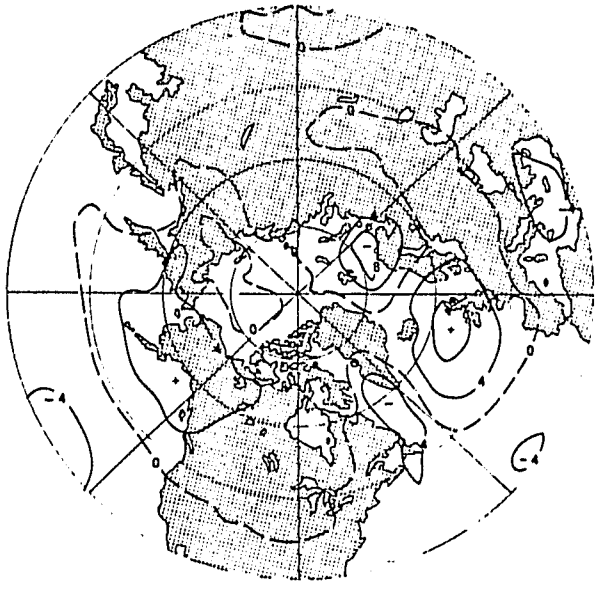

FIG. 3. Sea level pressure difference (mb) corresponding to pressure with minimum (control) ice conditions minus pressure with maximum (anomaly) ice conditions.

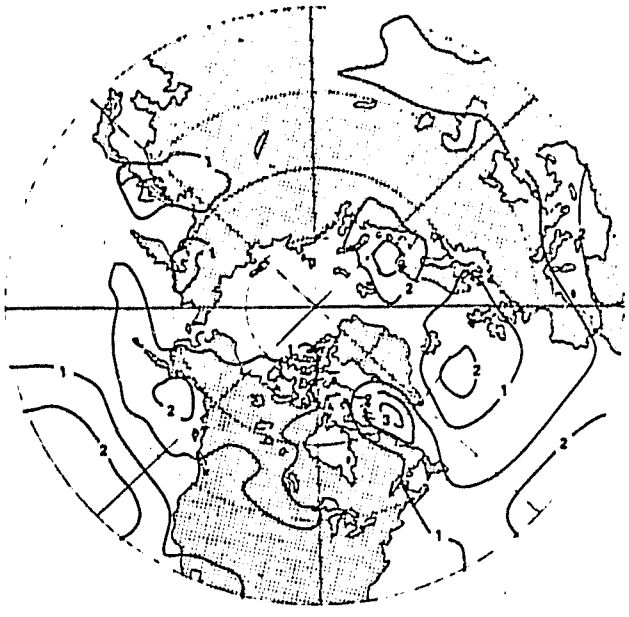

FIG. 4. Ratio of absolute value of sea level pressure difference to standard deviation of sea level pressure.

ferences as they are in the Atlantic. While a pressure rise occurs over the Sea of Okhotsk, pressure has fallen over the Bering Sea and Gulf of Alaska. The Bering Sea differences, however, are not statistically significant. Inherent variability (cf. Appendix B) of the Goddard model is larger in the Bering and Norwegian Seas than anywhere else in the Northern Hemisphere. Pressure differences in the Bering Sea simply are indistinguishable from noise.

As a measure of statistical significance we consider the signal-to-noise ratio which is obtained by normalizing pressure differences by the standard deviation of sea level pressure (Fig. 4). The increase in pressure caused by more ice exceeds two standard deviations of model noise over the Sea of Okhotsk and northern Japan, the Barents Sea and northern Scandinavia, and in the Davis Straits. The compensating pressure falls exceed two standard deviations locally in the Gulf of Alaska, and in the north Atlantic between Iceland and Great Britain. Regions with differences of two standard deviations or more occur also in the eastern mid-Pacific, eastern mid-Atlantic and over North Africa. Differences which occur in the subtropics suggest possible teleconnections between the high latitudes, midlatitudes and subtropical latitudes and are discussed further in Section 3c.

2) 700 mb TEMPERATURE AND GEOPOTENTIAL

The model's 700 mb hemispheric temperature field is altered by the imposed ice margin changes (Fig. 5a). Because there is stronger convective and latent heating associated with minimum ice cover, 700 mb temperatures are colder with maximum ice in the Sea of Okhotsk, over the northwestern Soviet Union, and over the north Atlantic between the southern tip of Greenland and the British Isles. These temperature changes with maximum ice cause the 700 mb geopotential height (Fig. 5b) to decrease by more than 80 gpm in the North Pacific, and by more than 100 gpm in the North Atlantic. There is some uncertainty in relating the location

FIG. 5a. 700 mb temperature difference corresponding to minimum minus maximum ice conditions.

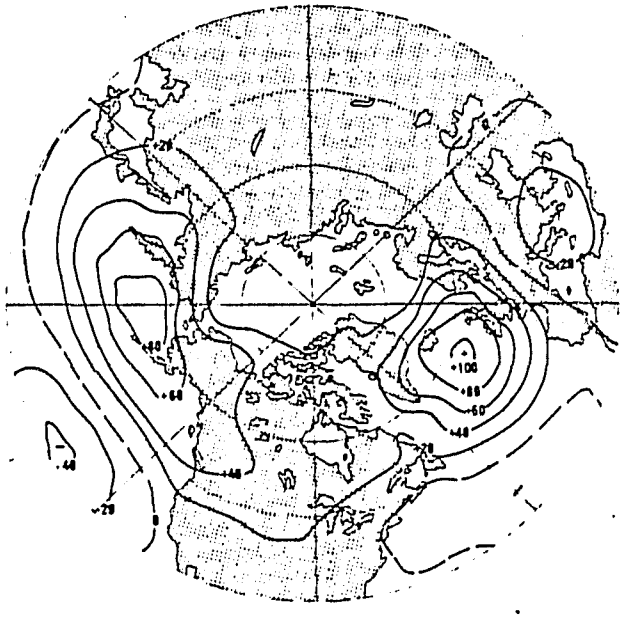

FIG. 5b. 700 mb geopotential height difference (gpm) corresponding to minimum minus maximum ice conditions.

of upper level changes to the location of surface changes because we imposed ice margin changes in several regions simultaneously. The change in the North Atlantic could be a downstream response to changes in the East Greenland Sea. Similarly, the temperature change centered over Novaya Zemlya could be a downstream response to the East Greenland Sea change, or a local response to the Barents Sea change. Here local responses would correspond to virtually no phase lag between the location of the heat source and location of maximum temperature change, while the downstream interpretation would require phase lags of about 30–40° from the heat sources in the Davis Straits and Barents Sea. Positive differences occur also over western Canada and the southwestern United States.

The absolute value of the geopotential difference between minimum and maximum ice conditions is normalized by the standard deviation of the 700 mb geopotential height and is shown in Fig. 6. Differences larger than three standard deviations are obtained to the east of Hokkaido and the Kamchatka peninsula. The differences between Greenland and the British Isles are greater than two standard deviations. Differences over the rest of the Northern Hemisphere are difficult to distinguish from noise.

Ice margin apparently is capable of affecting the pattern of "blocking" in the model's 700 mb flow field. If the surface heat sources (i.e., ice-free areas) are located sufficiently close to the major stationary troughs in the North Atlantic and North Pacific, then the changes in amplitude of both

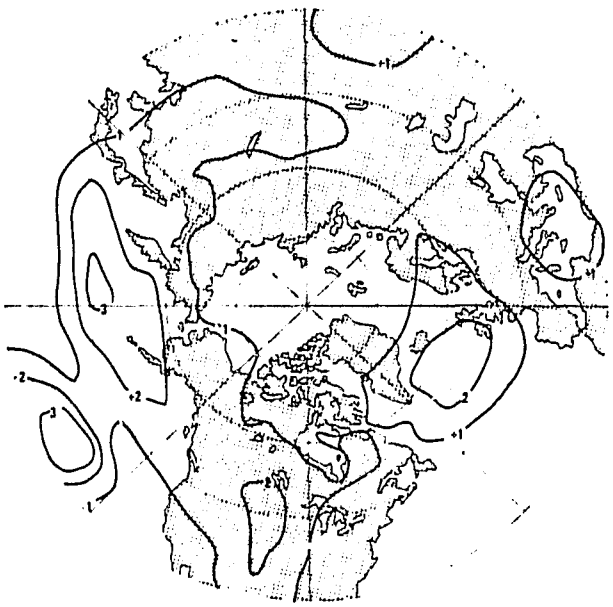

FIG. 6. Ratio of the absolute value of the 700 mb height difference to the standard deviation of the 700 mb height field.

FIG. 7a. 300 mb geopotential height difference (gpm) corresponding to minimum minus maximum ice conditions.

ridges and troughs at 700 mb may become very large due to resonant forcing. Similar effects have been attributed to North Atlantic sea surface temperature anomalies (Namias, 1964) and dynamical mechanisms have been proposed by Smagorinsky (1953) and others.

3) 300 mb GEOPOTENTIAL

Geopotential height differences caused by ice margin variation occur at high levels, and do not appear to have any systematic phase shift with height. Figs. 7a and 7b show that large differences and signal-to-noise ratios occur at 300 mb to the east and south of the Sea of Okhotsk, over the central United States, and northwest of Great Britain. The features are similar to those in the 700 mb geopotential difference field, but in the Atlantic and Pacific there is a slight shift southward and eastward of the region of ice margin change. Evidently the largest phase shifts are confined to the lowest 300 mb of the troposphere.

b. Zonally averaged temperature

Differences in the pattern of surface heating due to margin variations have an effect on the zonally averaged temperature, but significant changes are confined to the lowest layers of the high-latitude troposphere. Zonal temperatures (Fig. 8) are 2°C greater with less ice in the belt 42–70°N and from the surface to 800 mb. The corresponding signal-to-noise ratio (not shown) exceeds 2 between 50–70°N up to 600 mb, and exceeds 3 up to 835 mb.

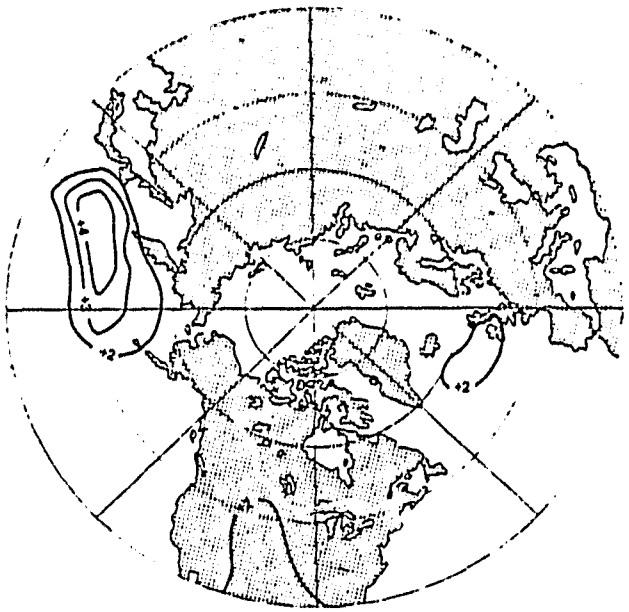

FIG. 7b. Ratio of the absolute value of the 300 mb height difference to the standard deviation of the 300 mb height field.

c. *Hemispheric changes and teleconnections*

In addition to local changes that occurred at latitudes where the ice margin perturbations were imposed, there were regions of high statistical significance in subtropical latitudes, and even in the Southern Hemisphere. Signal-to-noise ratios larger than 2 occur in the sea level pressure field (Fig. 9) in the eastern subtropical Atlantic and eastern subtropical Pacific Oceans and in the Mediterranean region. Small regions of significance in sea level pressure appear near the Weddell Sea and near the Tasman Sea, but these can be dismissed as being statistically spurious, even if they do represent more than a single point. Some grid points will be significant purely on the basis of chance, and these points will necessarily involve a number of adjacent grid points because the sea level pressure field is spatially coherent, i.e., pressures at adjacent model grid points are related through hydrostatic and hydrodynamic laws. Moreover, it is hard to imagine a viable mechanism that could relate Southern Hemisphere changes to Arctic ice perturbations. [The possibility of relationships between north and south polar ice has been mentioned by Defant (1961).]

There are good reasons for believing that the subtropical changes are real and caused by Arctic ice variations. Regions of significant differences in the subtropics occur systematically between most of the control and anomaly runs, and they cover areas that are as extensive as the differences at high midlatitudes. More importantly, the possibility of a significant relationship between pressure variations in high and low latitudes of the North Atlantic is becoming well established on the basis of observations. Kutzbach (1970) showed that the pattern for the first eigenvector of the January sea level pressure consisted of large variations of opposite sign occurring in the Icelandic region and the mid-Atlantic. Additional evidence that variations in the Icelandic region are accompanied by variations of

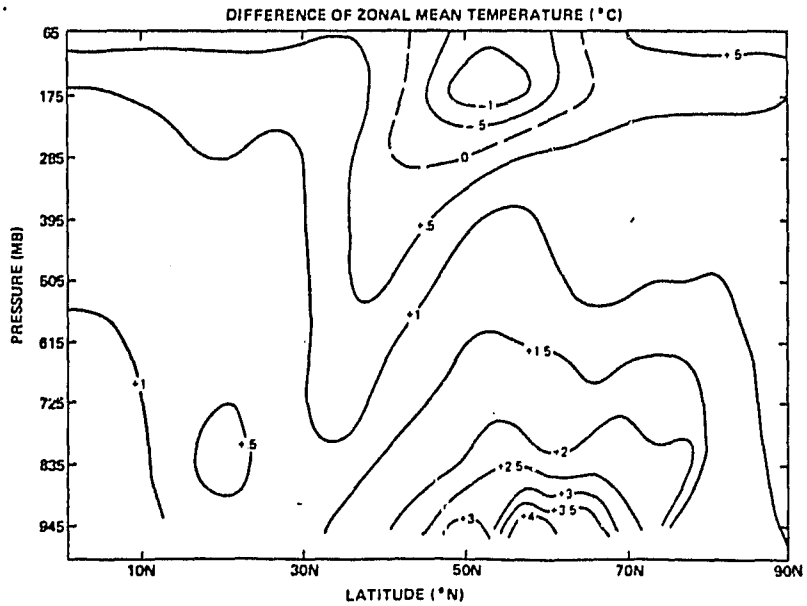

FIG. 8. Difference between zonal mean temperature corresponding to minimum minus maximum ice conditions. Positive values signify that temperatures are colder with maximum ice.

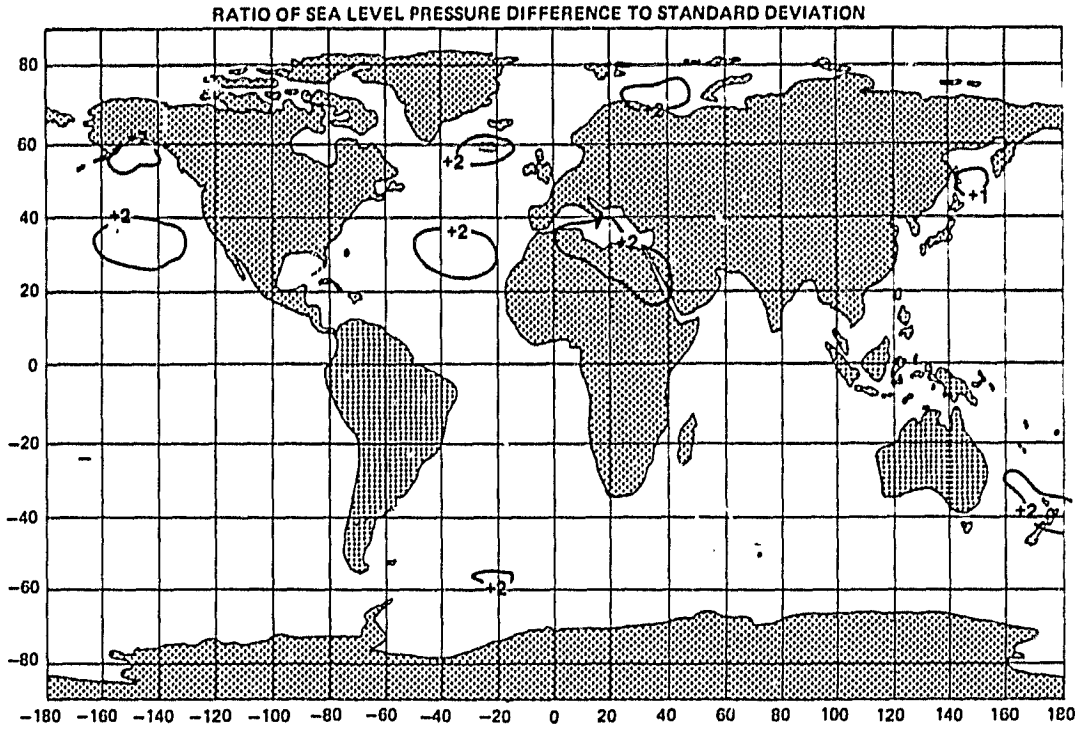

FIG. 9. Absolute value of signal-to-noise ratio for global sea level pressure difference. Values greater than 2 in subtropics correspond to higher pressure with maximum ice, while in the Gulf of Alaska and near Iceland they correspond to lower pressure.

opposite sign near the Azores has been presented in the sea surface temperature (SST) studies of Bjerknes (1962), and has also been mentioned by Lamb (1971). Namias (1972) found that intensification of the Azores High accompanies low-pressure anomalies in the Newfoundland Sea region.

If the results of this experiment are representative of the true atmospheric response to sea ice variations, then they support the hypotheses of Namias (1958) and others that there exist *teleconnections* or physical relationships between anomalies at high latitudes or in the Arctic, and anomalies at lower latitudes. It is not surprising that the pattern of teleconnections for ice anomalies resembles so closely that for SST anomalies (e.g., Namias, 1964; Ratcliffe and Murray, 1970) because both anomalies represent an alteration of the thermal forcing of planetary-scale waves.

We cannot at this time state quantitatively a dynamical mechanism for these concurrent changes. The explanation obviously involves conservation of mass and vorticity. Ice anomalies in the Atlantic occur near 65°N, i.e., close to the rising branch of the wintertime Ferrel cell, which automatically couples the surface convergence near 60°N to that near 30°N, i.e., near the descending branch of the cell. Alternatively, the amplification of the North Atlantic trough through generation of positive vorticity accompanies an intensifying ridge and negative vorticity.

d. Integral quantities

It has been suggested in discussions of long-term climatic effects of sea ice (cf., World Meteorological Organization, 1978, p. 10) that variations in ice extent would change the poleward transfer of heat by the eddies and by the mean meridional circulation. In order to examine possible changes in the poleward flux, we have computed the vertical integral of the zonally averaged total energy flux due to eddies, F_e, where

$$F_e = (2\pi a/g)\cos\theta \times \int [C_p(vT)_e + L(vq)_e + (v\Phi)_e]dp, \quad (1)$$

and that due to the mean meridional circulation, F_m, where

$$F_m = (2\pi a/g)\cos\theta \times \int [C_p(vT)_m + L(vq)_m + (v\Phi)_m]dp. \quad (2)$$

Here $(vT)_e$ and $(vT)_m$ are the northward temperature fluxes by the eddies and the mean circulation, respectively. Similarly, $(vq)_e$ and $(vq)_m$ are the water

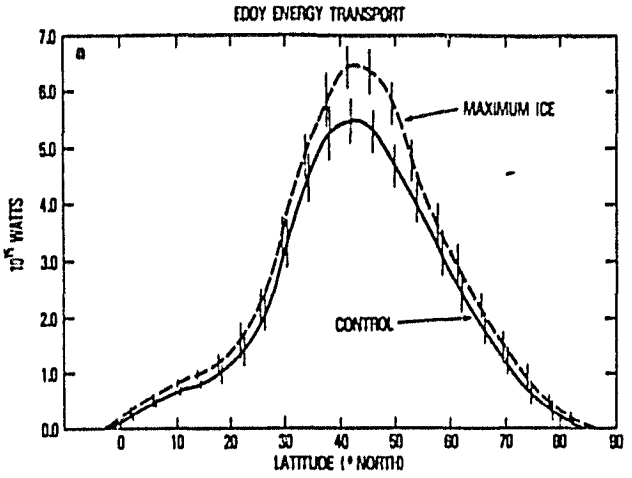

FIG. 10a. Vertically integrated poleward energy flux by eddies.

vapor fluxes and $(v\Phi)_e$ and $(v\Phi)_m$ are geopotential fluxes. Also, C_p is specific heat, L latent heat of vaporization, g gravity, p pressure, θ latitude and a the earth's radius.

Figs. 10a and 10b show the ensemble mean values of F_e and F_m, respectively, for maximum and minimum ice conditions. The error bars on the curves denote the standard deviations of F_e and F_m for the six runs that comprise the control.

Between latitudes 40 and 53°N the eddy energy flux with maximum ice is larger by almost 1×10^{15} W, which is more than twice the standard deviation of the energy flux in the control runs. Elsewhere the energy transport is larger, but the differences cannot be considered statistically significant. The magnitude of the energy flux by the mean meridional circulation is significantly larger between 40 and 53°N with maximum ice but differences are trivial elsewhere.

These results suggest that the feedback between

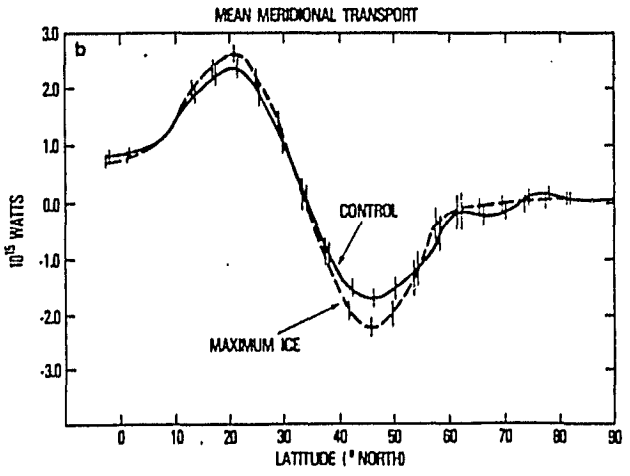

FIG. 10b. Vertically integrated poleward energy flux by mean meridional circulation.

sea ice and the poleward eddy energy flux is negative. As the ice margin expands, the temperature gradient at the surface and at low levels is increased and baroclinicity is enhanced. Larger transports result from a combination of a stronger gradient near 50°N and increased eddy activity. Although the real ice margin depends on ocean surface temperature and salinity, which our model does not compute, we speculate that there could be a limit to ice margin growth that is determined by the atmospheric energy transports. That would occur if there were a convergence of heat into the latitude bands where the ice margin was expanding that was large enough to inhibit further growth or even cause recession of the pack ice.

We did not compute the terms in the Lorenz energy cycle for these experiments. In the earlier ice extent experiment (Herman and Johnson, 1978) we found only slight differences in the conversion and storage terms for margin differences that nearly corresponded to ice age conditions.

4. Significance of results

The results presented here are clear evidence that variations of the fixed sea ice boundaries in the Goddard GCM cause statistically significant differences in the model's mean monthly climate both in high midlatitudes and in subtropical high-pressure zones. The model's response is consistent with our physical notion of how the atmosphere should respond to changes in surface heating at high latitudes, and these results strongly support numerous hypotheses that there are observed atmospheric anomalies that not only correlate with ice margin variations but are caused by them. In contrast to studying real atmospheric data, there is little ambiguity in determining that changes in the model's circulation were caused precisely by the ice margin changes provided that the circulation changes are sufficiently greater than the inherent model variability. This advantage results from being at liberty to specify fixed ice margins and ocean surface temperatures during the model calculation, but is at the price of neglecting the potential feedbacks between the ice cover and the high latitude heat budget and circulation. The sensible and latent heating over the model's ice-free Arctic seas would not proceed at the same rate in the atmosphere because the real ocean surface layer would lose heat to the atmosphere during air mass modification, and possibly even initiate accretion of new ice. The magnitude of the changes calculated here probably would be smaller if the model included an interactive ocean surface layer and pack ice because the heat fluxes would diminish as the ocean cooled.

If it is assumed that these results represent the true atmospheric response to ice margin anomalies, then several significant implications follow.

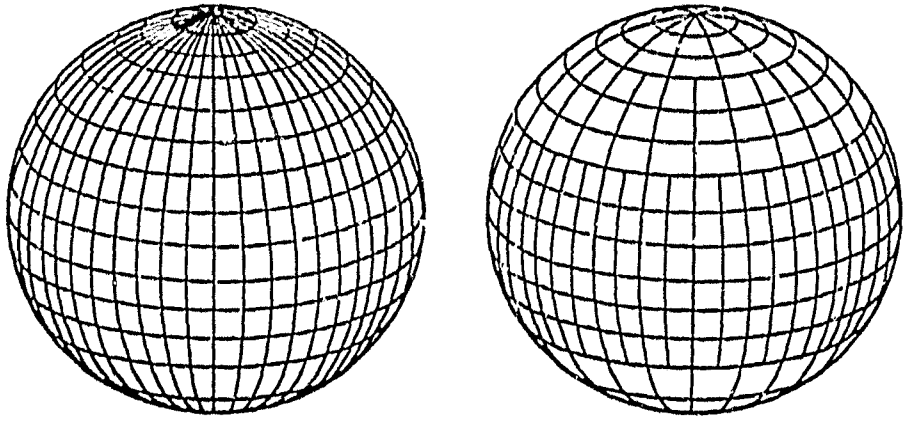

FIG. A1. Split grid as used in GLAS model.

1. *Ice margin is capable of exerting local synoptic influence*. The Davis Strait, the Barents Sea and the Sea of Okhotsk, and parts of the East Greenland Sea will have higher pressure when they are ice covered and this represents either less frequent or less intense cyclone activity, and concomitant cloudiness and precipitation. At the same time the expansion of the high pressure into the Barents Sea between Norway and Spitsbergen should cause a southward deflection of North Atlantic cyclones as proposed by Wiese (1924) and Schell (1970), but the statistical significance of such a conclusion is not high. We have computed the average precipitation for the control over Scandinavia of 1.6 ± 0.7 mm day^{-1}, and over northern Europe of 0.8 ± 0.3 mm day^{-1}. For the anomaly we obtain 2.5 ± 0.7 mm day^{-1} over Scandinavia and 1.4 ± 0.5 mm day^{-1} over northern Europe. Such an increase in precipitation would be consistent with more north Atlantic cyclones being deflected to northern Europe when there is maximum ice.

If real large-scale ice margin anomalies are sufficiently long-lived, i.e., they persist for a time period comparable to or greater than the length of our averaging period (~4 weeks), then there is predictive value in observing the location of the ice margin. [According to J. E. Walsh and C. M. Johnson (personal communication, 1978) ice margin anomalies tend to persist for several months.] A relatively large anomaly ("signal") would be required because of the large atmospheric variability in high and mid-latitudes. Sea level pressure changes correlate with concurrent ice margin changes, but from the present study we can make no statement about the possibility of time-lagged correlations.

2. *Ice margin is capable of exerting synoptic influence on a hemispheric scale*. Because anomalies of the Azores high have been found to be so well correlated with Icelandic low anomalies, ice margin changes in the Davis Strait or East Greenland Sea are linked to pressure changes in the subtropical regions of the eastern North Atlantic Ocean through their effect on the Icelandic low. The pressure change mechanism in the model involves only atmospheric processes because model sea surface temperatures are specified and do not respond to changing atmospheric conditions. Anomalies of seasonal climate in polar, mid-latitude and tropical regions are interdependent, and the construction of empirical or numerical prediction models as well as the design of observing systems necessarily involve hemispheric considerations.

APPENDIX A

Model Considerations

Several features of the Goddard GCM have been changed subsequent to the model summary given by Somerville *et al.* (1974). Those changes which were implemented in our calculations were in the high-latitude differencing scheme and in the parameterization of the planetary boundary layer and ground hydrology.

Differencing schemes containing grid elements equally spaced in latitude and longitude are less desirable because the Courant-Friedricks-Levy (CFL) stability criterion places a severe limitation on the size of the time step because of the spatial convergence of meridians in polar regions. Additional filtering of the highest frequency modes is required at those latitudes where the CFL condition is violated.

In an internal publication Halem and Russell[1] describe the so-called split-grid differencing scheme that is applied at high latitudes. The split grid retains a grid spacing of 4° latitude by 5° longitude up to 62°N. From 66 to 78°N the longitudinal spacing is 10°, and from 82° to the Pole it is 20° (Fig. A1). The modification also is made in the

[1] Goddard Space Flight Center, Institute for Space Studies, 1973 Research Review, pp. 194–200.

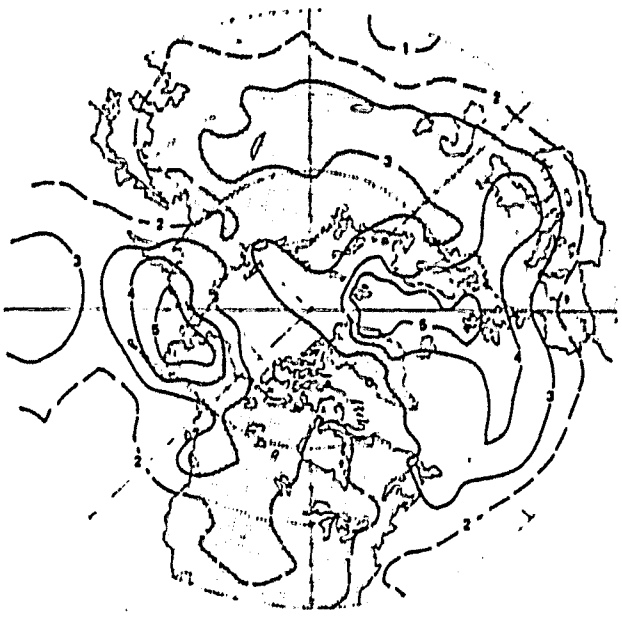

FIG. B1. Standard deviation (mb) of six mean monthly sea level pressure fields used for control.

Southern Hemisphere. The finite-difference equations were constructed for the new mesh spacing to ensure the same quadratic conservation properties of the original Arakawa differencing scheme for equal spacing on spherical grids. Additional differencing modifications to the momentum conservation equation were required to guarantee the conservation properties involving the integrated pressure gradient terms and the Coriolis term. It was found that the integration step could be doubled while eliminating spurious instabilities and significantly reducing the amount of smoothing required in polar regions. Model accuracy was not significantly affected outside of polar regions.

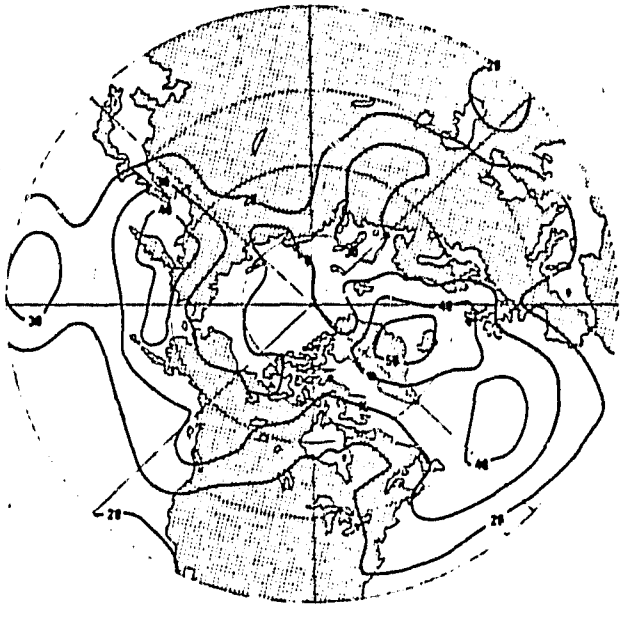

FIG. B2. Standard deviation (gpm) of six mean monthly 700 mb geopotential height fields.

The drag coefficient which governs surface exchange was multiplied by an empirical coefficient to give better agreement with observations. The surface roughness z_0 over the ocean is computed as a function of the friction velocity u_*. Following Cardone (1969),

$$z_0 = Au_*^{-1} + Bu_*^2 + C, \qquad \text{(A1)}$$

where A, B and C are empirically derived constants. The surface roughness enters into a logarithmic law for the drag coefficient which is solved interatively because it involves u_* implicitly.

Ground wetness is fixed globally in the model's hydrology, but the ground temperature calculation includes the temperature change caused by the freezing or melting of ice in the ground. For this reason an account is kept of the fraction of total water that is frozen at each grid point.

APPENDIX B

Statistical Evaluation of Results

Do the calculated difference fields represent a statistically significant difference between the mean control (minimum) ice conditions and mean anomaly (maximum) ice conditions? We estimate control and anomaly means as arithmetic averages of six and two January–February simulations, respectively. It is possible that other difference fields could have been generated if other members of a normal population of January–February simulations were chosen to compute control and anomaly means.

Laurmann and Gates (1977) and Chervin and Schneider (1976) have proposed several statistical tests for evaluating GCM model results. Ideally, conclusions reached on the basis of GCM simulations should be independent of the statistical test used. Statistical evaluation of this experiment was based on consideration of signal-to-noise ratios and a Student's t-test.

a. Signal-to-noise

Model "noise" or "inherent variability" is a measure of the extent to which the numerous dynamic instability mechanisms represented in a model amplify small differences in the initial state, or even differences associated with computer round-off. These mechanisms include baroclinic and barotropic instability, layered convective adjustment and parameterization of subgrid-scale cumulus convection. (In nature these are some of the mechanisms that cause one January climatology to differ from another.)

We expanded on the initial state perturbation experiments of Spar *et al.* (1978). The Spar *et al.* experiments specified rms errors in the initial state for 1 January 1975 over land consisting of differences in temperature, wind and sea level pressure of 1°C, 4 m s^{-1} and 3 mb, respectively. These figures were doubled over the oceans. These values represent the standard deviation of a normal distribution of differences specified randomly over land and over the ocean.

The control ensemble mean μ_c of a quantity ϕ is the arithmetic average of the mean value of that quantity obtained in each of N runs, i.e.,

$$\mu_c = \sum_{i=1}^{N} \phi_i/N. \qquad \text{(B1)}$$

The mean value ϕ_i is the arithmetic average of a model quantity f_{ij} which is sampled every 12 h. Thus, averaging over the last 30 days of a 42.5-day perturbation run,

$$\phi_i = \sum_{j=1}^{60} f_{ij}/60. \qquad \text{(B2)}$$

The anomaly ensemble mean μ_a is similarly defined with $N = 2$. As a measure of noise we use the unbiased estimate of the standard deviation s of the control mean,

$$s = [\sum_{i=1}^{N} (\mu_c - \phi_i)^2/(N-1)]^{1/2}. \qquad \text{(B3)}$$

Fig. B1 shows the standard deviation of sea level pressure computed from the six control simulations. The dominant feature of this map is that the largest standard deviations are found in middle and high latitudes, and most notably in regions where ice margin variability is observed to be the largest. This is not surprising since ice margin variations are caused largely by synoptic variations (cf., Walsh, 1978). Variability is largest (≥5 mb) in the extremely baroclinically unstable region off the east coast of Siberia, and in a portion of the North Atlantic storm track along the Greenwich meridian between Scotland and Spitsbergen. Variability of more than 3 mb occurs in the central North Pacific, central North Atlantic, and over most of Europe and central Asia. Values of 2 mb or less occur equatorward of about 38° everywhere except in the central Pacific.

The pattern of variability is qualitatively the same at 700 mb and at 300 mb as the standard deviation of geopotential height surfaces (Figs. B2 and B3) indicate. Two maxima occur over Asia, one directly over the Sea of Okhotsk, and another extending from the Barents Sea along the Ural mountains to central USSR. Maxima also occur in the central North Atlantic and North Pacific, between Greenland and northern Europe, and over northwestern North America.

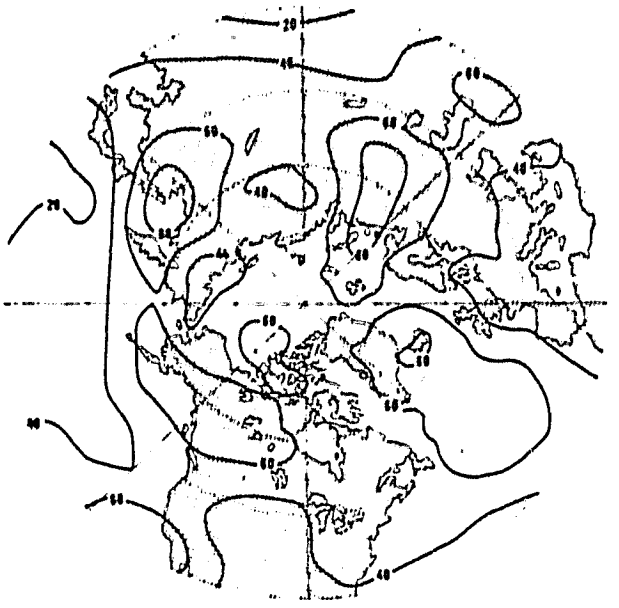

FIG. B3. As in Fig. B2 except for 300 mb geopotential height fields.

b. "t-tests"

We have also computed a Student's t-test for our results and find that our conclusions are not significantly different from those reached on the basis of signal-to-noise ratios. In particular, the Welch test as used by Chervin and Schneider [1976, Eqs. (2) and (3)] was applied to determine the confidence level at which we reject the hypothesis that there is no significant difference between control and anomaly. Fig. B4 shows the model grid points for which a 95% confidence value was computed for sea level pressure differences. (Individual grid points for which the calculated confidence level was 95% or greater are denoted by a plus sign.) Clusters of points for which the confidence level was 95% or greater for sea level pressure occur in the Gulf of Alaska, Davis Strait and Barents Sea; in the North Atlantic between Iceland and the British Isles, in the eastern regions of the subtropical North Atlantic and North Pacific Oceans; and over North Africa. Values of 95% occur at a number of other isolated points. The significance of 500 mb temperatures is somewhat different where clusters of points having greater than 95% confidence are found only over the North Pacific, the central United States and over the eastern subtropical Atlantic. There are also grid points in the Antarctic with 95% confidence values.

In fact, the t-statistic of a variable at a single grid point is not a meaningful quantity because the true sample size includes all global grid points. A better measure of confidence is the t-statistic that is computed for geographically averaged quantities.

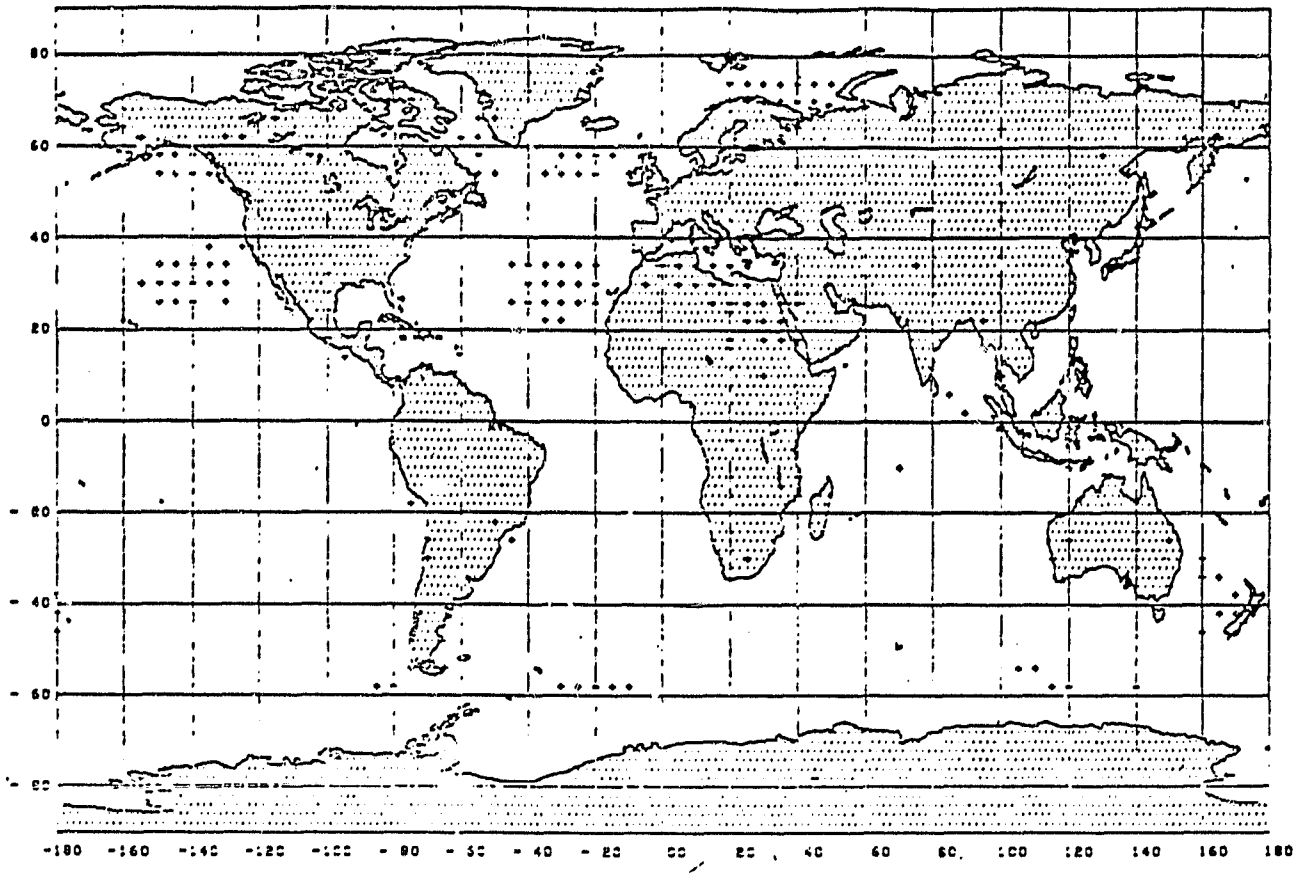

FIG. B4. Global distribution of model grid points at which sea level pressure difference between control and anomaly had a confidence value of 95% or greater (denoted by plus sign).

In Table B1 are shown the confidence levels for differences between ensemble means of areally averaged quantities, e.g., the mean of six average Northern Hemisphere sea level pressures of the control minus two average Northern Hemisphere pressures for the anomaly. Calculations are shown for global and hemispheric averages, averages about 20° latitude bands, and several local regions of interest.

The largest confidence values are found in the 70–50°N latitude band where values of 99% occur in 850 and 700 mb geopotential height, and 94% in sea level pressure. (The largest zonally averaged geopotential and temperature signal-to-noise ratios occurred between 70 and 50°N.) Large confidence values do not systematically occur in any other latitude bands. Note that the confidence value for both globally averaged 850 mb temperature and geopotential difference is 92%. Northern Hemisphere temperature differences have largest confidence values (94%) at 850 mb, and geopotentials (96%) at 700 mb. Hemispheric pressure differences are not significant.

On a regionally averaged basis sea level pressure differences yield high levels of confidence (95%) when averaged over western Canada and Alaska, and over the subtropical north Atlantic ocean. Values for temperature and geopotential differences are generally high when averaged over the North Pacific, but not when averaged over the north Atlantic. (A greater fraction of grid points had large signal-to-noise ratios in the area arbitrarily defined as North Pacific than in the one defined as North Atlantic.) Note that confidence levels are generally low for variables averaged over the central Arctic, northern Europe and Scandinavia.

In general we view these results with some pessimism as they illustrate the difficulty of observing the high-latitude response in GCM sensitivity studies. Relatively small differences in surface and upper level fields yield relatively high confidence levels in tropical and subtropical regions, but relatively large anomalies (ice cover or surface temperature) are required to produce a significant impact on meteorological fields at high latitudes. Clearly, it will be more difficult to predict seasonal fluctuations in high latitudes and midlatitudes based on response to anomalies in lower boundary conditions.

Acknowledgments. We are indebted to Dr. Milton Halem and the staff of the Modelling and Simulation

TABLE B1. Confidence level (percent) for differences between geographically averaged quantities.

	T_{850}	T_{700}	T_{500}	SLP	Z_{850}	Z_{700}	Z_{500}
1. Global average	92	88	82	80	92	92	90
2. Northern Hemisphere average	94	91	81	49	94	96	93
3. Southern Hemisphere average	88	85	82	82	86	86	86
4. Zonal averages							
90–70°N	94	90	73	7	27	61	76
70–50°N	97	92	74	94	99	99	97
50–30°N	91	86	75	71	17	79	83
30–10°N	89	92	87	89	79	89	90
10–10°S	84	83	84	59	66	90	87
10–30°S	87	84	78	71	10	92	87
30–50°S	80	71	61	69	59	37	18
50–70°S	86	85	83	84	85	85	85
70–90°S	96	88	87	71	77	80	83
5. Regional averages							
Western Canada & Alaska	54	75	60	95	93	90	86
Western United States	85	91	93	38	85	94	95
North America	96	94	85	68	91	94	93
Siberia	95	94	86	6	61	86	90
Central Arctic	90	92	83	11	21	54	74
Northern Europe	38	3	24	43	70	74	53
Scandinavia	46	15	23	34	77	79	59
North Pacific	90	94	81	18	84	94	95
Subtropical North Atlantic	90	95	97	95	79	63	91
North Atlantic	91	88	70	2	44	63	69

Facility of the Goddard Laboratory for Atmospheric Science (GLAS) for providing the facilities and support for these experiments. We appreciate the valuable comments and suggestions offered during the course of this analysis by Professors Yale Mintz and J. Shukla. Gerald Herman is supported by a NASA Faculty Research Associateship at the University of Wisconsin under Grant NASA-NSG-5152.

REFERENCES

Bjerknes, J., 1962: Synoptic survey of the interaction of sea and atmosphere in the North Atlantic. *Geofys. Publ.*, 24, 116–145.

Brennecke, W., 1904: Beziehungen zwischen der Luftdruck verteilung und den Eisverhaltnissen des Ostgrönlandischen Meeres. *Ann. Hydrogr. Mar. Meteor.*, 32(II), 49–62.

Cardone, V. J., 1969: Specification of the wind field distribution in the marine boundary layer for wave forecasting. Rep. TR-69-1. Geophys. Sci. Lab., New York University [NTIS AD-702-490].

Chervin, R. M., and S. H. Schneider, 1976: On determining the statistical significance of climate experiments with general circulation models. *J. Atmos. Sci.*, 33, 405–412.

Defant, A., 1961: *Physical Oceanography*, Vol. I. MacMillan, 728 pp.

Fletcher, J. O., 1968: The influence of Arctic pack ice on climate. *Meteor. Monogr.*, No. 30, 93–99.

——, Y. Mintz, A. Arakawa, and T. Fox, 1971: Numerical simulation of the influence of Arctic Sea ice on climate. WMO Tech. Note No. 129, *Proc. IAMAP/IAPSO/WMO Symp. Energy fluxes over polar surfaces*, Moscow.

Herman, G. F., and W. T. Johnson, 1979: The effect of extreme sea ice variations on the climatology of the Goddard general circulation model. *Sea Ice Processes and Models: Proc. ICSI/AIDJEX Symp.*, University of Washington Press (in press).

Hildebrandsson, H. Hildebrand, 1914: Quelques recherches sur les centres d'action de l'atmosphère. *Kung Sven. Vetenskap. Hand.*, 51, 3–16.

Kutzbach, J., 1970: Large-scale features of monthly mean Northern Hemisphere anomaly maps of sea level pressure. *Mon. Wea. Rev.*, 98, 708–716.

Lamb, H. H., 1971: *Climate: Present, Past and Future*. Methuen, 614 pp.

Laurmann, J. A., and W. L. Gates, 1977: Statistical considerations in the evaluation of climatic experiments with atmospheric general circulation models. *J. Atmos. Sci.*, 34, 1187–1199.

Meinardus, W., 1906: Periodische Schwankungen der Eistrift bei Island. *Ann. Hydrogr. Mar. Meteor.*, 34, 148–162 227–239, 278–285.

Namias, J., 1958: The general circulation of the lower troposphere over the Arctic regions and its relation to the circulation elsewhere. *Polar Atmosphere Symposium*, R. C. Sutcliffe, Ed., Pergamon Press, 341 pp.

——, 1964: Seasonal persistence and recurrence of European blocking during 1958–1960. *Tellus*, 16, 394–407.

——, 1972: Influence of northern hemisphere general circulation on drought in nortneast Brazil. *Tellus*, 24, 336–342.

Ratcliffe, R. A. S., and R. Murray, 1970: New lag associations between North Atlantic sea temperature and European pressure applied to long range weather forecasting. *Quart. J. Roy. Meteor. Soc.*, 96, 226–246.

Sanderson, R. M., 1975: Changes in the area of Arctic sea ice 1966 to 1974. *Meteor. Mag.*, 104, 313–322.

Scherhag, R., 1936: Eine bemerkenswerte Klimaänderung über Nordeuropa. *Ann Hydrogr. Mar. Meteor.*, 64, 96–100.

Schell, I. I., 1965: Interrelations of Arctic ice with the atmosphere and the ocean in the North Atlantic–Arctic and adjacent areas. *J. Meteor.*, 13, 46–58.

——, 1964: Interrelations of the ice off northern Japan and the weather. *J. Meteor. Soc. Jap.*, 42, 174–185.

——, 1970: Arctic ice and sea temperature anomalies in the northeastern North Atlantic and their significance for seasonal foreshadowing locally and to the eastward. *Mon. Wea. Rev.*, 98, 833–850.

Smagorinsky, J., 1953: The dynamical influence of large-scale heat sources and sinks in the quasi-stationary mean motion of the atmosphere. *Quart. J. Roy. Meteor. Soc.*, 79, 342–366.

Somerville, R. C. J., P. H. Stone, M. Halem, J. E. Hansen, J. S. Hogan, L. M. Druyan, G. Russell, A. A. Lacis, W. J. Quirk and J. Tennebaum, 1974: The GISS model of the global atmosphere. *J. Atmos. Sci.*, 31, 84–117.

Spar, J., J. J. Notario and W. J. Quirk, 1978: An initial state perturbation experiment with the GISS model. *Mon. Wea. Rev.*, 106, 89–100.

Stone, P. H., S. Chow and W. J. Quirk, 1977: The July climate and a comparison of the January and July climates simulated by the GISS general circulation model. *Mon. Wea. Rev.*, 105, 170–194.

Vowinckel, E., and B. Taylor, 1965: Energy balance of the Arctic. IV. Evaporation and sensible heat flux over the Arctic Ocean. *Arch. Meteor. Geophys. Bioklim.*, B14, 36–52.

Walker, G., 1947: Arctic conditions and world weather. *Quart. J. Roy. Meteor. Soc.*, 73, 226–256.

Walsh, J. E., 1979: Empirical orthogonal functions and the statistical predictability of sea ice extent. *Proc. ICSI/AIDJEX Symp. Sea Ice Processes and Models*, University of Washington Press (in press).

Warshaw, M., and R. R. Rapp, 1973: An experiment on the sensitivity of a global circulation model. *J. Appl. Meteor.*, 12, 43–49.

Wiese, W., 1924: Polareis und Atmospharische Schwankungen. *Geograf. Ann.*, 6, 273–299.

Williams, J., R. G. Barry and W. M. Washington, 1974: Simulation of the atmosphere using the NCAR global circulation model with ice age boundary conditions. *J. Appl. Meteor.*, 13, 305–317.

World Meteorological Organization, 1978: *The Polar Subprogramme*. GARP Publ. Ser., No. 19, 47 pp.

Reprinted from JOURNAL OF THE ATMOSPHERIC SCIENCES, Vol. 37, No. 6, June 1980
American Meteorological Society
Printed in U. S. A.

The Effect of Clouds on the Earth's Solar and Infrared Radiation Budgets

GERALD F. HERMAN

Department of Meteorology, University of Wisconsin, Madison 53706, and NASA Goddard Laboratory for Atmospheric Science, Greenbelt, MD 20771

MAN-LI C. WU

NASA Goddard Laboratory for Atmospheric Science, Greenbelt, MD 20771

WINTHROP T. JOHNSON

Sigma Data Services Corp., c/o NASA Goddard Space Flight Center, Greenbelt, MD 20771

(Manuscript received 15 March 1979, in final form 8 February 1980)

ABSTRACT

The effect of global cloudiness on the solar and infrared components of the earth's radiation balance is studied in general circulation model experiments. A wintertime simulation is conducted in which the cloud radiative transfer calculations use realistic cloud optical properties and are fully interactive with model-generated cloudiness. This simulation is compared to others in which the clouds are alternatively non-interactive with respect to the solar or thermal radiation calculations. Other cloud processes (formation, latent heat release, precipitation, vertical mixing) were accurately simulated in these experiments.

We conclude that on a global basis clouds increase the global radiation balance by 40 W m^{-2} by absorbing longwave radiation, but decrease it by 56 W m^{-2} by reflecting solar radiation to space. The net cloud effect is therefore a reduction of the radiation balance by 16 W m^{-2}, and is dominated by the cloud albedo effect.

Changes in cloud frequency and distribution and in atmospheric and land temperatures are also reported for the control and for the non-interactive simulations. In general, removal of the clouds' infrared absorption cools the atmosphere and causes additional cloudiness to occur, while removal of the clouds' solar radiative properties warms the atmosphere and causes fewer clouds to form. It is suggested that layered clouds and convective clouds over water enter the climate system as positive feedback components, while convective clouds over land enter as negative components.

1. Introduction

The earth's cloud cover exerts a profound influence on the budgets of solar and thermal radiation, and thus on the net radiation which is available to the earth-atmosphere system. It is commonly agreed that clouds have two important functions with respect to the radiation balance at the top of the atmosphere. First, the solar contribution to the radiation budget at the top of a previously clear column may change when cloud is introduced depending on the difference between the cloud albedo and the surface albedo. Over most parts of the globe clouds cause the solar contribution to decrease by reflecting more radiation back to space. Second, clouds generally enhance the infrared component of the budget by absorbing radiation that originates from the warmer layers beneath them, and emitting radiation to space at a comparatively colder temperature. This effect, of course, also depends on the cloud emissivity and the cloud temperature. It is frequently said that clouds exhibit an *albedo effect* when the radiation budget is decreased by reflection of solar radiation, and a *greenhouse effect*[1] when the budget is increased by absorption of thermal radiation.

There have been a variety of studies carried out to illustrate some of the possible mechanisms through which global-scale cloudiness affects the planetary radiation balance, the general circulation and climate. For a more complete review the reader is referred to the recent articles by Cess and Ramanathan (1978) for a discussion of cloud fraction and the radiation balance, and to Schneider

[1] More correctly, the term "greenhouse" refers to a specific family of radiative equilibrium temperature profiles which obtain in an atmosphere whose constituents interact with both solar and thermal radiation when the optical depth of maximum solar absorption is much greater than that of maximum thermal emission. See Herman and Goody (1976, Appendix B) for further discussion.

0022-4928/80/061251-11$06.75

et al. (1978) for a discussion of cloudiness and surface temperature response. Hunt (1978) recently has conducted general circulation model (GCM) experiments to study general circulation statistics in a cloud-free atmosphere.

We report here on the results of a set of experiments conducted with the general circulation model of the Goddard Laboratory for Atmospheric Science (GLAS). Our experiments are designed to demonstrate the separate effect that the visible and infrared opacities of terrestrial clouds have on the solar and infrared components of the radiation budget of the earth-atmosphere system. In particular, we wish to determine the relative role of the *albedo* and *greenhouse* effects of clouds on the radiation budget when the clouds are considered in a global aggregate.

We also investigate several mechanisms through which cloud *formation* processes may be coupled to cloud *radiative* processes. For example, does the geographic distribution of clouds change in response to the altered solar or infrared heating, or is there a redistribution of clouds in the vertical that reduces the effect of the opacity changes on the radiation budget. Finally, it will be useful to note the similarities and differences between this experiment, which separately removes the clouds' visible and infrared absorption, and those experiments and studies which in effect alter simultaneously the absorption in these two spectral regions.

It is important to note that this experiment is not a climate experiment, nor is it capable of predicting the true response of the equilibrium temperatures of the surface or of the planet to changing cloud conditions. This is principally due to the fact that current versions of the GLAS GCM, including the one used in this experiment, use specified rather than predicted values of ocean surface temperatures. Thus, the changes in the radiation field caused by cloudiness affect only the temperature and stability of the atmosphere, and the ground temperature of land and sea ice. If we were to compute an equilibrium climate for the model, it would not be determined by the planetary balance of solar and infrared radiation alone, but would also involve the imposed sea surface temperature distribution.

2. Description of experiment

Many details of the GLAS general circulation model have been described by Somerville *et al.* (1974). The version used here is essentially the same as the one used in the ice margin experiments of Herman and Johnson (1978) with the following exceptions: the snow cover was held fixed during the integration to eliminate surface albedo feedback; additional smoothing of wind, temperature and moisture fields was accomplished by using a technique developed by Shapiro (1971); sea surface temperature and sea ice cover were prescribed to vary smoothly according to climatology during the calculation.

In the control run for this experiment, solar and thermal radiation calculations were fully consistent and interactive with the model's predicted cloud fields. Solar radiation was calculated according to the method of Lacis and Hansen (1974), which explicitly treats cloud absorption and multiple scattering processes. Longwave radiation was computed and summed over 10 spectral intervals using a technique developed by M. L. Wu and L. D. Kaplan. Cloud solar optical properties were fixed according to cloud type as described by Somerville *et al.* (1974, Table 3), and unit cloud emissivity was assumed in the infrared spectrum. Since the model does not treat fractional cloudiness that occurs on the subgrid scale, clouds were assumed to cover an entire 4° latitude × 5° longitude grid area.

In one experiment (inactive solar), all cloud formation processes and radiative transfer were calculated as they were in the control, except that cloud coverage was fixed at zero in the solar radiation calculation. Thus, clouds formed, liberated latent heat and participated in vertical mixing processes, but were otherwise transparent to the streams of solar radiation. The second experiment (inactive thermal) specified zero cloud coverage in the longwave radiation calculation, but explicitly treated all other cloud processes, including solar radiation.

The initial state was defined from the 0000 GMT 1 January 1975 National Meteorological Center (NMC) global analysis, and the integration period was 30 days. Our conclusions therefore refer to an average January circulation for a model atmosphere in which the ocean surface temperature, surface albedo and sea ice extent are prescribed and noninteractive. Thus, we do not have the means to determine from these experiments whether the annual average planetary mean surface temperature would increase or decrease in association with global cloud-coverage changes. The differences between our control and experimental (transparent) simulations represent only the responses of the atmospheric and land components of the model's earth-atmosphere system.

3. Results and discussion

a. Global radiation budget

The effect of model-generated clouds on the components of the radiation budget at the top of the model's atmosphere is illustrated in Table 1. Column A refers to the January control, while columns B and C refer to the cases where model-generated clouds were absent in the thermal and solar radiation calculations, respectively. For later discussion, we cite in column E the observational results of

TABLE 1. Radiation balance for radiatively-interactive and non-interactive clouds.

	(A) January control	(B) Inactive thermal	(C) Inactive solar	(D) Model variability	(E) Observations[1] (Raschke *et al.*, 1973)
1. Net infrared radiation at top of atmosphere (W m^{-2})					
N. Hemisphere	−207	−236	−215	0.7	−232
S. Hemisphere	−213	−253	−223	0.3	−239
Global	−210	−244	−219	0.2	−235 (−231)
2. Solar radiation absorbed by earth atmosphere system (W m^{-2})					
N. Hemisphere	165	159	199	0.6	174
S. Hemisphere	332	327	429	0.4	330
Global	249	243	314	0.2	252 (243)
3. Planetary albedo (%)					
N. Hemisphere	29	31	13	0.2	27
S. Hemisphere	31	33	13	0.1	29
Global	30	33	13	0.1	28 (31)
4. Radiation balance [absorbed solar plus net infrared (W m^{-2})]					
N. Hemisphere	−42	−77	−16	2.0	−58
S. Hemisphere	119	74	206	0.4	91
Global	39	−1	95	0.3	17 (12)

[1] Values in parentheses are those of Ellis *et al.* (1978) for 65°N–65°S.

Raschke *et al.* (1973), and in parentheses the values of Ellis *et al.* (1978). The variability of each radiation budget parameter in the model has been determined in initial-state perturbation experiments (cf. Herman and Johnson, 1978, Appendix B) and is shown in column D. The variability of planetary albedo, for example, is defined as the standard deviation of the albedos obtained in six model simulations whose initial conditions differed by small, randomly distributed amounts. There is very little variability of these monthly globally averaged quantities, and the differences between runs are due to the prescribed changes in cloud properties rather than to the inherent variability of the model. The question of statistical significance of the differences between the control and the experimental runs poses no limitation to the following discussion.

In row 1 the difference between columns B and A demonstrates the extent to which clouds trap terrestrial radiation: when clouds do not interact with thermal radiation, the radiation lost to space in the Northern Hemisphere, Southern Hemisphere and globally increases by 29, 40 and 34 W m^{-2}, respectively. When clouds are non-interactive with respect to the streams of solar radiation (column C), the outgoing radiation increases slightly because the surface temperatures are warmer (see Section 3b), and the difference between columns A and C indicates the extent to which the outgoing longwave radiation is coupled, through atmospheric and surface processes, to the transfer of *solar* radiation in clouds.

Comparing the results of the control simulation (column A) with the observational analysis of Raschke *et al.* (1973) in column E, we see that the outgoing longwave flux simulated by the GLAS model is smaller than the observed. There are two likely reasons for this discrepancy. One is that all model generated clouds are assumed to have unit emissivity, including those that would correspond to atmospheric cirrus or altostratus clouds. Thus model clouds tend to be more opaque than those occurring in nature. A second is that model clouds with their extremely large horizontal extent (~400 × 400 km) at each grid point trap more radiation than do the scattered and broken cloud fields that actually occur, especially at high levels. (Both of these model deficiencies are in the process of being corrected.)

Row 2 illustrates the role that clouds play in determining the solar radiation absorbed by the model's earth-atmosphere system. Comparing columns A and B shows that eliminating the interaction of thermal radiation with clouds decreases the solar radiation absorbed by 5–6 W m^{-2} because of increased cloudiness. When clouds become transparent to solar radiation, the amount of solar radiation absorbed by the earth-atmosphere system increases in the Northern and Southern Hemispheres, and globally by 34, 97 and 65 W m^{-2}, respectively. These increases represent the solar radiation that is reflected back to space by interactive model clouds.

In general, the solar components of the model's

radiation budget (column A) are in good agreement with observations (column D). This finding is encouraging in view of the several unknown and difficult-to-measure parameters in the solar radiation calculation, *viz.*, cloud optical depth, single-scatter albedo, droplet phase functions and surface reflectance properties.

The albedo of the earth-atmosphere system (row 3) is an alternate measure of the effect of cloud on the solar radiation budget. In general, clouds maintain the planetary albedo near its observed value of 30% as compared with an albedo of 13% with non-interacting clouds. Note that there is only a slight increase in the global planetary albedo from 30 to 33% when clouds do not interact with thermal radiation.

Finally, the effect of clouds on the net radiation available to the earth-atmosphere system is shown in row 4. The net radiation balance of the January control is more positive (less negative) than the observations in the Northern and Southern Hemispheres, and globally by 14, 28 and 22 W m^{-2}, respectively. Again, this discrepancy is a likely consequence of the model's treatment of thermal absorption in high clouds, or the absence of partially clouded areas. When clouds do not interact with solar radiation, substantially more energy is available to the system because of the diminished planetary albedo, and the balance becomes more *positive* (and less negative) than the control by 26, 87 and 56 W m^{-2} in the Northern and Southern Hemispheres and globally. The balance becomes more *negative* (and less positive) in these same regions when clouds are transparent to thermal radiation by 35, 45 and 40 W m^{-2}, respectively.

Under certain circumstances (see Section 3b), it is possible to compute the net effect of the clouds on the radiation balance simply by combining the radiation loss due to the albedo effect (column A minus column C), and the gain due to the greenhouse effect (column A − column B). Thus, from row 4, the *net cloud effect* on the global net radiation balance is −16 W m^{-2}, i.e., the albedo effect makes the balance more negative by 56 W m^{-2} (39 minus 95), while the greenhouse effect makes it more positive by only 40 W m^{-2} (39 minus −1). Similarly, in the Southern Hemisphere, we obtain a cloud effect of −42 W m^{-2} and in the Northern Hemisphere, +9 W m^{-2}. Hence during the month of January the albedo effect dominates the greenhouse effect in the radiation budgets of the globe and of the Southern Hemisphere. The greenhouse effect dominates the budget of the Northern Hemisphere winter because there is less solar radiation available than in the Southern Hemisphere due to geometrical factors.

b. Temperature and cloud frequency

We may deduce the net effect of clouds on the net radiation as the difference between the albedo and greenhouse effects only if the changes caused by the two processes are independent. It is possible to imagine a variety of coupling mechanisms (feedbacks) that might relate the cloud-solar and cloud-longwave processes. For example, ground temperature differences induced by solar radiation changes might change the longwave loss at the top of the atmosphere through cloud formation processes related to stability and cumulus convection.

Table 2 illustrates the effects of cloud-radiative interactions on surface and atmospheric temperatures. Values are spatial averages with appropriate areal weighting. The surface temperatures over oceans do not change because ocean temperatures are specified in the model. When clouds are not present in the solar radiation calculation surface temperatures over land (row 1) increase in the Northern and Southern Hemispheres and globally by 2, 3 and 3°C, respectively, due to the increased direct solar heating of the ground. When clouds are absent in the longwave calculation, back radia-

TABLE 2. Spatially averaged temperatures for radiative-interactive and non-interactive cloudiness (K).

	(A) January control		(B) Inactive thermal minus control		(C) Inactive solar minus control	
	Land	Oceans	Land	Oceans	Land	Oceans
1. Surface temperature						
N. Hemisphere	271	293	−5	0	2	0
S. Hemisphere	285	291	−2	0	3	0
Global	275	292	−3	0	3	0
2. Average atmospheric temperature						
N. Hemisphere	240	252	−1	−1	2	1
S. Hemisphere	249	253	−1	−1	2	2
Global	243	253	−1	−2	2	1

tion from the atmospheres decreases substantially and hence averaged surface temperatures decrease by 5, 2 and 3°C. Spatially averaged atmospheric temperatures behave in the same fashion, over both land and ocean, i.e., temperatures increase by 1–2°C without solar interactions and decrease by 1–2°C without thermal interactions.

The degree of coupling between the radiation and the cloudiness is illustrated in Table 3, which shows the differences between the cloudiness calculated in the control and in the transparent cloud simulations. As a measure of cloudiness we use *cloud frequency*, which is defined as the fraction of the total integration time during which a specified cloud type occurred at a grid point.

Supersaturation clouds in the model, which represent in an approximate way stratiform clouds in the atmosphere, form simply when the water vapor mixing ratio at a grid point exceeds the saturation value. Thus the supersaturation (or stratus) cloud frequencies increase by 1–2% when cloud-longwave interactions are absent because of the cooler atmospheric temperatures (cf. Table 2). The cloud frequencies decrease by comparable amounts due to warmer atmospheric temperatures when solar interactions are absent, except over continental regions of the Southern Hemisphere. Evidently, there is a negative correlation in the model between the occurrence of layered cloudiness and average atmospheric temperatures.

The model's convective clouds, which represent cumulus clouds in nature, generally form less frequently than supersaturation clouds. However, the relative changes in their frequency caused by eliminating radiative interactions are much larger. The frequency changes over the oceans are correlated in a negative sense with the induced atmospheric temperature change, i.e., convective cloud frequencies decrease when the atmosphere is heated by enhanced solar radiation, and increase when it is cooled through enhanced longwave emission. Changes are on the order of 2–4%.

The opposite is true of convective cloud frequencies over land, where frequencies increase by ~0.5% when there is stronger heating (except in the Southern Hemisphere), and decrease by 2% when there is enhanced cooling. Globally, the convective frequencies decrease from the January control value of 11.2% to 9.8% with solar transparency, and increase to 12.9% with thermal transparency. Since the convective cloud frequencies over the oceans are more sensitive to solar radiation changes than those over land, we note that model-generated convective cloudiness apparently is more strongly correlated with atmospheric temperature and stability than with surface temperature. On a global basis the combined frequency of all cloud types decreases from the control value of 46.9% to 44.1% without solar interactions, and increases to 49.6% without thermal interactions.

The global distribution of cloud frequency in the GLAS model is illustrated in Figs. 1–3, where squares correspond to model grid areas, and the integer denotes the range of cloud frequency in tenths (e.g., an integer 3 means that the cloud frequency ranges between 30 and 39%). The solid line encloses regions in which the frequency of supersaturation or total cloud exceeds 70%, or where the frequency of convective cloud exceeds 30%.

Referring first to the distribution of model-generated convective clouds (Fig. 1b), we see that convective clouds form most frequently in a number of broad areas: central Brazil, Africa, Indonesia,

TABLE 3. Spatially averaged cloud frequency for radiatively-interactive and non-interactive clouds (%).

	(A) January control		(B) Inactive thermal minus control		(C) Inactive solar minus control	
	Land	Oceans	Land	Oceans	Land	Oceans
1. Supersaturation clouds						
N. Hemisphere	47.9	39.9	1.3	1.9	−1.6	−3.1
S. Hemisphere	50.2	40.8	0.3	1.5	0.5	−2.1
Global	48.6	40.4	1.1	1.7	−0.8	−2.5
2. Convective clouds						
N. Hemisphere	8.9	12.0	−1.6	4.3	0.6	−2.7
S. Hemisphere	23.0	8.5	−2.7	3.1	−0.4	−2.0
Global	13.5	10.0	−1.9	3.6	0.4	−2.3
3. All clouds						
N. Hemisphere	50.8	43.8	1.4	3.7	−1.5	−4.1
S. Hemisphere	57.6	43.8	1.5	2.9	−0.8	−3.2
Global	53.1	43.8	1.4	3.2	−1.3	−3.6

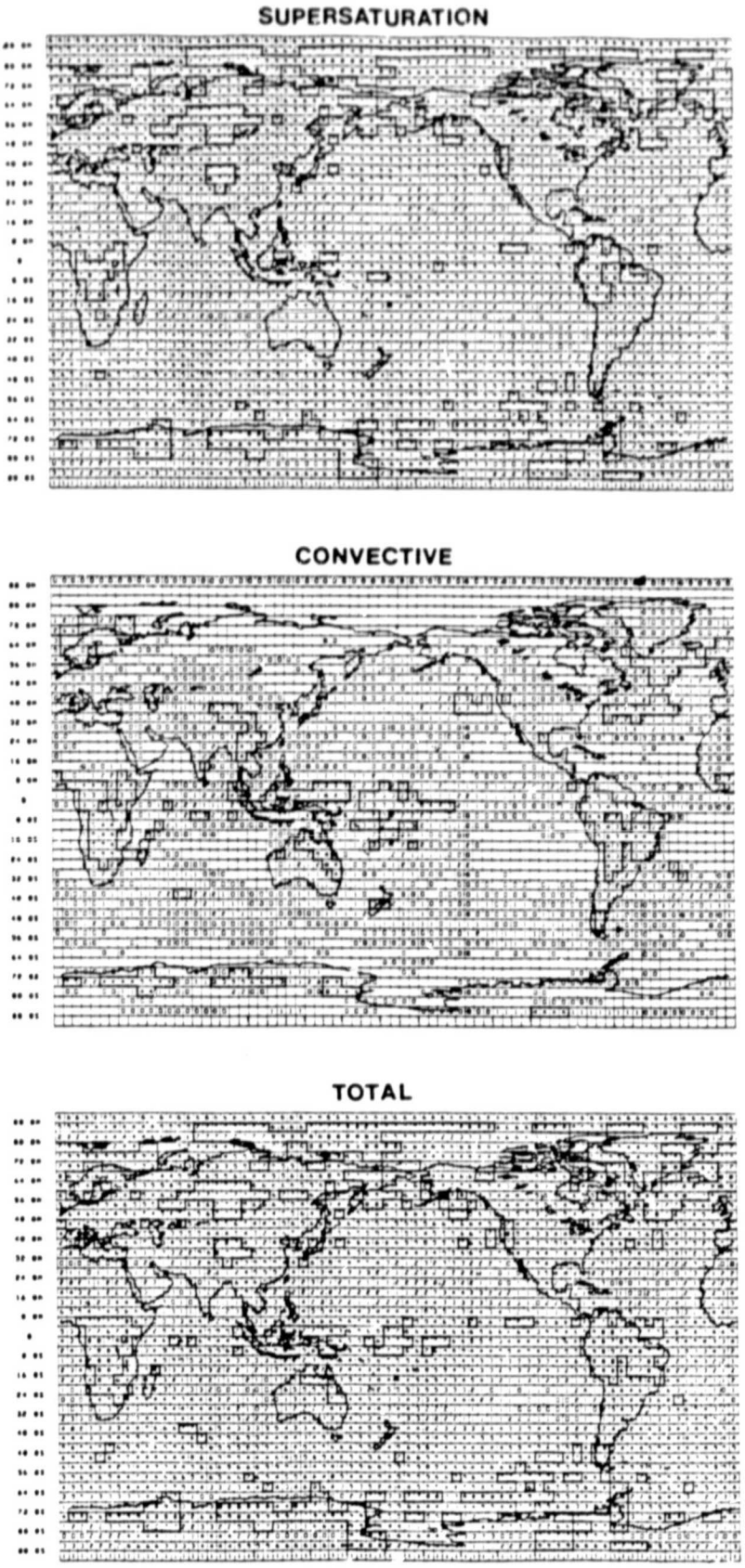

FIG. 1. Global distribution of supersaturation cloud frequencies (a), convective cloud frequencies (b) and total cloud frequencies (c) for January control. Areas enclosed by solid line illustrate regions where convective cloud frequency exceeds 30%, and where supersaturation cloud and total cloud frequency exceed 70%.

North Atlantic Ocean, tropical west Pacific Ocean, central China and east Antarctica. (The frequency of convective clouds in the latter two regions is greater than was anticipated on the basis of climatology, and possibly represents a problem in parameterizing convection in regions of extreme topography.) The eastern regions of the subtropical oceans, the desert regions of Africa, and Siberia and Canada are notably free of convective clouds.

Supersaturation clouds (Fig. 1a) occur over extensive regions of the globe, except in the eastern subtropical Atlantic, Pacific and Indian Oceans. They occur most frequently (>70%) at latitudes poleward of about 50°, and also over equatorial Africa and South America. Supersaturation clouds also form infrequently over deserts.

The combined frequency of all cloud types for the winter control is shown in Fig. 1c. The regions of most frequent cloudiness are determined almost exclusively by supersaturation clouds in mid-latitudes and high latitudes, and by a combination of convective and supersaturation clouds at low latitudes.

Figs. 2 and 3 show the global distribution of cloud frequencies for the two simulations conducted with non-interactive radiation.

Upon comparing Figs. 2b with Fig. 1b, we see that the effect of removing cloud interaction with solar radiation is to increase slightly the convective cloudiness of the Northern Hemisphere, and this occurs predominantly through the enhancement of convective-cloud formation over India and Asia Minor. It appears that in these regions model clouds that ordinarily interact with solar radiation *inhibit* convection by maintaining a less positive surface radiation balance than that which results with non-interactive cloudiness. It is difficult to point to any one region in the Southern Hemisphere that could account for the reduced hemispheric convective cloud frequency over land.

The frequency of supersaturation clouds (Fig. 2a) when there are no solar radiation interactions in the clouds tends to be slightly lower than in the control everywhere in the Northern Hemisphere, and over the oceans in the Southern Hemisphere. This decrease is generally due to the fact that warmer atmospheric temperatures are possible as the cloud's reflection of solar radiation is eliminated (cf. Table 2), and these decreases are most evident in the subtropical regions of the Atlantic and Pacific Oceans. Supersaturation cloud frequencies over land in the Southern Hemisphere increase slightly. Evidently, the increased evaporation over land in the summer hemisphere counteracts the effect of warmer atmospheric temperatures.

The most noticeable effect on the total cloud frequency of removing solar interactions is a general decrease of cloud frequency in both hemispheres. By considering only the interaction between global cloudiness with *solar* radiation, it would appear that the relation between cloud albedo and the model's cloud formation processes involves a positive feedback: as clouds become less reflective more solar radiation is available to the earth-atmosphere system, and warmer temperatures result in less total cloudiness, which in turn reflects even less solar radiation back to space.

A comparison of Figs. 1b and 3b shows that when cloud longwave radiative interactions are removed more convective clouds form over the oceans, especially in the tropical regions of the Indian and Pacific Ocean, and in the North Pacific Ocean. The model's convective clouds over the oceans, like supersaturation clouds, are correlated in a negative sense with atmospheric temperatures. Hence as the model atmosphere cools when it becomes transparent to longwave radiation (cf. Table 2), more regions in the model are susceptible to convective instabilities, and cloud frequency increases. At the same time, however, the stability of an atmospheric column depends on surface temperature. Infrared transfer in clouds tends to keep the surface radiation balance positive over land. As the clouds become transparent the ground cools more, and fewer convective clouds form. This is evident in the diminished cloud frequency over Brazil and Africa in Fig. 3b. The increase in supersaturation cloud frequency (cf. Fig. 3a) for both oceanic and land grid areas also is apparent.

The frequency of all types of clouds (Fig. 3c) increases globally when the clouds are made transparent to infrared radiation. The increase is most apparent in the high latitudes of the North Atlantic and North Pacific, in the Arctic and Antarctic, and in the equatorial tropics. The relationship between the model's cloud formation processes and infrared transfer in clouds appears to involve a negative feedback: as clouds trap less longwave radiation atmospheric temperatures cool and more clouds form, thereby permitting more radiation to be trapped.

c. *Vertical distribution of globally averaged cloudiness*

There is a redistribution in the vertical direction of the globally averaged cloud frequencies that accompany the changes in the visible or infrared capacity of the atmosphere, and this is illustrated in Table 4. The increase in globally averaged cloud frequency for the transparent infrared case (column B) is effected by an increase at virtually all levels in the model, except for supersaturation clouds at level 2 and convective clouds at level 5. The decrease in total cloudiness for the solar transparent case (column C) is caused by a decrease of frequencies at most levels, although convective and supersaturation cloud frequency each increase

North Atlantic Ocean, tropical west Pacific Ocean, central China and east Antarctica. (The frequency of convective clouds in the latter two regions is greater than was anticipated on the basis of climatology, and possibly represents a problem in parameterizing convection in regions of extreme topography.) The eastern regions of the subtropical oceans, the desert regions of Africa, and Siberia and Canada are notably free of convective clouds.

Supersaturation clouds (Fig. 1a) occur over extensive regions of the globe, except in the eastern subtropical Atlantic, Pacific and Indian Oceans. They occur most frequently (>70%) at latitudes poleward of about 50°, and also over equatorial Africa and South America. Supersaturation clouds also form infrequently over deserts.

The combined frequency of all cloud types for the winter control is shown in Fig. 1c. The regions of most frequent cloudiness are determined almost exclusively by supersaturation clouds in mid-latitudes and high latitudes, and by a combination of convective and supersaturation clouds at low latitudes.

Figs. 2 and 3 show the global distribution of cloud frequencies for the two simulations conducted with non-interactive radiation.

Upon comparing Figs. 2b with Fig. 1b, we see that the effect of removing cloud interaction with solar radiation is to increase slightly the convective cloudiness of the Northern Hemisphere, and this occurs predominantly through the enhancement of convective-cloud formation over India and Asia Minor. It appears that in these regions model clouds that ordinarily interact with solar radiation *inhibit* convection by maintaining a less positive surface radiation balance than that which results with non-interactive cloudiness. It is difficult to point to any one region in the Southern Hemisphere that could account for the reduced hemispheric convective cloud frequency over land.

The frequency of supersaturation clouds (Fig. 2a) when there are no solar radiation interactions in the clouds tends to be slightly lower than in the control everywhere in the Northern Hemisphere, and over the oceans in the Southern Hemisphere. This decrease is generally due to the fact that warmer atmospheric temperatures are possible as the cloud's reflection of solar radiation is eliminated (cf. Table 2), and these decreases are most evident in the subtropical regions of the Atlantic and Pacific Oceans. Supersaturation cloud frequencies over land in the Southern Hemisphere increase slightly. Evidently, the increased evaporation over land in the summer hemisphere counteracts the effect of warmer atmospheric temperatures.

The most noticeable effect on the total cloud frequency of removing solar interactions is a general decrease of cloud frequency in both hemispheres. By considering only the interaction between global cloudiness with *solar* radiation, it would appear that the relation between cloud albedo and the model's cloud formation processes involves a positive feedback: as clouds become less reflective more solar radiation is available to the earth-atmosphere system, and warmer temperatures result in less total cloudiness, which in turn reflects even less solar radiation back to space.

A comparison of Figs. 1b and 3b shows that when cloud longwave radiative interactions are removed more convective clouds form over the oceans, especially in the tropical regions of the Indian and Pacific Ocean, and in the North Pacific Ocean. The model's convective clouds over the oceans, like supersaturation clouds, are correlated in a negative sense with atmospheric temperatures. Hence as the model atmosphere cools when it becomes transparent to longwave radiation (cf. Table 2), more regions in the model are susceptible to convective instabilities, and cloud frequency increases. At the same time, however, the stability of an atmospheric column depends on surface temperature. Infrared transfer in clouds tends to keep the surface radiation balance positive over land. As the clouds become transparent the ground cools more, and fewer convective clouds form. This is evident in the diminished cloud frequency over Brazil and Africa in Fig. 3b. The increase in supersaturation cloud frequency (cf. Fig. 3a) for both oceanic and land grid areas also is apparent.

The frequency of all types of clouds (Fig. 3c) increases globally when the clouds are made transparent to infrared radiation. The increase is most apparent in the high latitudes of the North Atlantic and North Pacific, in the Arctic and Antarctic, and in the equatorial tropics. The relationship between the model's cloud formation processes and infrared transfer in clouds appears to involve a negative feedback: as clouds trap less longwave radiation atmospheric temperatures cool and more clouds form, thereby permitting more radiation to be trapped.

c. *Vertical distribution of globally averaged cloudiness*

There is a redistribution in the vertical direction of the globally averaged cloud frequencies that accompany the changes in the visible or infrared capacity of the atmosphere, and this is illustrated in Table 4. The increase in globally averaged cloud frequency for the transparent infrared case (column B) is effected by an increase at virtually all levels in the model, except for supersaturation clouds at level 2 and convective clouds at level 5. The decrease in total cloudiness for the solar transparent case (column C) is caused by a decrease of frequencies at most levels, although convective and supersaturation cloud frequency each increase

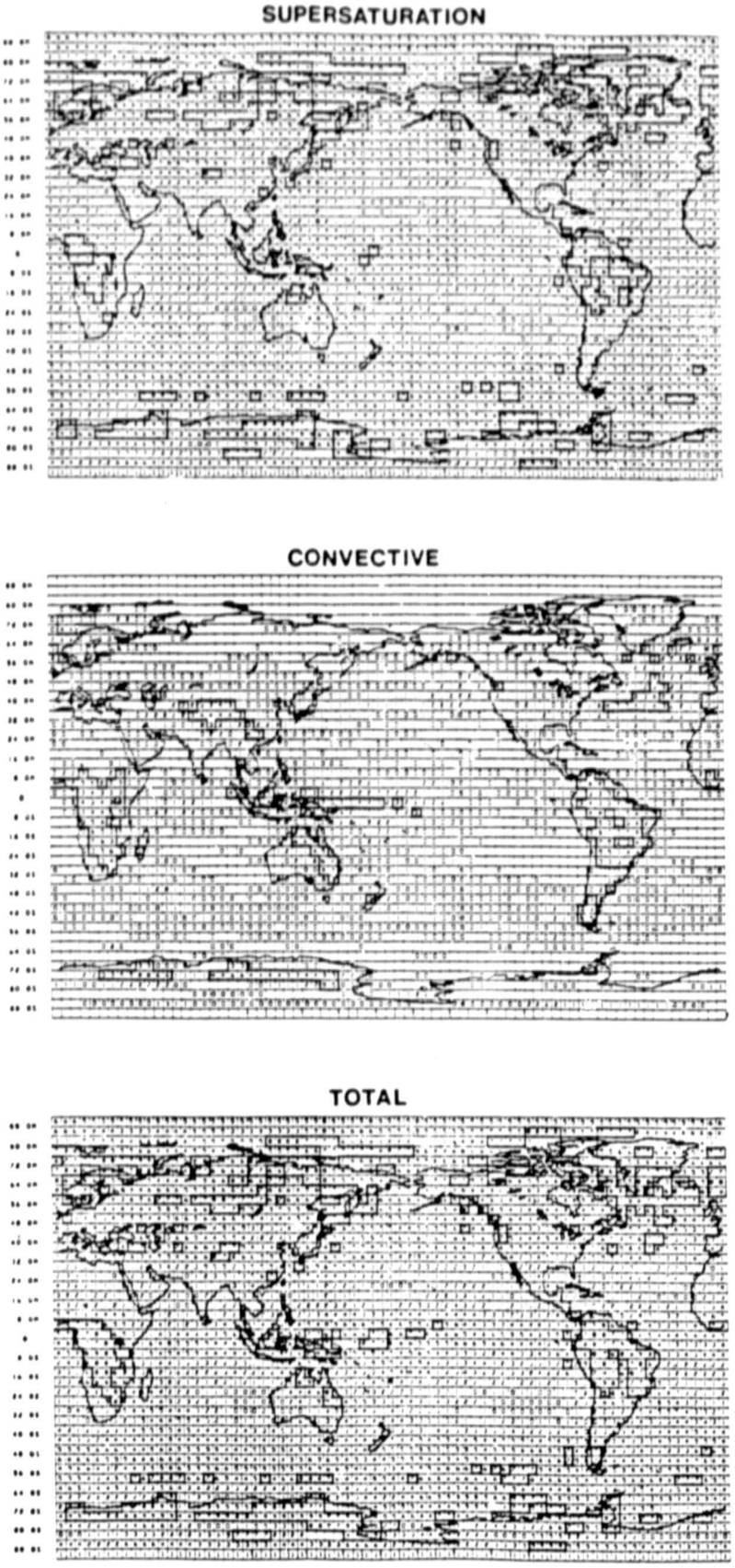

FIG. 2. As in Fig. 1 except for clouds non-interactive with solar radiation.

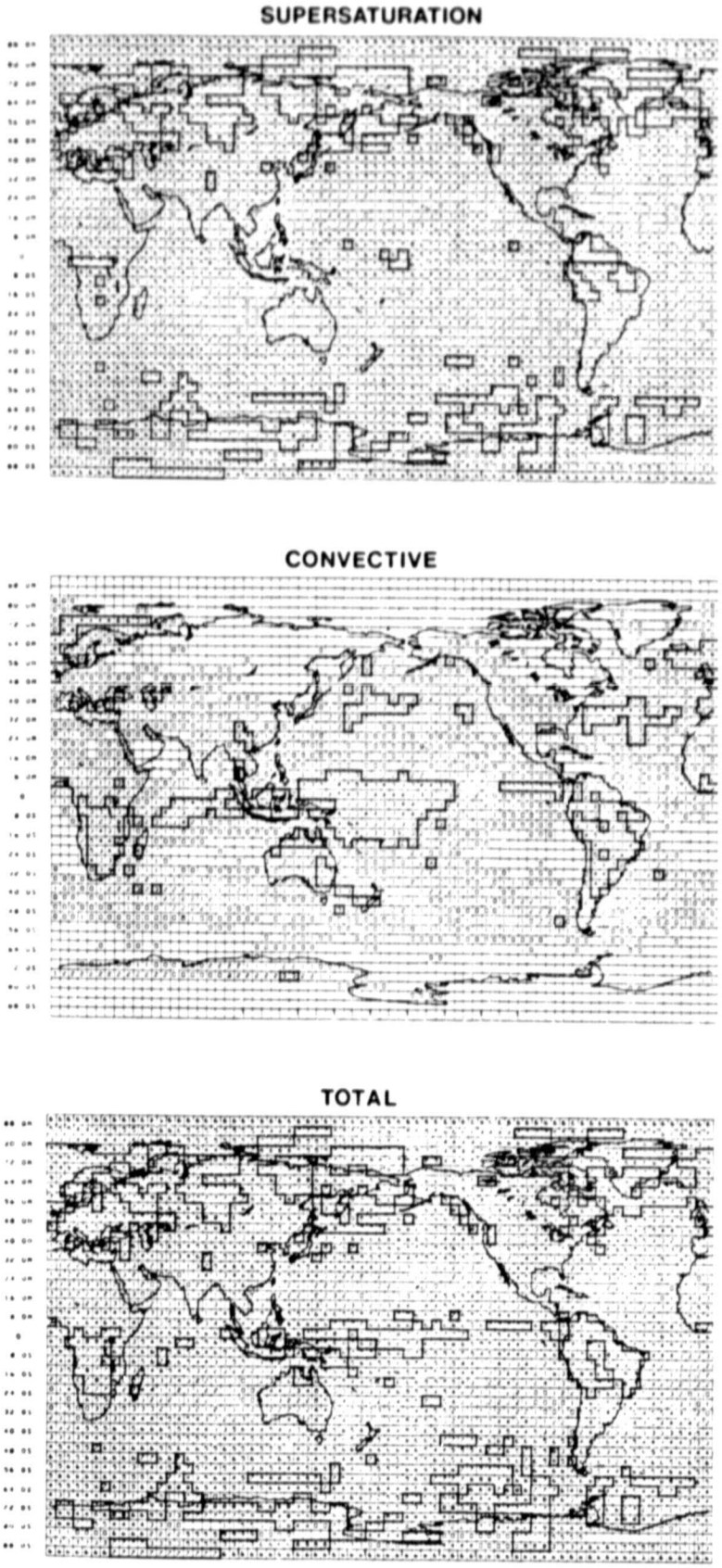

FIG. 3. As in Fig. 1 except for clouds non-interactive with thermal radiation.

TABLE 4. Globally averaged vertical distribution of cloud frequency (%) for control and non-interactive radiation.

Level	Nominal pressure at mid-level (mb)	(A) January control	(B) Inactive thermal minus control	(C) Inactive solar minus control
1. *Supersaturation clouds*				
9	945	24.1	2.3	−0.2
8	835	10.0	1.0	0.2
7	725	9.5	0.9	0.0
6	615	10.4	0.3	−0.4
5	505	11.7	0.4	−0.7
4	395	11.7	1.0	−0.6
3	285	10.1	0.4	−1.1
2	175	8.0	−1.1	−0.8
1	65	0.0	0.0	0.0
2. *Convective clouds*				
8	835	1.7	0.1	−0.1
7	725	2.9	0.1	−0.2
6	615	0.5	0.0	0.0
5	505	0.5	−0.1	0.1
3. *Penetrative convective clouds*				
9	945	1.4	0.4	−0.3
8	835	4.2	1.2	−1.0
7	725	5.5	1.7	−1.2
6	615	5.5	1.7	−1.2
5	505	4.1	1.3	−0.9
4	395	1.4	0.4	−0.3

slightly at one level. There is some tendency at most levels for the changes in the cloud frequency caused by infrared transparency to compensate partially for the changes due to solar transparency, but complete cancellation does not occur.

In particular, if we examine upper level (levels 3–5) supersaturation clouds in the model we see that the frequency is indeed greater when the clouds are capable of reflecting solar radiation as compared with the case when they are not. And upon examining columns A and C in Table 1, we see that a decrease in the amount of infrared radiation lost to space accompanies the increase in cloud frequency. Cloud redistribution within the GLAS model partly reduces the magnitude of the albedo effect, but it does not cancel it.

4. Conclusions

Recently, there has been active discussion over the relative roles of the solar and infrared effects of clouds in the global climate system. In particular, would an increase in cloud cover be associated with a surface warming due to greenhouse-type processes, or to a surface cooling due to albedo effects? Is there a simultaneous redistribution of cloud location that accompanies and possibly compensates for differences in the radiation balance caused by changed atmospheric opacity or total cloud amount?

On the basis of theoretical models of radiative equilibrium and radiative energy balances for specified cloud conditions (e.g., Manabe and Strickler, 1964; Manabe and Wetherald, 1967; Schneider, 1972; Hunt, 1977), it appears that increases in the amount of low and middle level clouds cause the surface temperature to decrease. But it also appears that increasing the upper level (e.g., cirriform) cloud amount increases the surface temperature, although this latter conclusion is more sensitive to assumptions about cloud optical properties and cloud temperature. Thus, the albedo effect appears to dominate when changes in low cloud amount occur, while the infrared effect dominates when the changes involve upper level clouds. It is important to note that the studies listed above are distinct from the present simulation in that they do not provide for changing lapse rate, moisture conditions or adjustment in cloud cover. Clearly, any discussion of the radiative effect of changing *global* cloud amounts (or atmospheric transparency) must consider the possibility of changes in the distribution and type of cloud as well, a point stressed by Cess and Ramanathan (1978). In fact, Cess (1976) suggests that changes in global cloudiness occur in such a fashion that the net radiation balance is essentially unchanged.

There are a number of results emerging from this GCM experiment that should provide some indication of the true nature of atmospheric cloud-radiative interactions.

First, the increase in the solar component of the model's global radiation budget caused by removing the visible opacity is 56 W m^{-2}, while the decrease caused by removing the infrared opacity is 40 W m^{-2}. To the extent that it is possible to treat cloud interactions with solar radiation as being independent of cloud interactions with thermal radiation, it is possible to combine the two radiative effects and conclude that the net effect of clouds on the net radiation budget is 16 W m^{-2} and is dominated by the albedo effect. Our results are therefore consistent with those of the simpler energy balance models.

It is instructive to compare our GCM results with the radiation balance study of Ellis (1978) based on satellite radiometer measurements. For the December–February period, Ellis concluded that the cloud effect on the radiation balance, ΔN, which was obtained by subtracting cloud-free values from values obtained with actual cloudiness, was 27 W m^{-2}, and was also dominated by the albedo effect. This compares favorably with the GCM value, although it should be noted that Ellis' measurements are not strictly analogous to our GCM

experiment because his observations account for the totality of atmospheric changes that accompany the cloudy-to-clear transition, while this GCM experiment separately eliminated solar and infrared interactions. As with the GCM results, Ellis' values do not apply to *small* changes in cloud amount.

Second, it does not appear that the model provides for a simultaneous adjustment of cloud distribution in the vertical that would negate the effect on the net radiation due to opacity changes. There is, in fact, an increase in model cloudiness at most levels that results from the cooler temperatures that accompany infrared transparency, consistent with the prediction of Cess (1978). However, even with the additional perfectly opaque upper level clouds that form in the GCM the net change in the infrared is still less than that due to the albedo effect. One possible explanation suggested by column C in Table 4 is that there is a simultaneous *decrease* in upper level cloudiness that accompanies the transition to solar transparency.

Finally, it is interesting to speculate on the nature of the interaction between global radiation and global cloud formation processes. Generally speaking, the formation of supersaturation (stratiform) clouds correlates well with atmospheric temperature. Thus, those processes that cool the atmosphere (i.e., albedo effects) produce more layered clouds, while those which warm the atmosphere (i.e., greenhouse effects) produce fewer. Layered clouds may thus be viewed as a positive feedback component of the system.

Convective clouds over the oceans behave in a manner similar to supersaturation clouds because of the decreased effect of surface temperature changes. Over land the importance of surface heating becomes evident, and convective cloudiness increases or decreases as the surface temperature becomes warmer or cooler. Convective clouds over land are in a sense a negative feedback component since their occurrence causes the surface energy balance to change in a direction that is unfavorable for their further development or maintenance.

It is tempting to assume that because layered clouds appear to be more prevalent than convective clouds in the global climatology, then the net feedback between total cloudiness and radiation acts in a positive sense. Such a statement would not be inconsistent with the results of this experiment (cf. Table 3, line 3). Clearly, there is a hierarchy of carefully controlled experiments that will need to be conducted to elucidate this question further.

Acknowledgments. We are indebted to Dr. Milton Halem and the staff of the Modelling and Simulation Facility for providing the support and resources needed to conduct these experiments. We appreciate the particularly constructive reviews of this paper offered by Profs. R. D. Cess and M. E. Schlesinger. Gerald Herman is supported by a NASA Faculty Research Associateship at the University of Wisconsin under NASA Grant NSG-5152.

REFERENCES

Cess, R. D., 1976: Climate change: An appraisal of atmospheric feedback mechanisms employing zonal climatology. *J. Atmos. Sci.*, 33, 1831–1843.

——, and V. Ramanathan, 1978: Averaging of infrared cloud opacities for climate modeling. *J. Atmos. Sci.*, 35, 919–922.

Ellis, J. S., 1978: Cloudiness, the planetary radiation budget, and climate. Ph.D. thesis, Colorado State University, 129 pp.

——, T. H. Vonder Haar, S. Levitus and A. H. Oort, 1978: The annual variation in the global heat balance of the earth. *J. Geophys. Res.*, 83, 1958–1962.

Herman, G. F., and R. Goody, 1976: Formation and persistence of summertime arctic stratus clouds. *J. Atmos. Sci.*, 33, 1537–1553.

——, and W. T. Johnson, 1978: The sensitivity of the general circulation to arctic sea ice boundaries. *Mon. Wea. Rev.*, 106, 1649–1664.

Hunt, G. E., 1977: Studies of the sensitivity of the components of the earth's radiation balance to changes in cloud properties using a zonally averaged model. *J. Quant. Spectros. Radiative Trans.*, 18, 295–307.

Hunt, B. G., 1978: On the general circulation of the atmosphere without clouds. *Quart. J. Roy. Meteor. Soc.*, 104, 91–102.

Lacis, A. A., and J. E. Hansen, 1974: A parameterization for the absorption of solar radiation in the earth's atmosphere. *J. Atmos. Sci.*, 31, 118–133.

Manabe, S., and R. F. Strickler, 1964: Thermal equilibrium of the atmosphere with a convective adjustment. *J. Atmos. Sci.*, 21, 361–385.

——, and R. T. Wetherald, 1967: Thermal equilibrium of the atmosphere with a given distribution of relative humidity. *J. Atmos. Sci.*, 24, 241–259.

Raschke, E., T. H. Vonder Haar, M. Pasternak and W. R. Bandeen, 1973: The radiation balance of the earth-atmosphere system from Nimbus 3 radiation measurements. NASA-TN-D7249 [NTIS-N-73-21702].

Schneider, S. H., 1972: Cloudiness as a global climatic feedback mechanism: The effect on the radiation balance and surface temperature of variations in cloudiness. *J. Atmos. Sci.*, 29, 1413–1422.

——, W. M. Washington and R. M. Chervin, 1978: Cloudiness as a global climatic feedback mechanism: Effects on cloud amount of prescribed global and regional surface temperature changes in the NCAR GCM. *J. Atmos. Sci.*, 35, 2207–2221.

Shapiro, R., 1971: The use of linear filtering as a parameterization of atmospheric diffusion. *J. Atmos. Sci.*, 28, 523–531.

Somerville, R. C. J., P. H. Stone, M. Halem, J. E. Hansen, J. S. Hogan, L. M. Druyan, G. Russell, A. A. Lacis, W. J. Quirk and J. Tennenbaum, 1974: The GISS model of the global atmosphere. *J. Atmos. Sci.*, 31, 84–117.

Reprinted from MONTHLY WEATHER REVIEW, Vol. 108, No. 12, December 1980
American Meteorological Society
Printed in U. S. A.

Sea Ice Simulations Based on Fields Generated by the GLAS GCM

CLAIRE L. PARKINSON

Laboratory for Atmospheric Sciences, NASA, Goddard Space Flight Center, Greenbelt, MD 20771

GERALD F. HERMAN[1]

Department of Meteorology, University of Wisconsin, Madison, 53706

(Manuscript received 19 May 1980, in final form 16 September 1980)

ABSTRACT

A four-month simulation of the thermodynamic portion of the Parkinson-Washington sea ice model was conducted using atmospheric boundary conditions that were obtained from a pre-computed seasonal simulation of the Goddard Laboratory for Atmospheric Sciences' General Circulation Model (GLAS GCM). The sea ice thickness and distribution were predicted for the 1 January–30 April period based on the GCM-generated fields of solar and infrared radiation, specific humidity and air temperature at the surface, and snow accumulation. The sensible heat and evaporative fluxes at the surface are mutually consistent with the ground temperatures generated by the ice model and the air temperatures generated by the atmospheric model.

In general, in the Northern Hemisphere the predicted ice distributions and the wintertime accretion and southward advance of the pack ice are well simulated. The computed ice thickness in the Southern Hemisphere appears reasonable, but the Antarctic melt season is extended, causing ice coverage to be less than observed in late March and April. During the Northern Hemisphere winter, the simulated ice accretion is the result of the net deficit of longwave radiation, heat gained from the ocean, and sensible heat lost to the atmosphere. In the early part of the Southern Hemisphere summer, the melting essentially balances the excess of solar over longwave radiation at the surface, while later in the simulation accretion balances the longwave and convective heat losses.

The results show that the Parkinson–Washington sea ice model produces acceptable ice concentrations and thicknesses when used in conjunction with the GLAS GCM for the January to April transition period. These results suggest the feasibility of fully coupled ice-atmosphere simulations with these two models.

1. Introduction

A frequently-cited goal in both general circulation studies and cryospheric research is the realistic modeling of the true interaction between sea ice processes and atmospheric processes. The relationship between the variations in the geographical distribution and physical properties of sea ice and the variations in the large-scale atmospheric circulation is obviously very complicated. Wind stress at the upper surface of the pack ice has long been accepted as the principal motive force for pack ice drift, while the energy balance and resultant ice temperature or rate of melting at the surface depend on atmospheric temperature, humidity, radiation and precipitation. At the same time, the fluctuations in the distribution and properties of sea ice may themselves be the cause of a range of atmospheric variations. The statistical relationship between ice and atmospheric processes has been well established through the observational analyses of Walsh and Johnson (1979) and others. Presumably the exact nature of the physical relationships will emerge from carefully designed modeling experiments in conjunction with data-based studies.

The study of the large-scale relationships between the sea ice and the atmosphere through numerical methods has thus far involved models which can be classified into three broad categories: (1) Sea ice models which depend upon but do not alter the atmospheric forcings (e.g., stress or radiation) that are specified from observational data or from atmospheric models; (2) Atmospheric models in which sea ice is a prescribed lower boundary condition that remains independent of the simulated atmospheric fields; (3) Fully coupled ice-atmosphere models in which the ice distribution and atmospheric fluxes are determined in a mutually consistent fashion.

In the first of these, which may be termed *non-interactive ice models*, the motion and thickness of sea ice are calculated from time-dependent mechanical and thermodynamic equations which require as boundary conditions such variables as the stress and the turbulent and radiative energy fluxes at the ice-atmosphere interface and at the ice-ocean interface.

[1] Also NASA Goddard Laboratory for Atmospheric Sciences.

0027-0644/80/122080-12$07.00

TABLE 1. Summary of large-scale sea ice models.

Model	Description	Required atmospheric parameters
1. Hibler (1979)	Dynamic with specified thermodynamics; simulation for full yearly cycle; Arctic Basin	Surface pressure; specified thermodynamic growth rates
2. Kulakov *et al.* (unpublished)	Dynamic-thermodynamic; 1 month simulation; South Polar region	Surface air temperature, pressure, and total radiation
3. Ling *et al.* (1980)	Dynamic; 18-day simulation; Weddell Sea	Surface air pressure
4. Parkinson and Washington (1979)	Dynamic-thermodynamic; simulation for full yearly cycle; North and South Polar regions	Surface air temperature, dew point, and geostrophic wind velocity
5. Pritchard *et al.* (1977)	Dynamic-thermodynamic; 10-day simulation; portion of Beaufort Sea	Surface air pressure
6. [illegible]rock (1975)	Dynamic; simulation for long-term average conditions; Arctic Basin	Surface air pressure
7. Washington *et al.* (1976)	Thermodynamic; simulation for full yearly cycle; North and South Polar regions	Surface air temperature, dew point, and geostrophic wind speed

In these models the changing character of the ice field does not alter the atmospheric forcing at the boundary, and consequently some of the conditions may be viewed as unrealistic, since the forcing may be inconsistent with the actual state of the ice. As an example, the stress at the surface depends upon the surface geostrophic wind and the drag characteristics of the ice; but in a non-interactive ice model the stress field would generally not readjust to the changing ice conditions. A summary of major large-scale ice models together with their required atmospheric inputs is given in Table 1.

In the second set of models, which we term *non-interactive atmospheric models*, the effective pack ice distribution is usually realized through the specified surface emissivity and reflectivity required in the atmospheric radiation calculations, through the temperature and wetness of the surface in thermodynamic calculations, and through the surface roughness in the horizontal momentum equation. The distribution and properties of the ice may vary with time according to a predetermined climatology, but they remain independent of the model-generated fields. Most operational weather forecasting models, and most versions of current GCMs (Table 2) are non-interactive with respect to sea ice.

Non-interactive atmospheric models have been used in a number of investigations of the role of sea ice in global climate. These include the ice-free Arctic Ocean experiments of Warshaw and Rapp (1973), the ice age experiments of Williams *et al.* (1974), and the marginal ice zone experiments of Herman and Johnson (1978). It is sometimes noted that in these experiments the simulated effect of the sea ice may be somewhat exaggerated because the experiments contain no ice-atmosphere feedback. For example, if the principal effect of reducing sea ice concentration is to increase the transfer of sensible heat to the atmosphere, then in nature a negative feedback is involved because the cooling of the ocean surface due to its heat loss to the atmosphere may be large enough to cause more ice to accrete. There is a positive feedback as well, involving the reflectivity of sea ice and the surface energy balance and surface temperature.

Fully coupled ice-atmosphere models, the third category listed above, allow the distribution of sea ice to evolve as part of the solution to the complete system of equations governing atmospheric and sea ice processes. A wide range of highly parameterized climate models fall into this category (for a review, see Saltzman, 1978); but, so far, there have been very few experiments with fully coupled ice-atmos-

TABLE 2. Sea ice specification in general circulation models.

Model	Treatment
1. GLAS (Halem *et al.*, 1979)	Fixed 3 m slab; specified variation of margin
2. GFDL (Manabe and Wetherald, 1980)	Occurrence depends on surface energy balance of ocean
3. GFDL-coupled (Manabe *et al.*, 1979)	Thickness and concentration depend on energy balance of ocean surface layer
4. NCAR (Washington and Williamson, 1977)	Specified January and July margin affecting only shortwave albedo
5. NCAR (Washington *et al.*, 1980)	Varies according to 1-dimensional energy balance model
6. Oregon State/UCLA (Schlesinger and Gates, 1979)	Fixed 3 m slab with prescribed margin variations
7. Meteorology Office (Corby *et al.*, 1972)	Prescribed slab

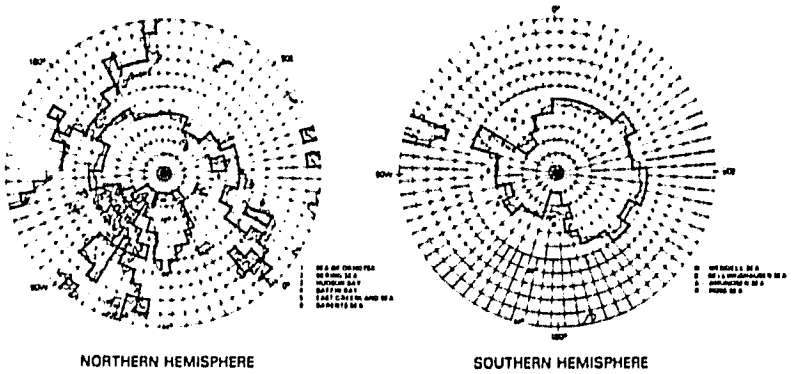

FIG. 1. Grid structure. Heavy solid line indicates the model resolution of continental boundaries.

phere general circulation models. The results of recent experiments with the coupled ice-atmosphere-ocean model at the Geophysical Fluid Dynamics Laboratory (GFDL) (Manabe *et al.*, 1975) have illustrated some of the difficulties. There, for example, the reduction in surface albedo due to melting sea ice caused anomalous heating in the south polar regions, while excessive ice growth in the Arctic, along with the absence of leads, limited the amount of heat that was conducted to the surface. This excessive growth was eliminated in later versions (Manabe *et al.*, 1979) in which the mean annual solar radiation was replaced with a realistic seasonal cycle. At the National Center for Atmospheric Research (NCAR), an *asynchronous coupling* has been performed with atmosphere, ocean and ice models. The atmospheric model was run individually for January, April, July and October; the resulting data were fitted to an annual curve which then drove the ocean model for a 5-year simulation; the new sea surface temperature and sea ice distributions were then used as revised boundary conditions for the atmospheric calculations. In general the sea ice distributions resulting from the simulation were thinner and less extensive than the observed (Washington *et al.*, 1980).

It is quite possible that one of the reasons that the fully non-interactive GCMs perform as well as they do in polar regions (e.g., Herman and Johnson, 1980) lies in their climatologically fixed sea ice margins and ocean temperatures and in the constraint which these place on the radiative and convective fluxes at the surface. It is thus not entirely unexpected that the first attempts at coupled simulations have produced additional difficulties.

The results reported here represent a preliminary step in assessing the feasibility of coupled ice-atmosphere simulations. This work is designed to demonstrate whether the thermodynamic portion of the sea ice model of Parkinson and Washington (1979) can predict a realistic seasonal variation of ice thickness and ice concentration when forced by the fields generated by a seasonal simulation with the GCM of the Goddard Laboratory for Atmospheric Sciences. It is important to note that we have not conducted a fully-coupled experiment, but rather have forced a non-interactive ice model with the precomputed results of a non-interactive GCM. A principal difficulty lies in assessing whether the success or failure of the results should be attributed to the atmospheric GCM or to the sea ice model and whether specific deficiencies will be reduced or enhanced when the two models are actually coupled.

2. Summary of models

The model calculations are carried out on the grid of the GLAS GCM. Horizontal grid resolution is defined by 5° longitude and 4° latitude spacing, with the grid squares centered at longitudes 0°, 5°E, . . . , 355°E and at latitudes 90°S, . . . , 6°S, 2°S, 2°N, 6°N, . . . , 90°N. This yields a grid size of 72 × 46 for the globe.

The current version of the GLAS GCM incorporates a *split grid* at high latitudes, with the longitudinal resolution doubled to 10° for latitudes 64–80° and doubled again to 20° for latitudes poleward of 80° (Fig. 1). For the sea ice calculations we have retained the full 72 × 46 grid size, and have interpolated the GCM grid point values to the off-split grid points.

a. Thermodynamic sea ice model

The sea ice model employed for the simulations is a thermodynamic model which calculates a lead percentage within the ice but does not simulate ice dynamics. It is essentially the thermodynamic portion of the three-dimensional model of Parkinson and Washington (1979), a model based in part on the one-dimensional models of Maykut and Untersteiner (1971) and of Semtner (1976). The Parkinson

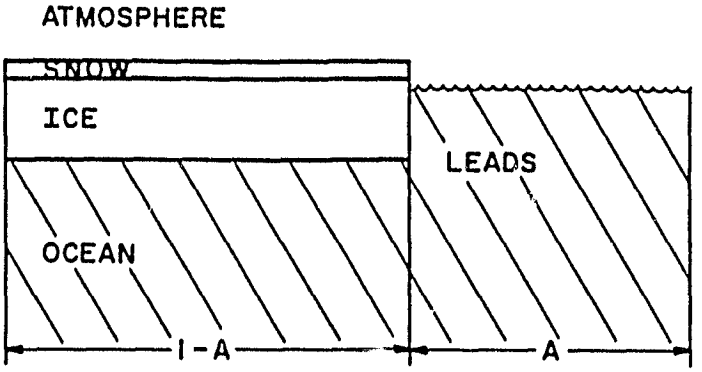

FIG. 2. Schematic of major divisions within a grid element.

and Washington model was developed for and run previously with mean monthly climatological data as input, contrasting with the GCM-generated data used here. The results of the climatological simulation can be found in Parkinson and Washington. Note that we are assuming that a reasonable simulation of ice thickness and distribution can be obtained when the details of ice dynamics and mechanics are explicitly neglected. This assumption is supported by the results of Parkinson and Washington, which show that the insertion of the dynamics did not substantially alter the model results from an earlier, strictly thermodynamic simulation.

Fig. 2 illustrates the basic model elements at an individual grid square. Uniform ice and snow layers cover a portion of the area, with the remainder covered by leads or open water. The fractional area A of leads and the thicknesses of the ice and snow are time dependent, being recalculated at each of the 6-hourly time steps. Depending on time and location, the snow layer or both the ice and snow layers may be non-existent.

The calculations for thickness changes are based on energy balances at the various interfaces. The fluxes between the upper snow surface and the atmosphere are sensible and latent heat H and LE respectively, incoming longwave radiation LW, incoming shortwave radiation SW, and emitted longwave radiation from the surface to the atmosphere. The only fluxes through the ice and snow are conductive, and there is also a flux to the undersurface of the ice from the ocean, F_0.

Formation of energy balances at the air-snow and snow-ice interfaces yields the pair of equations:

$$H + LE + \epsilon LW + (1 - \alpha)SW + \epsilon\sigma T_{sfc}^4 + \frac{k_s}{h_s}(T_I - T_{sfc}) = 0 \quad (1)$$

$$\frac{k_s}{h_s}(T_I - T_{sfc}) = \frac{k_I}{h_I}(T_B - T_I) \quad (2)$$

where ϵ is the longwave emissivity and α the shortwave albedo of snow; σ is the Stefan-Boltzmann constant; T_{sfc}, T_I and T_B are the temperatures at the upper snow surface, the snow-ice interface and the bottom ice surface respectively; k_s, k_I are the conductivities of the snow and ice respectively; and h_s, h_I are the snow and ice layer thicknesses.

Eqs. (1) and (2) are solved for T_I and T_{sfc}. If the calculated value of T_{sfc} exceeds the freezing point, the surface temperature is set exactly at freezing and the remaining energy is used to melt a portion of the snow. Otherwise, the snow thickness is increased by the snowfall amount obtained from the GCM.

At the bottom surface of the ice, the amount of ablation or accretion is calculated by balancing the energy flux from this change of state with the ocean heat flux and the conductive flux. This results in the following thickness change:

$$\Delta h_I = \frac{\Delta t}{Q_I}\left[\frac{k_I}{h_I}(T_B - T_I) - F_0\right] \quad (3)$$

where Δt is the time step (equal to 6 h) and Q_I is the heat of fusion of ice.

In grid squares where no ice exists or where ice exists but without a snow cover, the calculations are similarly based on energy balances, although with the following adjustments. In the case of no ice, the net energy flux into the ocean mixed layer is used to adjust the water temperature, with a small amount of ice being formed when the temperature reaches freezing; no account is taken of heat transport in the ocean or local upwelling effects. In the case of ice with no snow cover, the surface energy balance is constructed similarly to Eq. (1), with a modification to account for the penetration of shortwave radiation into the ice. Details are provided in Parkinson and Washington.

The lead percentage is parameterized by calculating the net energy input into the lead and distributing this energy to the lead itself and to the surrounding ice. In the event of a positive net input, the energy heats the water and laterally melts the ice, with the

partition of energy being proportional to the lead area. In the event of a negative net input (energy loss), the energy deficit is balanced by cooling the water, and, if the water temperature reaches freezing, then by laterally accreting new ice onto the existing ice.

b. The GLAS General Circulation Model

The principal features of the GLAS General Circulation Model have been described by Somerville *et al.* (1974), Stone *et al.* (1977), and Halem *et al.* (1979). Aspects of the model which are particularly relevant for high latitude studies have been discussed by Herman and Johnson (1978, 1980). Here it suffices to note that the GLAS GCM is a primitive equation model utilizing a sigma vertical coordinate system and 4° latitude by 5° longitude horizontal spacing. Computational stability at high latitudes is ensured through the use of the split grid; heat and moisture fluxes at the surface are computed through simple drag laws; and sea surface temperatures and sea ice margins are specified to vary smoothly according to a predetermined climatology.

More specifically, for the radiative fluxes needed in the present experiment, the GCM solar radiation is determined by the 2-stream calculation of Lacis and Hansen (1974) and the longwave radiation is based on an algorithm developed by Wu and Kaplan (Wu, 1980). The Lacis and Hansen formulation includes a detailed representation of atmospheric absorption and scattering, while the Wu and Kaplan formulation includes 10 regions in the water vapor spectrum. Both radiation calculations are fully interactive with the model-generated distributions of water vapor, cloudiness, and surface albedo. These radiation calculations are considerably more elaborate than those used when the sea ice model was run independently of the GCM (cf. Parkinson and Washington).

The simulated polar climatology of the GLAS GCM is discussed in detail by Herman and Johnson (1980). In the Arctic and peripheral Arctic oceans the simulated wintertime distributions of sea level pressure and surface energy fluxes are realistic, although surface air temperatures are 5–9°C too warm. Over the peripheral Antarctic oceans the belt of low pressure centers around the continent is not simulated as a result of the GCM's difficulty in simulating baroclinic eddy activity in the high latitudes of the Southern Hemisphere. Temperatures and energy fluxes are not unreasonable, although validation is difficult because of the lack of observed data.

3. Description of experiment

The fields needed for the ice calculations (Section 2a) are sensible and latent heat, longwave and shortwave radiation incident at the surface, and snowfall. The incoming longwave, incoming shortwave, and precipitation terms are taken directly from fields generated by the GCM, while the sensible and latent heat terms are calculated by bulk aerodynamic formulae which require from the GCM values for surface air temperature, wind speed, and surface specific humidity. These fields are entered into the calculations at each ice model timestep, i.e., every 6 h.

The GCM fields were generated by a 4-month simulation initialized from NMC conditions at 00 GMT 1 January 1975. The principal features of this simulation (GLAS Reference No. D122) have been analyzed in detail by Halem *et al.* (1979).

The ice model requires initial conditions for sea ice concentrations and thicknesses, and for the surface temperatures of the ocean, ice and snow. The initial ice concentrations were approximated from maps of average brightness temperature recorded by the Electronically Scanning Microwave Radiometer (ESMR) on Nimbus 5 over the 3-day period 30 December 1974–1 January 1975. A description of the ESMR data set is provided in Zwally and Gloersen (1977). As satellite data is not yet able to provide thickness estimates, the initial thickness distributions were estimated based on climatology. These initial ice conditions are mapped in Fig. 3. The initial ocean surface temperature at each grid square is either the initial GCM ocean temperature or the freezing point of sea water, whichever is larger; while the initial snow and ice surface temperatures are either the initial GCM snow and ice temperatures or the freezing point, whichever is smaller.

It is important to note that while the initial conditions for the GCM and the ice are based on January 1975 data, the present experiment is not designed to predict 1975 ice conditions. It is commonly accepted that, after some period of time ranging from several days to several weeks, the simulated GCM fields become essentially independent of the prescribed initial state, and more characteristic of the model's internal dynamical adjustment to the boundary conditions and external forcing. Thus, it is more correct to consider the sea ice model as being forced by the GLAS model climatology, rather than by a simulated 1975 atmospheric circulation.

It also follows that since the model-generated fields result in part from the GCM's adjustment to the boundary conditions (e.g., sea surface temperature, ice margin, surface albedo), the various atmospheric fields that force the sea ice model will actually contain some structure that is determined by the observed climatological surface boundary conditions. The computed sea ice fields thus may be anchored to an uncertain degree to the climatological ice conditions through the GCM's distribu-

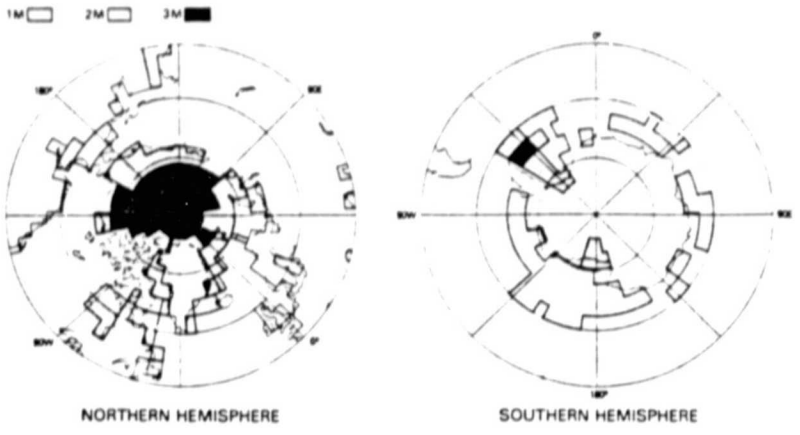

FIG. 3. Initial ice thickness (m) on 1 January.

tion of precipitation, radiation, etc. The effect of all of the physical processes which determine the distribution of sea ice in nature, including large-scale ice and ocean dynamics, is thereby implicitly communicated by the GCM to the sea ice model.

4. Results and discussion

a. Spatial fields of ice thickness and concentration

Selected results of the simulation are shown in Figs. 4–7. The Northern Hemisphere ice extents slowly move equatorward from January to March, first expanding southward in the Sea of Okhotsk in early January, then in the western Bering and Barents seas in late January. In February the extent is stable both in the Sea of Okhotsk and to the east of Greenland; there is a slight advance to the southwest of Greenland, and there are small regions of advance compensated by small regions of retreat in both the Bering and Barents seas. The ice begins its retreat in the Okhotsk and Bering seas in March and is in retreat in all sectors during April (Figs. 3–7).

To the extent that 1975 ice conditions are representative of climatology, it is possible to use 1975 data from the ESMR on Nimbus 5 to evaluate broad aspects of the ice model's simulation. The overall simulated distribution of Northern Hemisphere ice corresponds fairly well with the observed. However, there are discrepancies between the observations and the simulation. For instance, in the Sea of Okhotsk the observed ice advance occurs predominantly in February rather than in January, though the maximum extent in both cases is reached in early March, with some slight retreat in late March. The simulated full ice cover through April in Hudson Bay is confirmed in the observations, although the observations do not confirm as extensive an ice cover as is simulated in February in the Barents Sea. The situation in the Barents Sea can probably be explained by the failure to represent the warm, northward flowing ocean current to the west of Scandinavia.

In the Southern Hemisphere, the simulated ice edge remains steady for the first half of January, then in the latter half of January retreats significantly around most of the Antarctic continent except in the Weddell and Bellingshausen seas. There

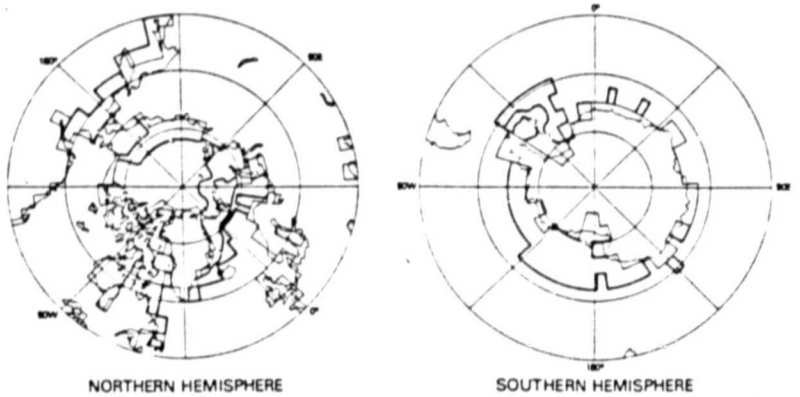

FIG. 4. Simulated ice thickness (m) on 1 February. Heavy lines show the ice edge and contours of ice thickness. Lighter lines show the continental boundaries and grid resolution of those boundaries.

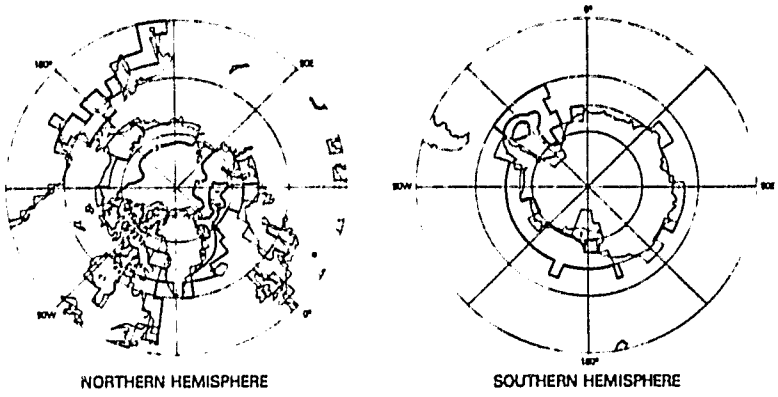

FIG. 5. Simulated ice thickness (m) on 1 March.

is continued retreat of the little ice remaining off the coast of East Antarctica during February, with essentially no East Antarctic ice left by 1 March. In February there is also continued edge retreat to the north and northeast of the Ross Sea, though the edge positions in the Weddell and Bellingshausen seas are maintained. In March the East Antarctic situation remains stable with practically no ice; the Bellingshausen Sea still shows no change in ice extent; and both the Ross and Weddell seas lose some ice in their northernmost regions and gain some in their southernmost regions. During April there is no further edge retreat in any region and there is significant expansion around the coast of East Antarctica and in the Weddell Sea (Figs. 3–7).

The 1975 ESMR imagery (unpublished) for the Southern Hemisphere confirms the relatively stable position of the ice edge in early January and the ice retreat in the East Antarctic and Ross Sea during late January and during February. However, the ESMR observations also indicate considerable ice advance during March, which would suggest a model delay of ½–1 month in the start of the fall growth season. A likely cause of this delay may be the unrealistically high surface air temperatures which characterize the GLAS GCM's Antarctic climatology. For instance, in mid-February, the 270 K isotherm of the GCM values closely follows the Antarctic coastline around most of the continent, the major exception occurring in the Weddell Sea, where the contour is further north than the coast. Thus, with the exception of the Weddell Sea, very little of the model's Southern Ocean is overlain by air with temperatures below 270 K. Based on observed climatological averages for the month of February, these simulated temperatures would be anomalously warm and thus would explain the delay in the refreezing of the surface water.

For more detail on the simulated ice thickness and concentration values, the time sequences of these quantities are tabulated in Table 3 for three specific regions: the Weddell Sea in the Southern Hemisphere and the East Greenland Sea and Central Arctic Basin in the Northern Hemisphere. The calculations for Table 3 involved all grid squares which contained ice irrespective of its concentration. The concentration value listed is the average value for the ice-laden grid squares, and the thickness listed is the average ice thickness, without regard to concentration.

In the Weddell Sea, the concentrations and thick-

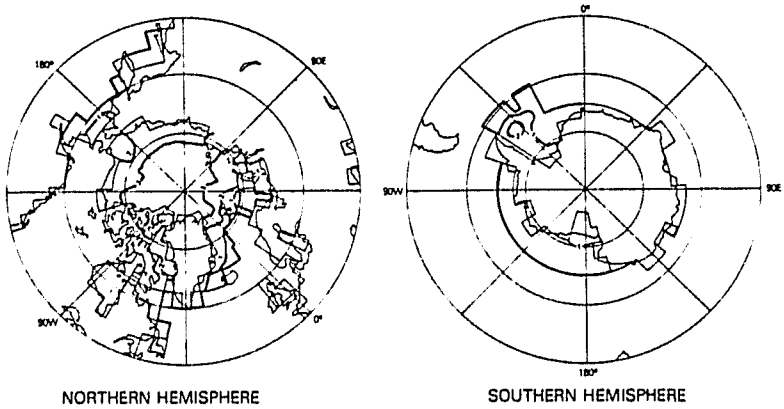

FIG. 6. Simulated ice thickness (m) on 1 April.

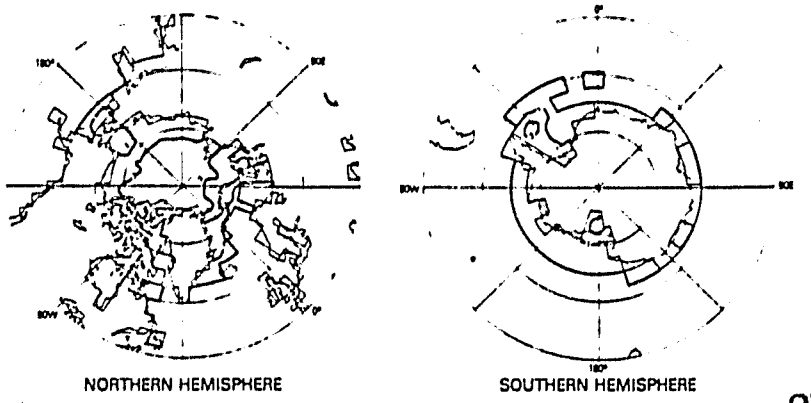

FIG. 7. Simulated ice thickness (m) on 29 April.

nesses steadily decrease during January and February as expected for the summer melt period. Two grid squares lose their ice cover in early March, with the result that the minimum ice extent occurs in mid-March. The ESMR satellite imagery for all four years available (1973–76) shows a slight increase in ice extent from the start to the middle of the month, suggesting that the numerical model has extended the summer melt period about 2 weeks beyond what the observations would indicate. For the month and a half after 15 March, the simulated ice concentrations rapidly increase, as would be expected for this early fall season. The thickness decreases from 15 March to 15 April, a result of averaging into the calculations newly ice-laden grid squares with very thin ice covers.

In the Central Arctic, averaged ice concentrations are initialized at 98.8%, increase to 99.5% by mid-February and then remain at this maximum-allowable value for the remainder of the simulation. The central Arctic thickness values slowly increase over the four-month simulation. These results are in general agreement with the expected trends for the central Arctic region.

The East Greenland Sea situation is somewhat more complicated since the number of grid squares involved changes over the simulation period. The increase in area of ice-laden waters from 1–15 January can easily account for the decrease in average ice thickness from 1.62 to 1.51 m. However, the continued, though less rapid, decrease in thickness through the end of March cannot be so explained, and this is presumably an unrealistic result. By contrast, the increase in ice concentration over the same period is reasonable.

b. Regionally-averaged energy balances

We illustrate in Figs. 8–10 the evolution of the areal averages of the principal GCM-generated parameters to which the ice model responds, and of the main components of the surface energy and mass balance. The GCM communicates to the ice model precipitation (i.e., snowfall), surface air temperature, specific humidity, and solar and incoming longwave radiation, the latter two variables being functions of ambient cloudiness. Evaporation and sensible heat exchange at the surface are based on GCM-generated

TABLE 3. Regionally-averaged ice thickness and concentration.

Date	Weddell Sea			East Greenland Sea			Central Arctic		
	Area of ice-laden waters (10^6 km^2)	Concentration (%)	Thickness (m)	Area of ice-laden waters (10^6 km^2)	Concentration (%)	Thickness (m)	Area of ice-laden waters (10^6 km^2)	Concentration (%)	Thickness (m)
1 January	2.6	47.0	1.72	1.2	53.0	1.62	2.8	98.8	2.98
15 January	2.6	41.7	1.53	1.3	72.3	1.51	2.8	99.2	3.01
1 February	2.6	36.4	1.30	1.3	76.4	1.47	2.8	99.3	3.04
15 February	2.6	33.4	1.19	1.3	82.2	1.45	2.8	99.5	3.08
1 March	2.6	31.6	1.10	1.3	83.2	1.43	2.8	99.5	3.11
15 March	2.4	35.5	1.13	1.3	86.3	1.34	2.8	99.5	3.14
1 April	2.6	54.7	1.02	1.3	89.1	1.29	2.8	99.5	3.18
15 April	2.8	79.3	0.96	1.3	87.0	1.33	2.8	99.5	3.21
29 April	2.8	88.9	1.01	1.2	90.6	1.36	2.8	99.5	3.23

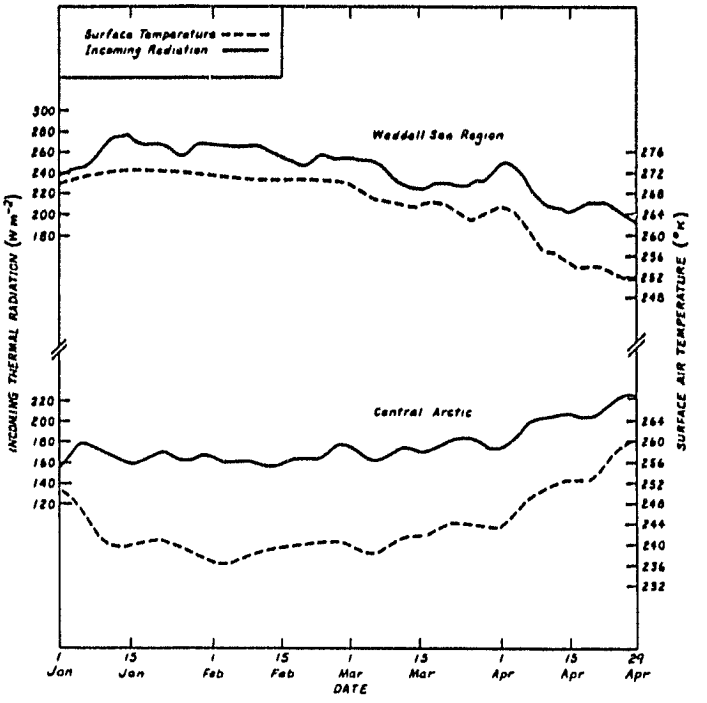

FIG. 8. GCM-generated surface temperature (broken line) and incoming longwave radiation for Weddell Sea Region (top) and Central Arctic Basin (bottom).

surface air temperatures and specific humidities, and the temperature and saturation vapor pressure produced by the ice model for the ice, snow and ocean surfaces. Thus, the surface fluxes are not interpreted as GCM fluxes, but rather as those fluxes which are mutually consistent with the respective temperatures generated by the ice and atmospheric models.

The evolution of the average GCM infrared radiation and surface temperature fields for the Weddell Sea region of the Southern Hemisphere is shown in the upper half of Fig. 8. Throughout most of January and February the surface air temperature is controlled by the melting sea ice, and remains near 272 K. The temperature decreases through March and April to 252 K, except for brief warmings which occur during mid March and early April. This behavior is in general agreement with the climatologies of surface stations near the Weddell Sea compiled by Schwerdtfeger (1970). Incoming longwave radiation during the first two months of the simulation period is about 260 W m^{-2} and decreases to 210–240 W m^{-2} during the latter two-month period, which is in general agreement with the zonal mean values obtained by Sasamori *et al.* (1972). Approximately 12 cm of snowfall (not shown) accumulates by the end of April.

The components of the Weddell Sea surface energy balance are shown in Fig. 9. GCM generated solar radiation is highly variable, and decreases from its 1 January value of 170 Wm^{-2} to 10 Wm^{-2} by the end of April. During the first half of the integration period the temperature difference between the air and ocean is small, and so consequently are the fluxes of sensible heat, latent heat and conduction. During most of this two-month period in the Weddell Sea the surface energy balance is governed largely by incoming radiation: The excess of solar radiation absorbed over net infrared radiation results in a warming of the ocean mixed layer and a decrease of ice volume, due to decreases in both thickness and concentration. During the latter half of the period the solar input becomes very small and the colder surface air temperatures are responsible for large evaporative and sensible heat fluxes from the ocean surface. The energy balance is strongly negative, and this is balanced jointly by ice accretion and further cooling of the mixed layer.

It is interesting to note how well the features of surface air temperature, surface energy fluxes, ice volume, and mixed layer temperature correlate with one another during March and April. For example, near the end of March there occurred in the GCM a brief warming of air temperatures and an increase in downwelling radiation. The regional response was rapid: Evaporation and convection from the surface diminished, ice accretion diminished and warming of the ice and ocean occurred. Clearly, evaporation and convection couple the ice model to the GCM in a rapid and efficient manner.

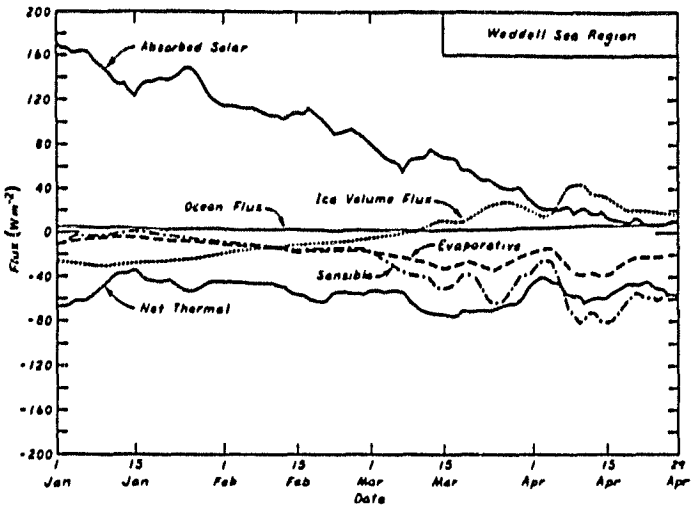

FIG. 9. Components of energy balance for ice in the Weddell Sea.

The smoothed GCM forcing parameters and resultant energy and mass budgets for the Central Arctic are shown in the lower half of Fig. 8 and in Fig. 10. Solar radiation is obviously irrelevant for the Central Arctic during most of this period. The incoming longwave radiation from the GCM is 160–180 Wm^{-2}, increasing toward the end of the integration period and agreeing reasonably well with the climatological values used by Maykut (1978). Approximately 24 cm of snow accumulated in the Central Arctic during this period, which is probably excessive. Observations show that typical wintertime accumulation is about 5 cm (Maykut and Untersteiner, 1971). Apparently this discrepancy did not cause any serious error in the simulated ice thickness. However, the melting of this excess snow would likely be a source of error if the integration were extended into the summer season. The GCM-generated Arctic surface air temperatures evolve in a realistic way as compared with observed climatologies (cf., Vowinckel and Orvig, 1970).

The components of the surface energy balance in the Central Arctic behave in a relatively simple fashion during this period. The evaporative heat flux is essentially zero because of the cold temperatures and resultant low atmospheric moisture capacity. The longwave energy lost from the surface is almost entirely compensated for by the sensible heat gained from the atmosphere and the energy conducted up from the ocean. The time series of sensible heat and radiative fluxes are similar to one another, and this again illustrates the strong coupling between GCM-generated radiation fields and ice model generated surface temperatures. The net energy loss

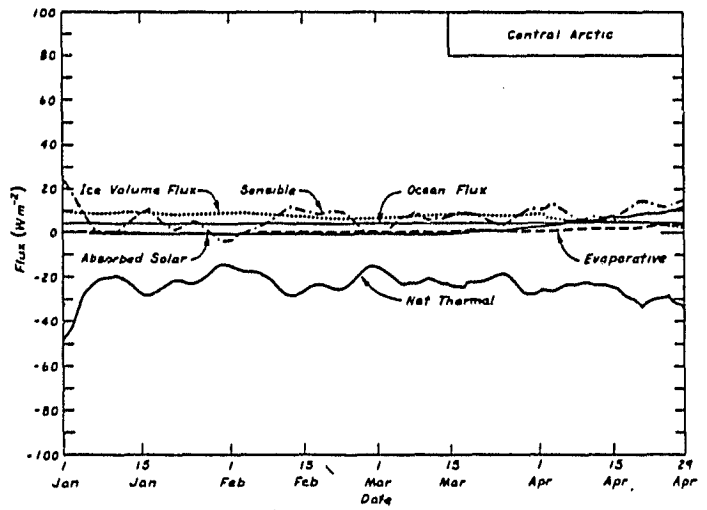

FIG. 10. Components of energy balance for ice in the Central Arctic.

from the entire layer of ice is about 10 Wm^{-2}, and this results in the accretion of about 18 cm of ice.

5. Summary and conclusions

The results of these experiments provide a number of useful insights into the problem of constructing coupled atmosphere-ice-ocean general circulation models. Most significantly, it appears that the GLAS GCM is capable of generating atmospheric fields in the Arctic and Antarctic that are sufficiently precise and accurate to produce reasonable distributions of sea ice when used in conjunction with a thermodynamic sea ice model. This conclusion is of course limited to the four-month period investigated. Systematic errors in the GCM's radiation were originally a source of concern given the typical sensitivity (e.g., Maykut and Untersteiner, 1971) of thermodynamic ice models to anomalies in the atmospheric fluxes. Also unknown was the response of the ice model to the large variations in atmospheric fluxes that occur in the GCM from time step to time step and from grid point to grid point. The ice model proves fairly insensitive to these nearly random fluctuations, and in fact integrates them into relatively smooth distributions of ice thickness and concentration. Obviously the effect of *systematic* errors will be a source of concern as the integration time of the GLAS GCM is extended to several seasons or years.

Most encouraging was the success in simulating the gross variations of the sea ice concentration in the Central Arctic, East Greenland Sea, Barents Sea, and Bering Sea sectors. Ice thickness in the Central Arctic agrees reasonably well with the observed average thickness of 3 m. The spatial trend recently reported by Hibler (1979) was not incorporated in the initial conditions and did not appear in the results. Perhaps a longer simulation and the incorporation of ice dynamics would produce these spatial variations.

The summer decay season of the ice simulated in the Antarctic extends several weeks beyond the normal observed ice minimum. This unrealistic behavior of the ice in the Southern Hemisphere is probably related to GCM errors in the high southern latitudes (Herman and Johnson, 1980), since the same sea ice model has demonstrated reasonable behavior in the Antarctic when forced with observed climatological data (Parkinson and Washington, 1979). The GCM-driven simulation does reproduce the fall-season extension of the ice, the major difficulty being simply that this growth is delayed for several weeks in early March.

The sensitivity of ice thermodynamics to the incoming radiation fields is troublesome. The solar and thermal fluxes generated by a GCM depend on the radiation model employed and, equally importantly, on a set of difficult-to-measure empirical parameters that determine atmospheric absorption. These include gaseous transmission, aerosol content and aerosol optical properties, cloudiness and cloud optical properties. The large uncertainty in measuring Arctic stratus cloud absorptance, for example, has been noted by Herman (1977), and one limit to the predictability of ice thickness is clearly imposed by such uncertain atmospheric parameters. The effect of systematic errors in the GCM-generated surface air temperatures and specific humidities, as well as in snowfall rates, remains to be investigated.

The ice model utilized here is principally a thermodynamic model; later experiments will be conducted with versions that will account for ice dynamics and mechanics, and the salinity structure of the oceanic mixed layer. Before successful fully coupled simulations are understood there are a range of sensitivity experiments that need to be conducted with these various models for integration periods extending to several seasons or years.

Acknowledgments. We are indebted to Drs. M. Halem and H. J. Zwally for providing the resources and facilities that were necessary for these experiments. The programming support of Messrs. M. Good and W. Johnson is especially acknowledged. G. F. Herman is supported at the University of Wisconsin under NASA Grant NSG-5152.

REFERENCES

Bryan, K., S. Manabe, and R. C. Pacanowski, 1975: A global ocean-atmosphere climate model. Part II. The oceanic circulation. *J. Phys. Oceanogr.*, 5, 30–46.

Corby, G. A., A. Gilchrist, and R. L. Newson, 1972: A general circulation model of the atmosphere suitable for long period integrations. *Quart. J. Roy. Meteor. Soc.*, 98, 809–832.

Halem, M., J. Shukla, Y. Mintz, M. L. Wu, R. Godbole, G. Herman, and Y. Sud, 1979: Comparison of observed seasonal climate features with a winter and summer numerical simulation produced with the GLAS general circulation model. Report of the JOC Study Conf. on Climate Models: Performance, Intercomparison and Sensitivity Studies, *GARP Publ. Series No. 22*, 207–253, WMO, Geneva, Switzerland.

Herman, G. F., 1977: Solar radiation in Arctic stratus clouds. *J. Atmos. Sci.*, 34, 1423–1432.

Herman, G. F., and W. T. Johnson, 1978: The sensitivity of the general circulation to Arctic sea ice boundaries: A numerical experiment. *Mon. Wea. Rev.*, 106, 1649–1664.

Herman, G. F., and W. T. Johnson, 1980: Arctic and Antarctic climatology of the GLAS General Circulation Model. *Mon. Wea. Rev.*, 108, 1974–1991.

Hibler, W. D., III, 1979: A dynamic thermodynamic sea ice model. *J. Phys. Oceanog.*, 9, 815–846.

Lacis, A. A., and J. E. Hansen, 1974: A parameterization for the absorption of solar radiation in the earth's atmosphere. *J. Atmos. Sci.*, 31, 118–133.

Ling, C. H., L. A. Rasmussen, and W. J. Campbell, 1980: A continuum sea ice model for a global climate model. *Sea Ice Processes and Models*, R. Pritchard, Ed., University of Washington Press, 187–196.

Manabe, S., K. Bryan, and M. J. Spelman, 1975: A global ocean-atmosphere climate model. Part I. The atmospheric circulation. *J. Phys. Oceanogr.*, 5, 3–29.

Manabe, S., K. Bryan, and M. J. Spelman, 1979: A global ocean-atmosphere climate model with seasonal variation for future

studies of climate sensitivity. *Dyn. Atmos. Oceans*, 3, 393–426.

Manabe, S., and R. T. Wetherald, 1980: On the distribution of climate change resulting from an increase in CO_2 content of the atmosphere. *J. Atmos. Sci.*, 37, 99–118.

Maykut, G. A., 1978: Energy exchange over young sea ice in the Central Arctic. *J. Geophys. Res.*, 83, 3646–3658.

Maykut, G. A., and N. Untersteiner, 1971: Some results from a time-dependent, thermodynamic model of sea ice. *J. Geophys. Res.*, 76, 1550–1575.

Parkinson, C. L., and W. M. Washington, 1979: A large-scale numerical model of sea ice. *J. Geophys. Res.*, 84, 311–337.

Pritchard, R. S., M. D. Coon, and M. G. McPhee, 1977: Simulation of sea ice dynamics during AIDJEX. *J. Pressure Vessel Tech.*, 99, 491–497.

Rothrock, D. A., 1975: The steady drift of an incompressible Arctic ice cover. *J. Geophys. Res.*, 80, 387–397.

Saltzman, B., 1978: A survey of statistical-dynamical models of the terrestrial climate. *Advances in Geophysics*, Vol. 20, Academic Press, 184–295.

Sasamori, T., J. London, and D. Hoyt, 1972: Radiation budget of the Southern Hemisphere. *Meteor. Monogr.*, No. 35, Amer. Meteor. Soc., 9–22.

Schlesinger, M. E., and W. L. Gates, 1979: Performance of the Oregon State University two-level atmospheric general circulation model. Report of the JOC Study Conf. on Climate Models: Performance, Intercomparison and Sensitivity Studies, *GARP Publ. Series No. 22*, 139–206, WMO, Geneva, Switzerland.

Schwerdtfeger, W., 1970: The climate of the Antarctic. In: *World Survey of Climatology*, Vol. 14, *Climates of the Polar Regions*. S. Orvig, Ed., Elsevier, 370 pp.

Semtner, A. J., Jr., 1976: A model for the thermodynamic growth of sea ice in numerical investigations of climate. *J. Phys. Oceanogr.*, 6, 379–389.

Stone, P. H., S. Chow, and W. J. Quirk, 1977: The July climate and a comparison of the January and July climates simulated by the GISS general circulation model. *Mon. Wea. Rev.*, 105, 170–194.

Somerville, R. C. J., P. H. Stone, M. Halem, J. E. Hansen, J. S. Hogan, L. M. Druyan, G. Russell, A. A. Lacis, W. J. Quirk, and J. Tenenbaum, 1974: The GISS model of the global atmosphere. *J. Atmos. Sci.*, 31, 84–117.

Vowinckel, E. and S. Orvig, 1970: The climate of the north polar basin. In: *World Survey of Climatology*, Vol. 14, *Climates of the Polar Regions*. S. Orvig, Ed., Elsevier, 370 pp.

Walsh, J. E., and C. M. Johnson, 1979: Interannual atmospheric variability and associated fluctuations in Arctic sea ice extent. *J. Geophys. Res.*, 84, 6915–6928.

Warshaw, M., and R. R. Rapp, 1973: An experiment on the sensitivity of a global circulation model. *J. Appl. Meteor.*, 12, 43–49.

Washington, W. M., A. J. Semtner, Jr., C. L. Parkinson, and L. Morrison, 1976: On the development of a seasonal change sea ice model. *J. Phys. Oceanogr.*, 6, 679–685.

Washington, W. M., A. J. Semtner, Jr., G. A. Meehl, D. J. Knight, and T. A. Mayer, 1980: A general circulation experiment with a coupled atmosphere, ocean and sea ice model. *J. Phys. Oceanogr.*, 10 (in press).

Washington, W. M., and D. L. Williamson, 1977: A description of the NCAR global circulation models. *Methods in Computational Physics*, Vol. 17, *General Circulation Models of the Atmosphere*, J. Chang, Ed., Academic Press, 111–172.

Williams, J., R. G. Barry, and W. M. Washington, 1974: Simulation of the atmosphere using the NCAR global circulation model with Ice Age boundary conditions. *J. Appl. Meteor.*, 13, 305–317.

Wu, M. L., 1980: The exchange of infrared radiative energy in the troposphere. *J. Geophys. Res.*, 85, 4084–4090.

Zwally, H. J., and P. Gloersen, 1977: Passive microwave images of the polar regions and research applications. *Polar Record*, 18, 431–450.

CLOUD-RADIATION EXPERIMENTS CONDUCTED WITH GLAS GENERAL CIRCULATION MODELS

by

Gerald F. Herman

Department of Meteorology
University of Wisconsin, Madison, WI 53706
and
Laboratory for Atmospheric Sciences
NASA Goddard Space Flight Center, Greenbelt, MD 20771

ABSTRACT

The cloud and radiation budget climatologies of GLAS second order general circulation models are assessed for the January-February and July periods, and the models' radiation and cloud parameterizations are briefly reviewed. Systematic errors in the computed infrared radiation budget are attributed to difficulties in treating the infrared optical properties of clouds, and in predicting subgrid scale fractional cloudiness. The solar radiation balance is generally reasonable, although some discrepancies with observations occur during the Southern Hemisphere summer. Problems with the models' cloud climatology include excessive low cloudiness during the Northern Hemisphere winter, and a failure to simulate adequately the advance and retreat of the ITCZ.

Four cloud feedback experiments that were conducted with GLAS GCMs are reviewed. These include transparent cloud experiments, fixed and variable cloud experiments, and desert albedo feedback experiments. The role of radiation in the maintenance of the Siberian high also is investigated.

1. INTRODUCTION

The general circulation models (GCMs) of NASA's Goddard Laboratory for Atmospheric Science (GLAS) have been widely applied to problems of weather forecasting, and in climate sensitivity and simulation studies. A striking and sometimes disturbing conclusion that frequently emerges from the analyses of these GCM calculations is that the results are sensitive to a significant degree either to the parameterizations of solar or infrared radiation, or to the computational procedure through which the radiative fluxes interact with clouds, the gaseous atmosphere, or the surface of the earth. In most cases, the nature of the sensitivity is complicated, and frequently is ascribed to processes that are loosely termed cloud-radiative interactions or cloud-radiative feedback.

There are two broad problems involving the relationship between clouds and radiation that arise in the numerical modeling of weather and climate. There is always an interaction between clouds and radiation insofar as when a stream of radiation encounters cloud particles, there is either a redirection of energy from the incident stream (scattering), or an exchange of energy between the radiation field and the thermal energy of the cloud particles (absorption or emission). These interactions between clouds and radiation essentially determine the amount of radiative energy that is available to the earth-atmosphere system. Thus, the influence or effect of clouds on the radiation must be properly represented in numerical simulations of climate or the general circulation, and this is accomplished by specifying the optical properties of the atmosphere and of the earth's surface. The optical properties may themselves depend on the disposition of the radiation, as in the case of when radiative cooling induces cloud formation. The mutual adjustment of the cloud and radiation fields to a state that is consistent with the internal dynamics of a model is termed cloud-radiative feedback. A fundamental and essentially unanswered question has been whether the detailed simulation of cloud-radiative feedback is critical for climate and general circulation sensitivity studies. Likewise, neither the importance of cloud influences nor the effect of cloud-radiative feedback have been established for short- and medium-range forecasting efforts.

We summarize here the principal features of the cloud and radiation budget climatologies of GLAS GCMs. These fields are compared with observed climatologies to assess the reliability of model-generated fields, and to illustrate potential cloud influences on the radiative balance of the model. Also discussed are several GCM experiments conducted at GLAS in which the results clearly were dependent on the nature of the cloud interactions with the model radiation and dynamics. These latter discussions involving potentially complicated cloud feedbacks are at the same time qualitative, speculative, and perhaps model dependent. They also illustrate the inherent difficulty that exists in attempting to deduce the nature of cloud-radiative feedbacks based on the output generated by a global circulation model.

2. CLOUD PARAMETERIZATION AND RADIATIVE TRANSFER

Many details of the GLAS GCMs have been described by Somerville et al. (1974), Stone et al. (1977), and Halem et al. (1979). Here it suffices to note that the GLAS model is a nine-layer primitive equation model utilizing a σ-vertical coordinate formulation together with a 4° latitude by 5° longitude horizontal grid. Ocean surface temperatures and polar sea ice boundaries are prescribed to vary according to a pre-determined climatology, while ground temperatures over land and ice are calculated from the surface energy balance. Simple approximations are used for ground moisture conditions, and surface fluxes of heat and moisture are based on drag laws that account for the stability and windshear in the boundary layer, and the roughness of the surface.

Cloud formation processes in the model are fully coupled to cloud radiative processes insofar as clouds grow and dissipate in response to changes in temperature, stability, and surface heating, and these depend in part on the flux and flux divergence of solar and thermal radiation. The parameterization of these cloud and radiative processes are described below.

Convective cloud formation in the GLAS model (see Helfand, 1979) follows the Arakawa three level cumulus cloud parameterization. Convection occurs if air at a cloud base layer becomes buoyant during its moist adiabatic ascent to the cloud top layer.

Convective clouds (see Fig 1) are said to be penetrative when the lowest 6 model layers participate in the vertical mixing; while low-level convection involves σ-layers 7 and 8, and upper-level convection involves layers 5 and 6. Supersaturation clouds in the model, which represent stratiform clouds in nature, form simply when the water vapor mixing ratio at a grid point exceeds the saturation mixing ratio for the ambient temperature.

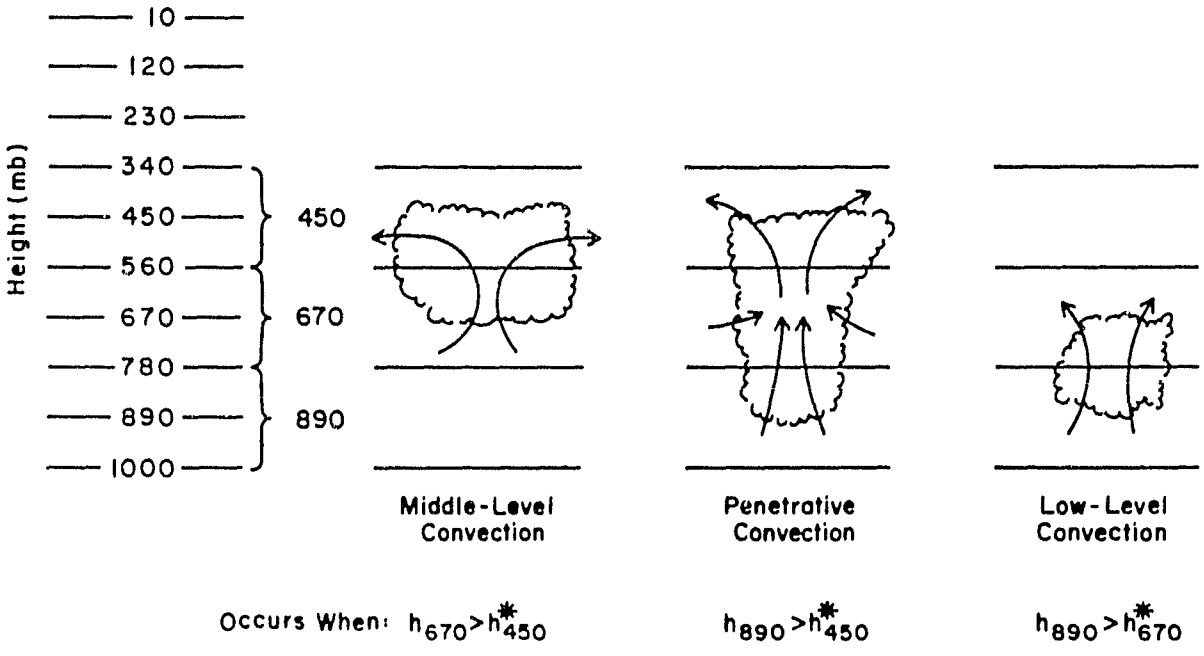

Figure 1. Convective cloud formation with the 3-layer "strapped" Arakawa scheme. (after Helfand, 1979).

Solar radiation in the GLAS model has been computed using the formulation of Lacis and Hansen (1974). Ozone absorption is treated with accurate empirical formulae based on detailed multiple scattering calculations and laboratory measurements of ozone absorption. Water vapor absorption under clear-sky conditions is computed with the Yamamoto (1962) data, and under cloudy conditions this absorption is reformulated with a "k-distribution" for use in conjunction with a two-stream approximation. In the published version of the Lacis

and Hansen parameterization neither absorption by the liquid water droplets nor the solar zenith angle dependency of clouds or of the surface is represented. Modifications to the GLAS solar radiation code have been made by Davies (1980) to include the effect of solar elevation on the surface albedo, and to introduce solar zenith angle angle dependency into the cloud multiple scattering calculations with a δ-Eddington two-stream approach. The preliminary results indicate that the effects of these modifications are substantial, e.g., when the new zenith angle dependency was introduced into test runs the planetary albedo of the model increased from 31 to 37%.

In the present version of the GLAS radiation code the optical properties of the cloud (i.e., optical depth and single scatter albedo) are prescribed quantities, since cloud liquid water is not a predicted model variable at the present time. Thus, cloud optical thickness depends only on cloud type, and the vertical layer in which the cloud forms. (see Table 1)

The calculation of solar radiation requires approximately 2 seconds of CPU time to compute the entire 46x72 array of vertical profiles at each time step. This represents approximately 10% of the time required for the total GCM calculation at time steps when the solar radiation routine is called. At present it is called every third time step, or every 30 minutes.

Table 1. Prescribed cloud properties in GLAS solar radiation calculations.

Cloud origin	Cloud type	Albedo (%)	Optical Thickness
Convective			
mid-level	Ac	50	8
low-level	Cu	70	16
penetrating	Cb	80	32
Supersaturation			
0-400 mb	Ci	20	2
400-700 mb	As	50	8
700-1000 mb	St	70	16

Infrared radiation in the GLAS GCM originally was computed according to an algorithm developed by J. Hogan and described in Somerville et al. (1974). In recent years the Hogan calculation was replaced by the more detailed code developed by Wu and Kaplan (see Wu, 1980). A significant price was paid for this increased accuracy: The running time of the Hogan version of the code was about 40 seconds. For the same calculations the Wu-Kaplan algorithm required 150-200 seconds per call to the longwave radiation.

The Wu calculation closely follows the formulation of Rodgers and and Walshaw (1966), although revised spectral data are used in the 6.3 μm water vapor band and in the continuum region. Ozone and carbon dioxide transmission are parameterized on the basis of precomputed line by line calculations. All clouds in the infrared calculation are assumed to be optically thick.

Significant differences in the GLAS model climatology occurred when the Hogan calculation was replaced with the Wu-Kaplan routine. (see Wu et al., 1978). In general the differences between cooling rates computed by the Wu-Kaplan and Hogan algorithms were small in the mid-troposphere, but cooling rates in the upper troposhere and lower stratosphere were larger with the Wu-Kaplan formulation because of its improved treatment of CO_2 absorption. Cooling rates were also larger in the lower troposhere at low latitudes because of the inclusion of water vapor dimer absorption.

3. RADIATION CLIMATOLOGY OF THE GLAS GCM.

In general, the realistic simulation of the radiation budget of the earth-atmosphere system may be viewed as a necessary, but not sufficient, condition for concluding that a model can accurately simulate the observed climate. If the GCM's radiation balance agrees with observations, it is one of several indications that the dynamical processes which determine the distribution of cloudiness, water vapor, and temperture are properly simulated. By itself, a correct radiation balance does not ensure that the simulated general circulation is correct or even reasonable.

The model's radiation balance that is discussed here may be viewed as a model climatology insofar as it is based on ensemble averages computed from a number of January-February and July simulations. The January-February simulations to which we refer were derived from the runs used in the ice margin experiments of Herman and Johnson (1978) and in the sea surface temperature anomaly experiments of Shukla and Bangaru (1975). These simulations were initialized with 00 GMT 1 January conditions, and averages were obtained from model data sampled at 12 hour intervals during the last 30 days of the 45 day simulations. Thus, the monthly averages refer to the mean defined over the time interval 1200 GMT 15 January to 1200 GMT 14 February. The July simulations were obtained from the climate variability and predictability studies conducted at GLAS by Dr. J. Shukla and collaborators. They were initialized with 00 GMT 15 June NMC conditions, or perturbations thereof, and averages were computed from data collected at 12 hour intervals between 1 July and 1 August. The model climatology was thus formed from the respective averages of the eight January-February simulations and seven July simulations. More details of the individual runs used in the climatology appear in Herman and Johnson (1980, Table 1). It is assumed that the GCM data that are sampled after fifteen days of integration are sufficiently independent of the initial conditions, and thus the fields are representative of the GCM's internal adjustment to the boundary conditions and external forcing.

The model's radiation climatology is compared in Figures 2 and 3 with the observed satellite-derived radiation climatology recently compiled by Winston et al. (1979) for the for the January-February and July periods.

The most striking feature of the model's infrared radiation budget at the top of the atmosphere is the large and systematic underestimation of the amount of radiation lost to space during both seasons. On the average this systematic bias is 30-40 Wm^{-2}, but becomes as large as 60-70 Wm^{-2} during the winter in the high latitudes of the Northern Hemisphere.

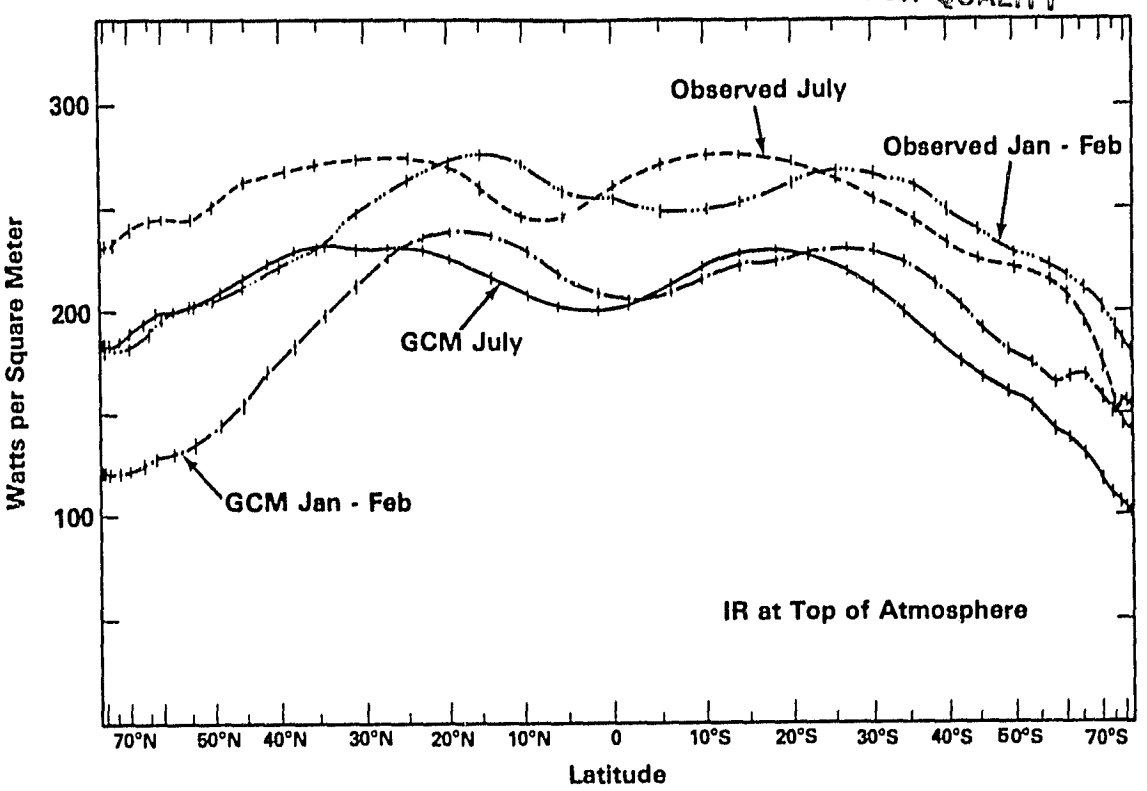

Figure 2. Observed and simulated net longwave radiation at the top of the atmosphere. Key: Simulated July _____ ; Observed July _ _ _ ; Simulated January-February____ . ___ _; Observed January-February ___. _ _ _ ___ _ _ _;

The reason that the model fails to emit enough thermal radiation to space is due to its difficulties in properly representing the infrared optical properties of model-generated clouds. Firstly, all clouds in the model are treated as being completely opaque (i.e., having unit emissivity) irrespective of their temperature. Thus the model does not distinguish between liquid water and ice clouds, and does not account for the semi-transparent properties of cirrus, or thin stratiform clouds. It is commonly accepted that these latter cloud types have emissivities that depart substantially from unity, and are thus capable of transmitting to space warmer radiation that is emitted from the surface or lower troposphere.

Secondly, all model clouds, including those that result from subgrid scale cumulus convection, are assumed to occupy the entire (~400x400km^2) grid area. Hence fractional cloudiness is not represented, and model clouds at each grid point trap more radiation than do the scattered and broken cloud fields that occur in nature.

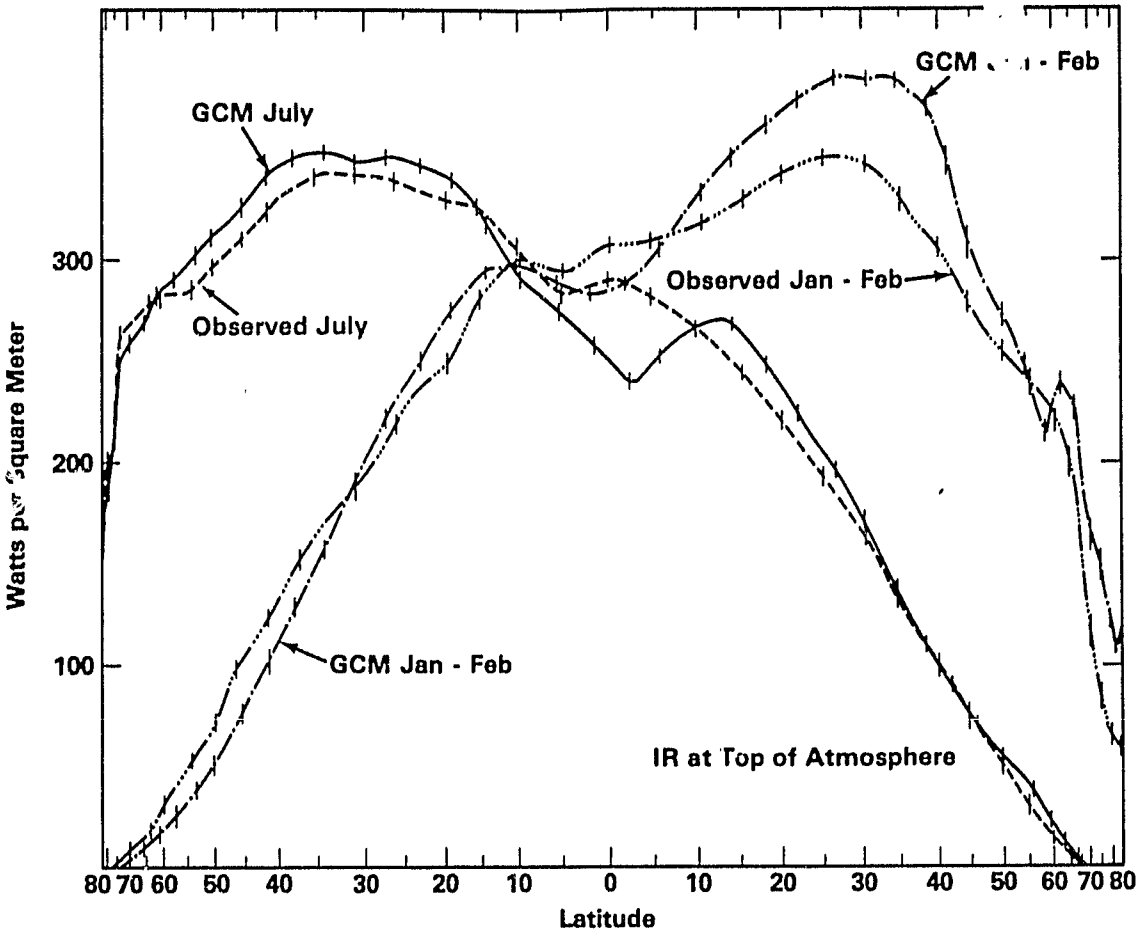

Figure 3. Observed and simulated solar radiation absorbed by the earth atmosphere system. Key is the same as in Fig 2.

Modifications to the Wu-Kaplan radiation scheme recently have been made to account for both fractional cloudiness and variable emissivity (see Herman and Krishnamurthy, 1981), although extended integrations have not yet been carried out. Vertical profiles of the flux and flux divergence calculated for different cloud fractions and emissivities are shown in Table 2. It is clear that specifying the proper cloud fraction and emissivity potentially provides the means for bringing the model longwave radiation balance into closer agreement with the observations. Clearly, the difficult theoretical problem here lies in parameterizing the fractional sub-grid distribution of cloudiness based on the internal dynamics and thermodynamics of the model.

Table 2. Longwave fluxes and cooding rates for various cloud fractions (f) and cloud transmissivity (T_c). Values are for clouds in sigma-layer 5, 46° N, for 1 February. (Details of calculation appear in Herman and Krishnamurthy, 1981.)

Level	Pressure (mb)	Flux(W m^{-2})				
		Cloudless f=0.0,$\bar{T}_c$=1.0	f=0.25,$\bar{T}_c$=0.0 or f=1.0,$\bar{T}_c$=0.75	f=0.5,$\bar{T}_c$=0.0 or f=1.0,$\bar{T}_c$=0.5	f=0.75,$\bar{T}_c$=0.0 or f_c=1.0,$\bar{T}_c$=0.25	f=1.0 $\bar{T}_c$=0.0
1	10	211	195	179	164	148
2	120	205	189	173	157	141
3	230	197	181	164	148	131
4	340	187	170	153	136	119
5	450	170	152	134	116	98
6	560	151	126	100	75	49
7	670	134	113	92	72	51
8	780	118	101	83	66	48
9	890	104	89	74	59	44
10	1000	90	77	64	51	39

Layer	Pressure at Center of Layer (mb)	Cooling Rate (°C/Day)				
		Cloudless f=0.0,$\bar{T}_c$=1.0	f=0.25,$\bar{T}_c$=0.0 or f=1.0,$\bar{T}_c$=0.75	f=0.5,$\bar{T}_c$=0.0 or f=1.0,$\bar{T}_c$=0.5	f=0.75,$\bar{T}_c$=0.0 or f=1.0,$\bar{T}_c$=0.25	f=1.0 $\bar{T}_c$=0.0
1	65	0.4	0.5	0.5	0.5	0.6
2	175	0.6	0.6	0.7	0.7	0.7
3	285	0.8	0.9	0.9	0.9	0.9
4	395	1.3	1.4	1.4	1.5	1.6
5	505	1.4	2.0	2.6	3.2	3.8
6	615	1.3	1.0	0.6	0.2	-0.2
7	725	1.2	1.0	0.7	0.5	0.2
8	835	1.1	0.9	0.7	0.5	0.3
9	945	1.1	0.9	0.8	0.6	0.4

In general the solar radiation absorbed by the model's earth-atmosphere system agrees well with the observations, except in the mid-latitudes of the Southern Hemisphere during July and in the equatorial regions during January. It is plausible that this excess absorption in the Southern Hemisphere is a consequence of the relatively small values of cloudiness (and lower planetary albedo) simulated during January between 10° and 40°S. However, the cloudiness is also underestimated during the Northern Hemisphere summer, but the differences between the observations and the simulations are not as large as in winter.

4. CLOUD CLIMATOLOGY OF THE MODEL.

The cloud climatology of the GLAS GCM was obtained from the eight January-February and seven July simulations described in Section 3. As a measure of cloudiness in the model we use cloud frequency, which is defined as the fraction of the total integration time during which a specified cloud type occurred at a grid point.

The zonally-averaged model cloud frequency is illustrated in Figure 4a and 4b. For comparison we also illustrate the zonal values for January and July tabulated by Berlyand and Strokina (1975), and also values interpolated from the zonal summary presented by Gates and Schlesinger, (1977). Of course, only a qualitative comparison is possible because of the disparity between the definitions of "cloudness" used in the different sources. The Beryland and Strokina and Gates and Schlesinger data are mixtures of surface and satellite observations, and are supplemented by inferences from other analyses. The precise relationship between the measures of cloudiness reported in these analyses and the cloud frequency in the GCM is yet unclear. The gross features of the global climatology are simulated by the model: Maximum cloudiness occurs in mid-and high latitude, and in the equatorial tropics, with minimum cloudiness in the subtropical regions.

The southward shift of the tropical maximum from July to January corresponding to the southward migration of the ITCZ is apparent in the Berlyand and Strokina data, and is simulated by the GCM. However, the amplitude of the simulated shift is extremely small as compared with observations. In the high latitudes of the northern

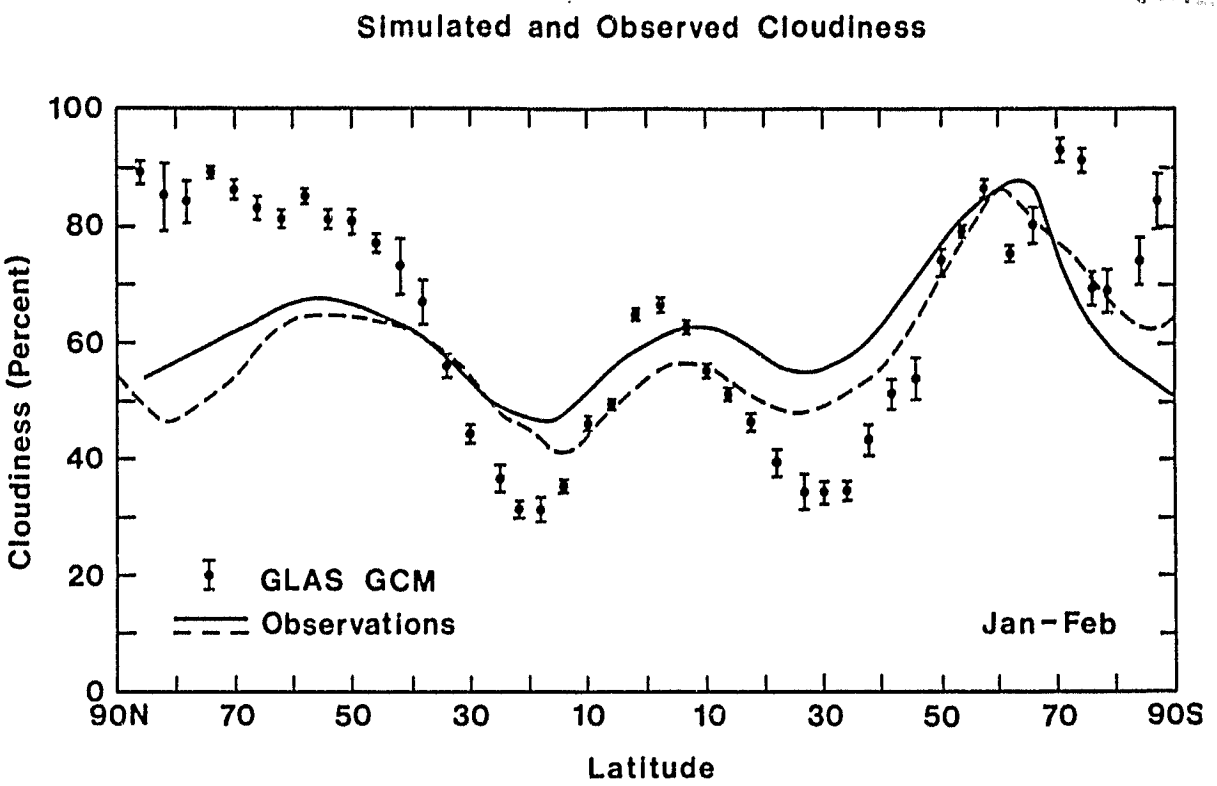

Figure 4a. Observed zonal cloudiness from Berlyand and Strokina (solid line) and as compiled by Gates and Schlesinger (1977). Bars indicate the inherent variability of model-generated cloudiness.

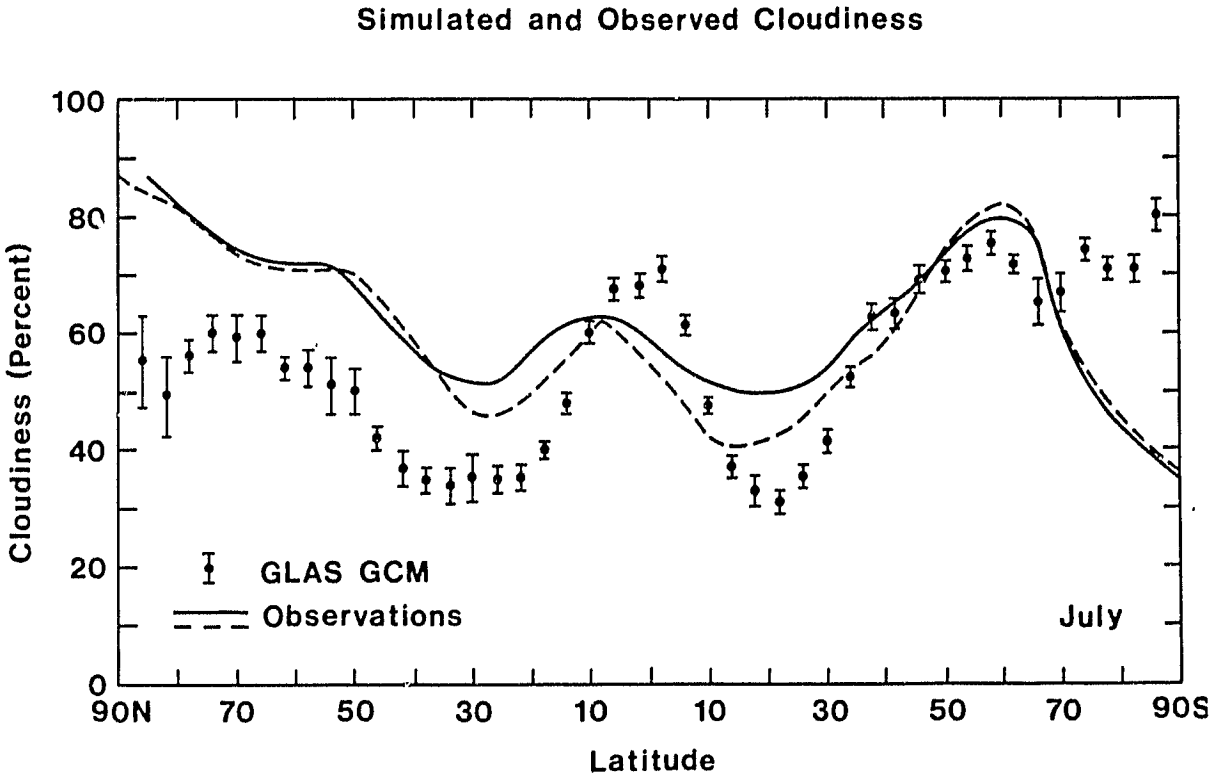

Figure 4b. As in Figure 4a, except for July.

hemisphere (north of 60°N) the observations show that maximum cloud cover occurs during the summer, due primarily to the buildup of stratus over the Arctic Basin and convective cloudiness over the adjacent continents. The cloudiness diminishes in winter owing to the development of the relatively cloudfree continental anticyclones. This trend is reversed in the GCM due to the wintertime buildup of stratiform clouds throughout the high mid-latitudes of the northern hemisphere. Elsewhere a detailed comparison is difficult to obtain.

The observed global distribution of cloudiness obtained by Berlyand and Strokina (1980) is shown in Figures 5a and 5b. During January, maximum cloudiness is observed to occur over the cyclonically-active regions of the north Atlantic, north Pacific, and sub-Antarctic oceans; over equatorial Brazil, Africa, and Indonesia; and over the Barents Sea and northwestern Europe. Minima are found over the continental deserts of Asia, Africa, Australia, and North and South America; over eastern Siberia, and over the sub-tropical oceans. During July (Figure 5b) the cloud maxima persist over the Atlantic, Pacific, and southern oceans, and there is a slight northward shift of the cloud maxima in the equatorial tropics. The summertime maximum of stratus clouds in the Arctic is clearly evident. The extent of the regions of minimum cloud cover over the deserts has also expanded relative to the January situation.

The GLAS GCM global cloud climatology is shown in Figures 6a and 6b. Here the digital value represents the range of cloud frequency in tenths, e.g., an integer 3 indicates that the cloud frequency lies in the range 30-39%. For emphasis, regions where the convective cloudiness exceeds 30% are enclosed by a solid line, and similarly for regions where the frequency of supersaturation or total cloudiness exceeds 70%.

From figures 6a and 6b it is evident that the GCM reproduces the convective maxima over Brazil, Africa, and Indonesia, and the northward migration of this maxima from January to July. The cyclonically-active regions of the north Atlantic and north Pacific show some slight convective activity, as do the southern oceans. The eastern regions of the subtropical oceans are essentially devoid of convective activity.

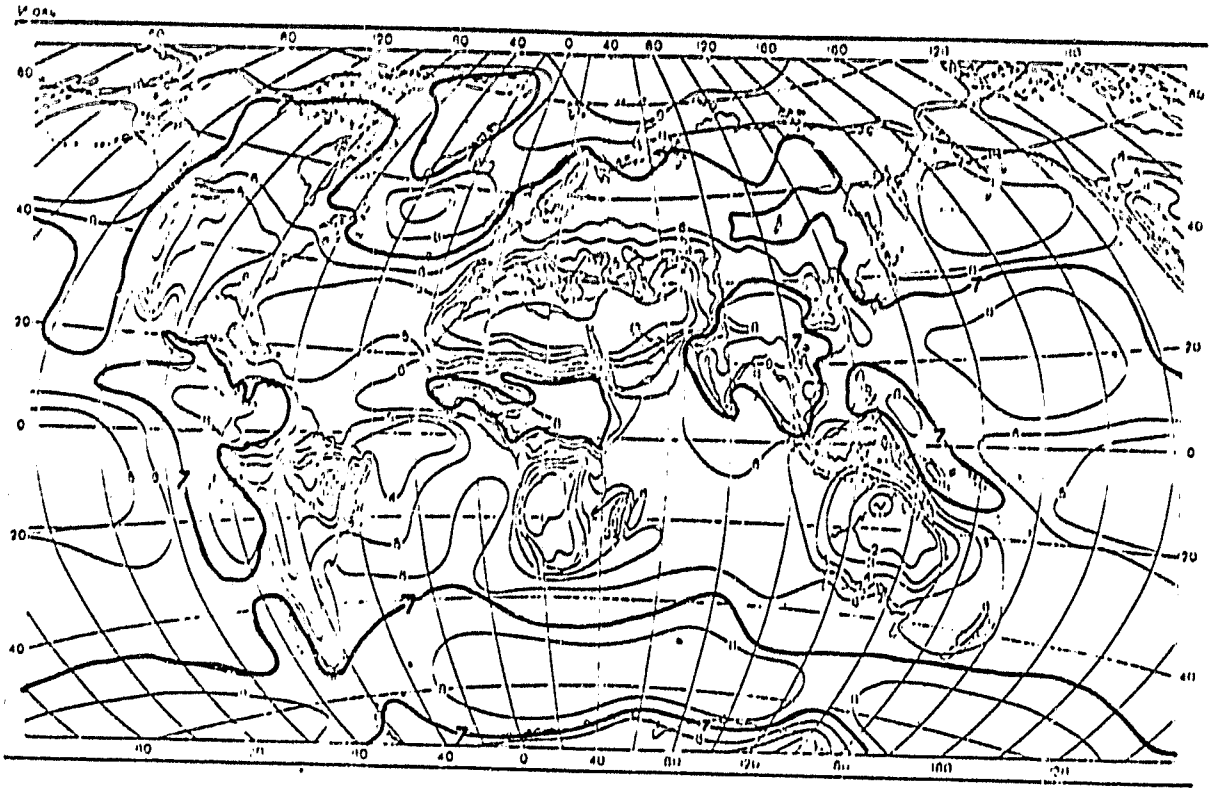

Figure 5a. Observed distribution of cloudiness (January). (After Berlyand and Strokina, 1980).

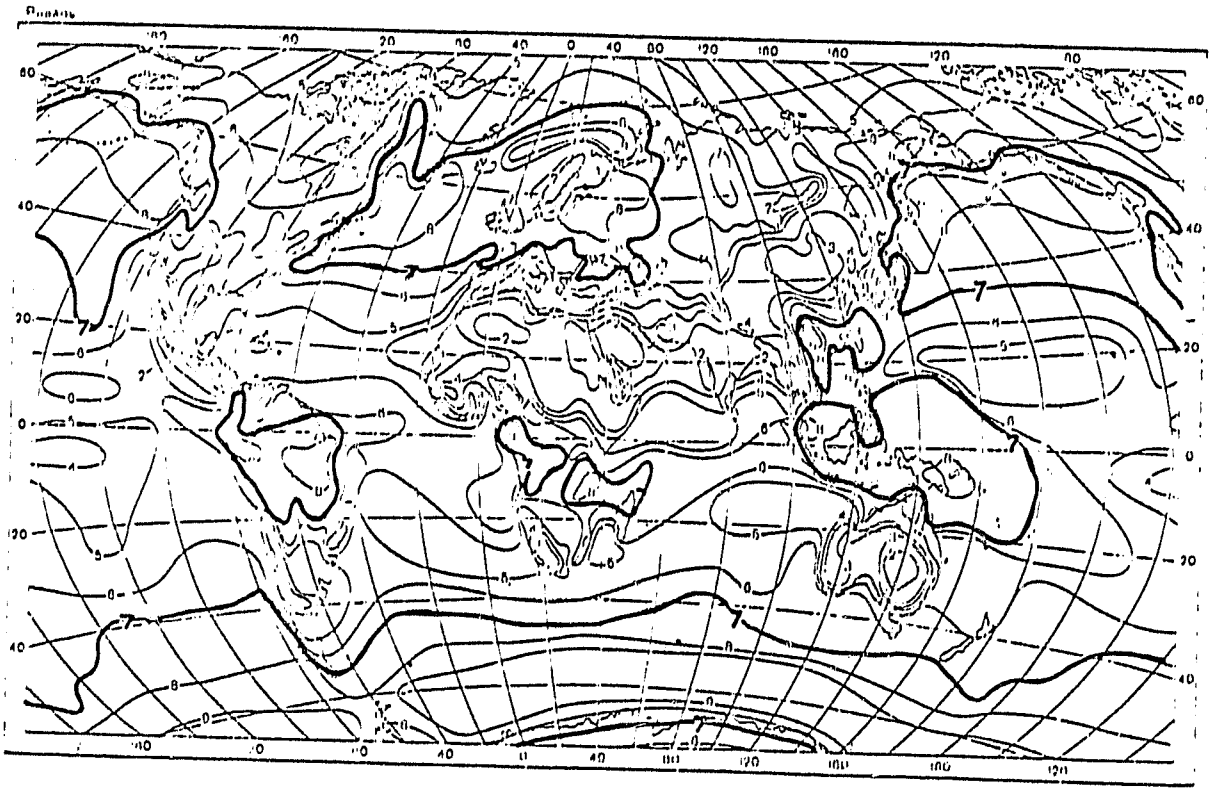

Figure 5b. Observed distribution of cloudiness (July). (After Berlyand and Strokina, 1980).

SUPERSATURATION

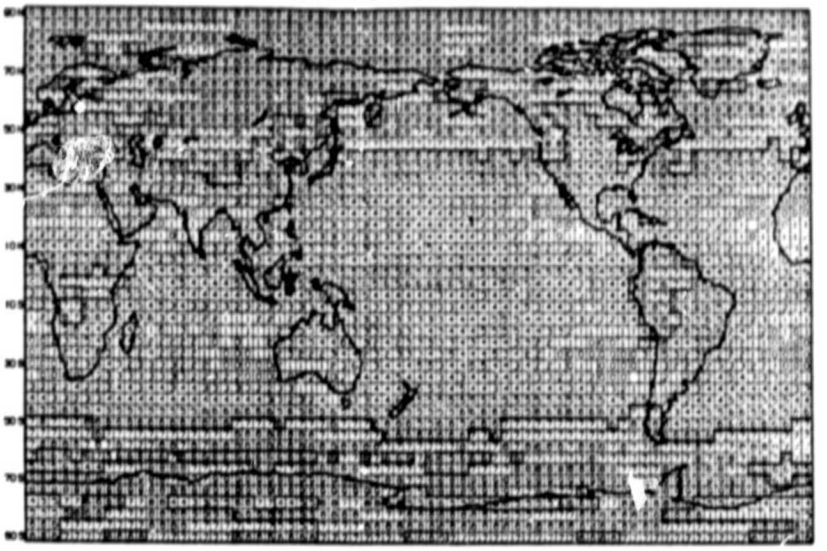

CONVECTIVE

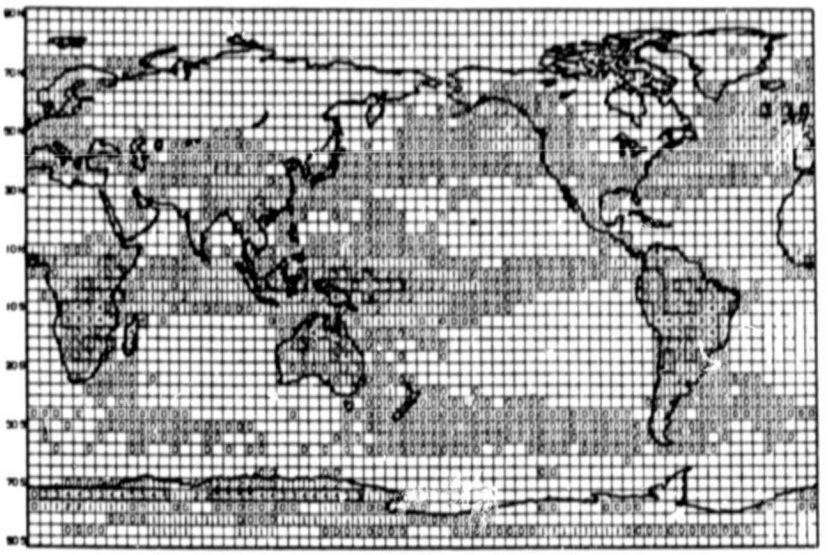

TOTAL

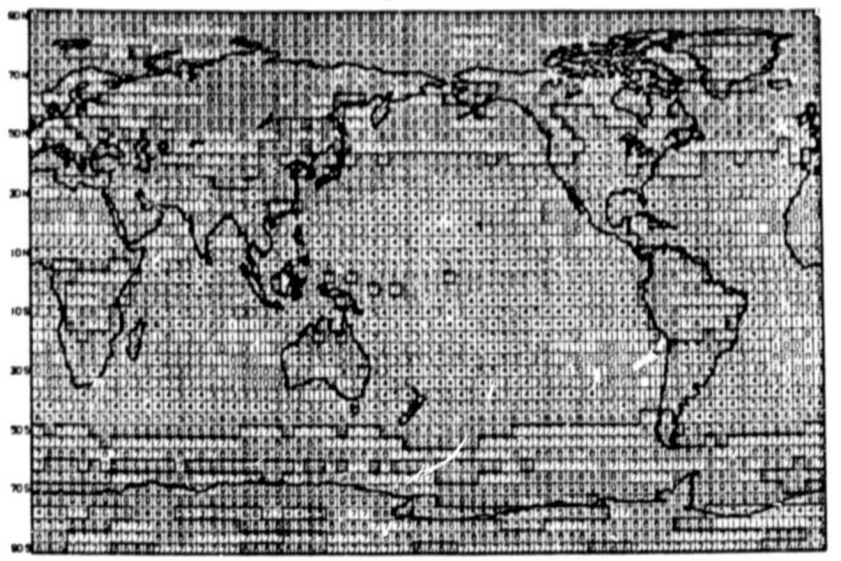

Figure 6a. Digitized cloud frequencies for January.

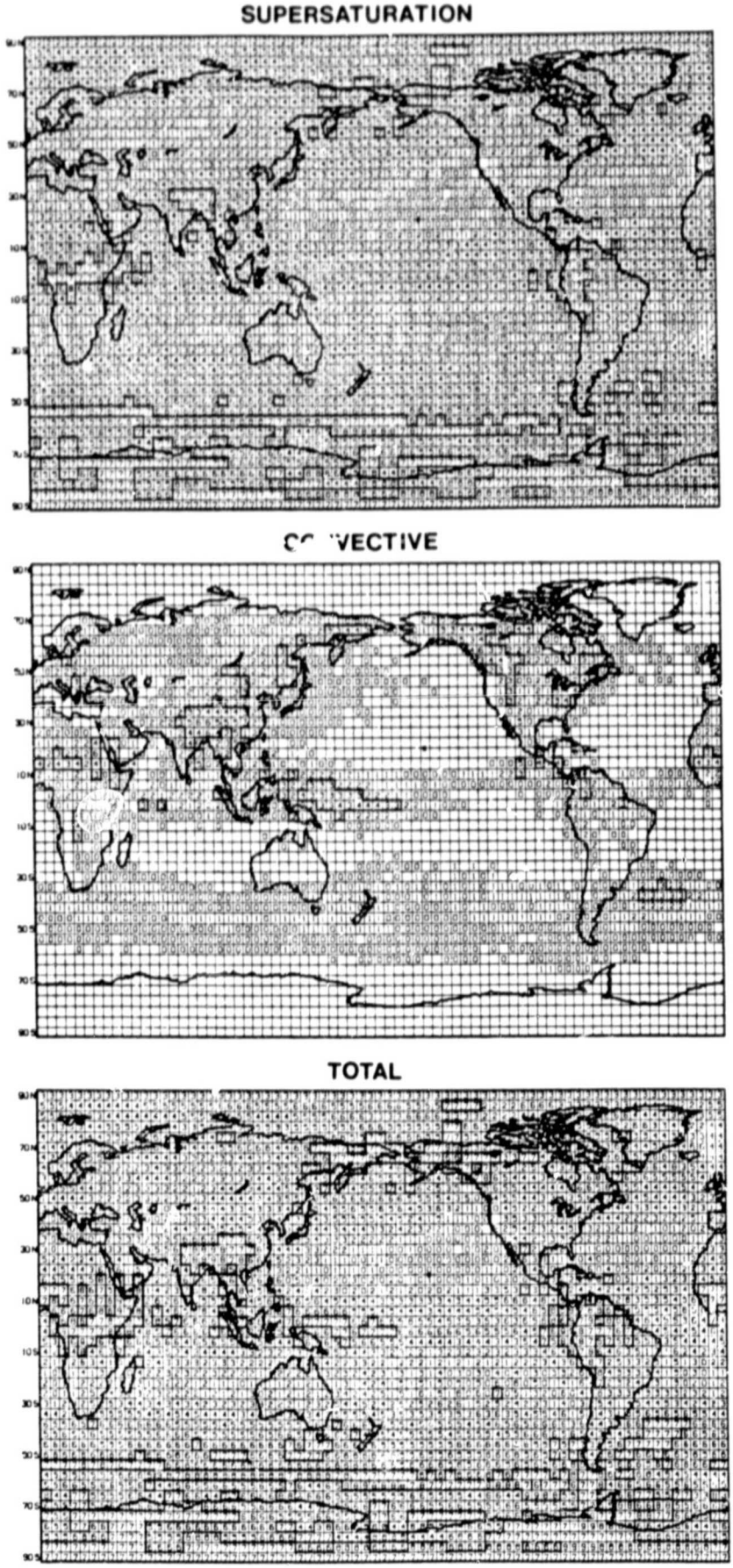

Figure 6b. Same as figure 6a, except for July.

The supersaturation or stratiform cloud cover of the model is also illustrated. The simulated maxima and minima during January generally agree with the observations except for the following cases: Extensive supersaturation cloud covers Antarctica, Greenland, the central Arctic basin, and northwestern Siberia. The tropical maxima and minima seem to be well represented. During July the model fails to produce the summertime stratus cover of the central Arctic, and the desert regions of Africa and North America appear to have too much cloud cover.

5. CLOUD-RADIATION FEEDBACK IN GLAS GCM EXPERIMENTS.

5.1. Albedo change in semi-arid regions.

One of the first cloud feedback experiments conducted with the model resulted from the desert-albedo experiments of Charney et al., (1977) that employed early versions of the GLAS (then GISS) model. Charney's (1975) original hypothesis for the expansion of deserts involved a positive feedback between large-scale subsidence and the surface albedo, and was independent of cloud formation processes. Stated briefly, it was proposed that increasing the surface reflectivity (through agricultural processes) would decrease the net radiation available to the surface, and would thus enhance large-scale subsidence through the response of a thermally-driven, frictionally-controlled circulation. The subsidence, in turn, would inhibit precipitation and the growth of vegetation, and thus further increase the albedo. This process might be illustrated by the following simplified feedback loop:

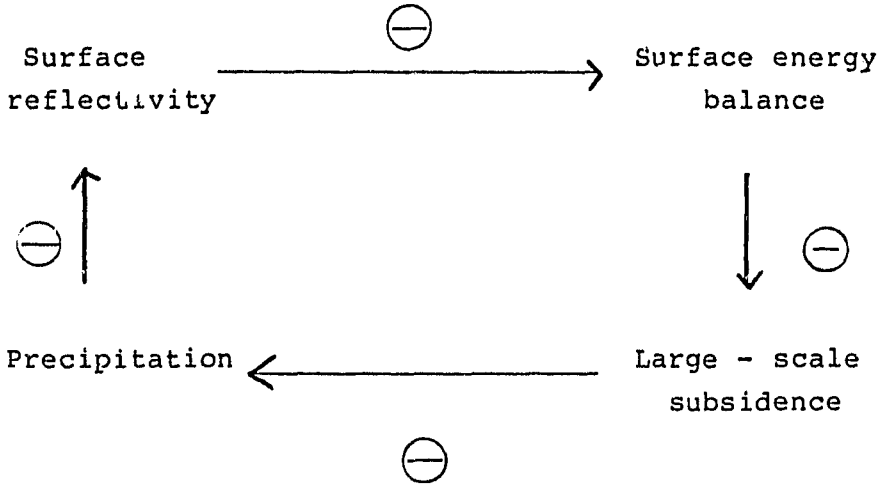

Here a minus (or plus) sign expresses in a schematic way the sense of the correlation between two processes. The feedback of the entire loop would be determined by the product of the signs of the individual links. Thus, the feedback loop shown above would be positive.

The Charney hypothesis was indeed verified in two sets of sensitivity experiments that were conducted with the GLAS GCM. When the albedo in these simulations was increased from 14 to 35% the net radiation at the ground diminished in all of the regions tested, and there was a resultant decrease in precipitation in two of the three regions. However, the cloud formation was handled differently in each of the two sets of experiments, and thus the mechanisms through precipitation was diminished were also different.

The differences between the two experiments are summarized in Table 3. One experiment is refered to as having no cloud feedback since surface evaporation was artifically suppressed and cloudiness differed by only 1-5% between the control and anomaly runs (see Row B). The other experiments were said to have cloud feedback because of the excessive evaporation provided by the parameterizations, and cloud frequency changes ranged between 15-24%.

When no cloud feedback was permitted, the radiation balance decreased by about 46 Wm^{-2}, and so did precipitation in most regions, in agreement with the Charney hypothesis. The differences, however, were due almost exclusively to the differences in the absorbed solar radiation caused by the albedo changes. With cloud feedback, the radiation balance also decreased in response to the brighter albedo, but the decrease was not generally due to diminished solar absorption. Rather, it was due to the fact that the infrared balance at the surface became smaller (more negative) due to the suppression of cloud formation. In fact, in two cases (see Row A) the solar radiation at the surface increased slightly because the planetary albedo diminished with the smaller cloud frequencies. Here, too, the precipitation also diminished.

These results illustrate the complicated way in which the cloud effect on the net radiation is linked to the surface brightness.

Table 3. Summary of Changes in Desert Albedo Experiments

	Control (low albedo)				Differences (high albedo minus control)			
A. Radiation Budget (Wm^{-2})								
	Feedback		No Feedback		Feedback		No Feedback	
	Solar	IR	Solar	IR	Solar	IR	Solar	IR
1. SHL	172	-59	263	-141	8	-26	-47	0
2. RPT	183	-48	273	-136	9	-28	-51	5
3. GP	189	-63	308	-176	-1	-18	-59	13
B. Cloud frequency (%)								
	Feedback		No Feedback		Feedback		No Feedback	
1. SHL	70		40		24		5	
2. RPT	77		43		20		1	
3. GP	67		21		15		1	
C. Hydrologic Cycle (Wm^{-2})								
	Feedback		No Feedback		Feedback		No Feedback	
	Evap	Precip	Evap	Precip	Evap	Precip	Evap	Precip
1. SHL	107	215	4	116	-26	-99	6	-38
2. RPT	119	142	3	61	-15	-75	5	9
3. GP	122	107	0	23	-29	-43	3	-11

D. Cloud Effects on the Radiation Balance (Wm^{-2})

	Low Albedo			High Albedo		
	IR	Solar	Net	IR	Solar	Net
1. SHL	82	-91	-9	56	-36	+20
2. RPT	88	-90	-2	55	-30	+25
3. GP	110	-119	-9	82	-61	+21

Regions: SHL-Sahel; RPT-Rajputana; GP-Western Great Plains

Row D of Table 3 shows the effects of cloud feedback. These are the IR balance without feedback minus that with feedback, and the solar balance minus that without feedback, for each of the two surface albedo conditions. Thus in the Sahel, for example, when the albedo was 14%, and the inclusion of feedback increased cloud frequency from 40 to 70%, the infrared balance increased by 82 Wm^{-2}, while solar absorption decreased by 91 Wm^{-2}, resulting in a net decrease of 9 Wm^{-2}. However, over the bright 35% albedo surface, the solar absorption was diminished by only 36 Wm^{-2}, because of the smaller differences between cloud and surface albedo. The net cloud effect was thus an increase of 20 Wm^{-2}, since the gain in the infrared was 56 Wm^{-2}. The surface albedo changes evidently accompany a change of sign in the net cloud effect.

b. Transparent cloud experiments

i. Radiation of balance studies.

A set of experiments was conducted with the GCM to examine further the separate roles that the visible and infrared opacity of clouds plays in determining the radiation balance at the top of the atmosphere. The details of these experiments are described in Herman et al. (1980).

Clouds are frequently said to exhibit an albedo effect when their formation causes the radiation balance to decrease because of their reflection of solar radiation, and a greenhouse effect when the balance is increased by their absorption and re-emission of infrared radiation. The relative roles of the greenhouse and albedo effects were examined in experiments in which the clouds were made transparent to the streams of solar and infared radiation while all other cloud processes such as formation, latent heat release, precipitation and vertical mixing were realistically computed. The differences between the control and the transparent simulations were then interpreted in terms of greenhouse and albedo effects.

The control and perturbation runs were 30 day integrations spanning the period 1-30 January, and were based on 00 GMT 1 January 1975 initial conditions from NMC. Ocean surface temperatures, surface albedo, and polar sea ice boundaries were prescribed, but were allowed to vary climatologically during the simulation.

The globally and hemispherically-averaged results are cited in Herman et al. (1980). In Figures 7 through 9 we illustrate the zonally-averaged values of the net longwave radiation at the top of the atmosphere, the solar radiation absorbed by the earth-atmosphere system, and the net radiation for the control and for the transparent simulations. The role of model-generated cloudiness in limiting the loss of infrared radiation is apparent from the curves for the control and the thermally transparent case: Without a greenhouse effect the radiation balance would become more negative at all latitudes, with the largest differences occurring in the tropics and in the warmer summer hemisphere. On a hemispheric basis, when clouds do not interact with thermal radiation, the radiation lost to space in the Northern Hemisphere, Southern Hemisphere, and globally increases on the average by 29, 40, and 34 Wm^{-2}, respectively.

The extent to which clouds increase the planetary albedo and thus decrease the solar radiation available is seen by comparing the curves in Fig. 8 for the solar radiation absorbed by the earth-atmosphere system for the control, with that for the solar transparent case. It is clear that clouds decrease the solar radiation budget at all latitudes, with the differences again being largest in the tropics and in the summer hemisphere. When clouds become transparent to solar radiation, the amount of solar radiation absorbed by the earth-atmosphere system increase on the average in the Northern and Southern Hemispheres, and globally by 34, 97, and 65 Wm^{-2}, respectively.

The net cloud effect on the net radiation balance is the combined effect of the greenhouse and albedo mechanisms. Under limited conditiohs it is possible to compute the net effect of the clouds on the radiation balance simply by adding the radiation loss due to the albedo effect and the gain due to the greenhouse effect. This would be possible only if the changes caused by the two processes were indepedent, i.e., only if the role of thermal radiation in cloud formation processes were unrelated to cloud-solar radiative interactions. The two fields of radiation may be coupled in a variety of ways. For example, warming of the ocean mixed layer through the absorption of solar radiation could induce deep cumulus convection, and thus decrease the longwave loss at the top of the atmosphere.

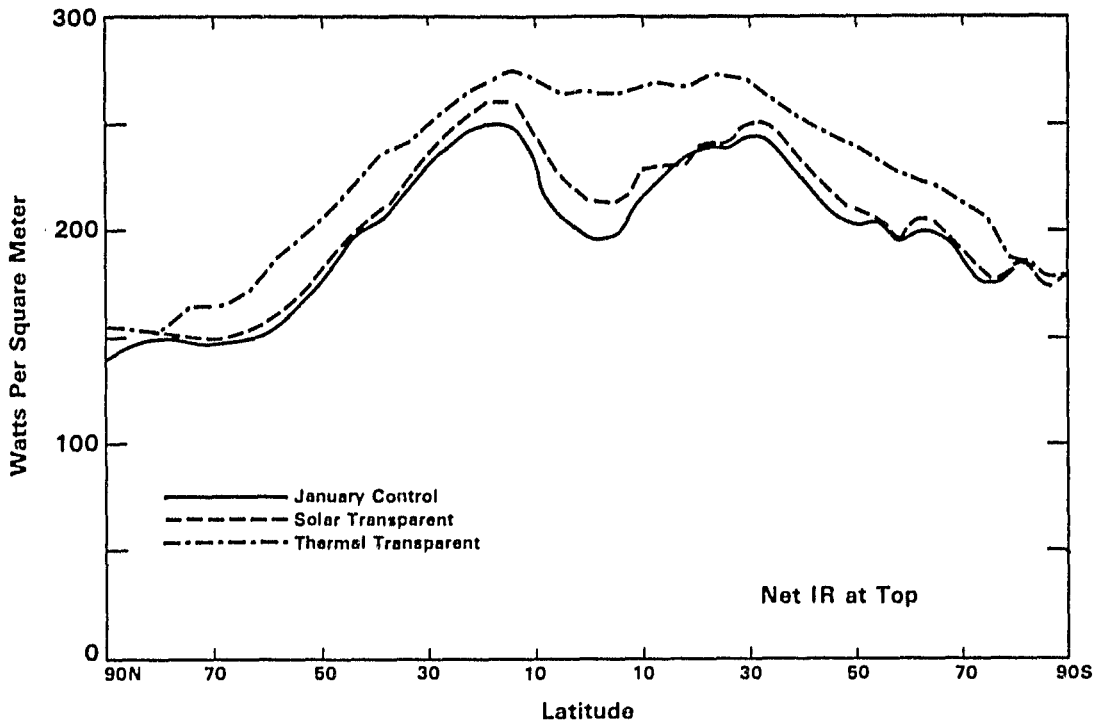

Figure 7. Zonally-averaged longwave radiation at top of atmosphere for control and transparent cloud simulations.

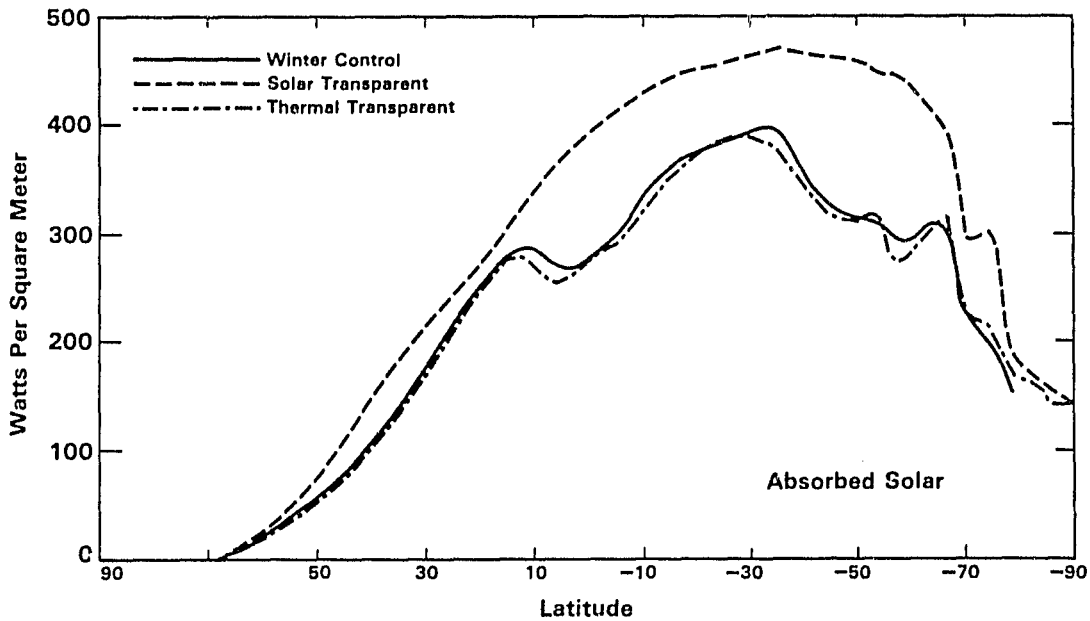

Figure 8. Zonally-averaged shortwave radiation absorbed by earth-atmosphere system for control and transparent cloud simulation.

The zonal distribution of the net cloud effect, ΔN, is shown in Fig 9. In the Northern (winter) Hemisphere the cloud effect is positive, or slightly negative, indicating that the greenhouse effect of clouds dominates their albedo effect, and clouds tend to increase the radiation balance by longwave emission more than they decrease it by reflecting solar radiation to space. In the Southern (summer) Hemisphere the net cloud effect is strongly dominated by the albedo effect. The areally-averaged values are +9 Wm^{-2}, -42 Wm^{-2}, and -16 Wm^{-2} for the Northern Hemisphere, Southern Hemisphere, and globe, respectively.

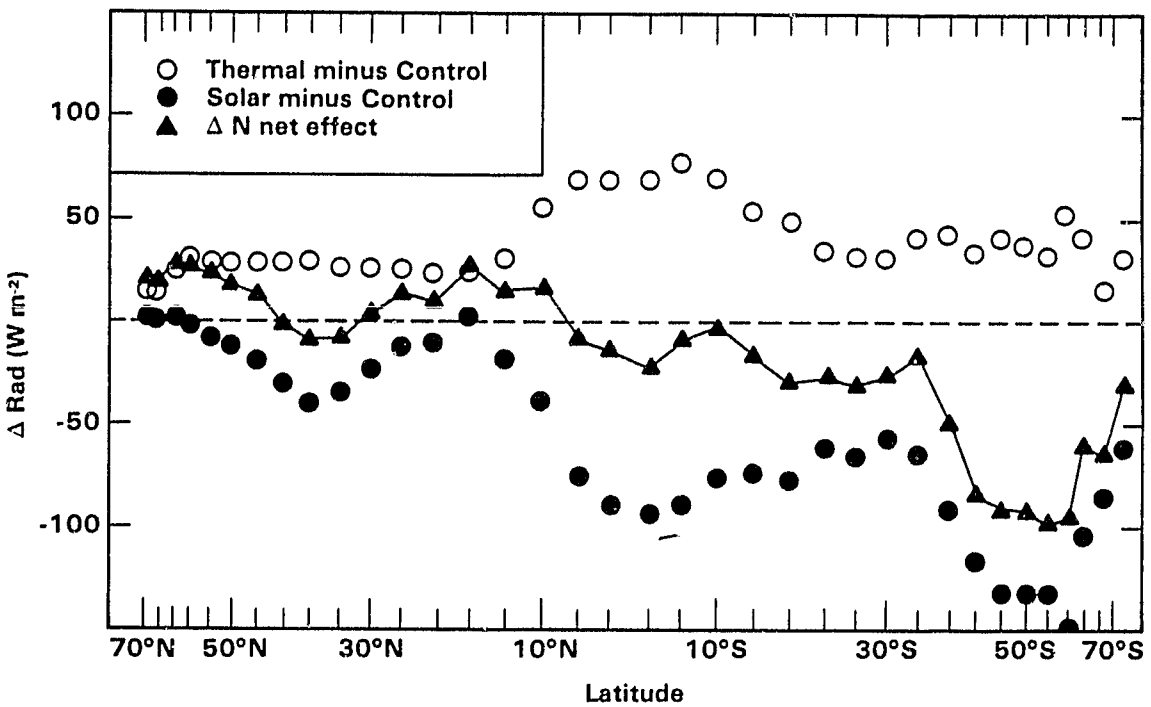

Figure 9. Cloud effect on the net radiation. Open circles are differences between control and clouds which are transparent to thermal radiation; closed circles are differences between control and clouds transparent to solar radiation. Triangles indicate net cloud effect on the net radiation.

Ellis (1978) recently deduced the net cloud effect by computing global radiation budgets from satellite data obtained under clear and cloudy conditions. For the same regions listed above Ellis obtained a net cloud effect of -12 Wm^{-2}, -42 Wm^{-2}, and -27 Wm^{-2} for the January-February period. These results agree well with the GCM values in the Southern Hemisphere, but conflict with the model results by showing a dominant albedo effect in the Northern Hemisphere. This discrepancy may be another consequence of the

previously discussed problem of unrealistic thermally opaque clouds in the GLAS model.

ii. Cloud-feedback studies

Although the cloud opacity was effectively set to zero in the transparent cloud simulations, clouds were still allowed to exist, and partake in all of the other dynamical functions that the GCM provides. It is thus possible to draw some conclusions about the means through which aspects of the model's dynamics are coupled to solar and infrared radiative processes in clouds. In particular, it is possible to investigate how cloud radiative processes interact or feedback on cloud formation processes.

Sea surface temperatures in the GCM are prescribed, and consequently the formation of convective clouds and supersaturation clouds over water in the GLAS GCM depends only on the response of the atmosphere to the changing radiative conditions. The increase (or decrease) of atmospheric temperature relative to the ocean surface due to radiative processes thus suppresses evaporation and sensible heat transfer at the surface and lowers (or raises) the relative humidity at other levels. Similarly, the heating (or cooling) of the water vapor in the lower troposphere would decrease (or increase) vertical stability. A possible feedback loop would be:

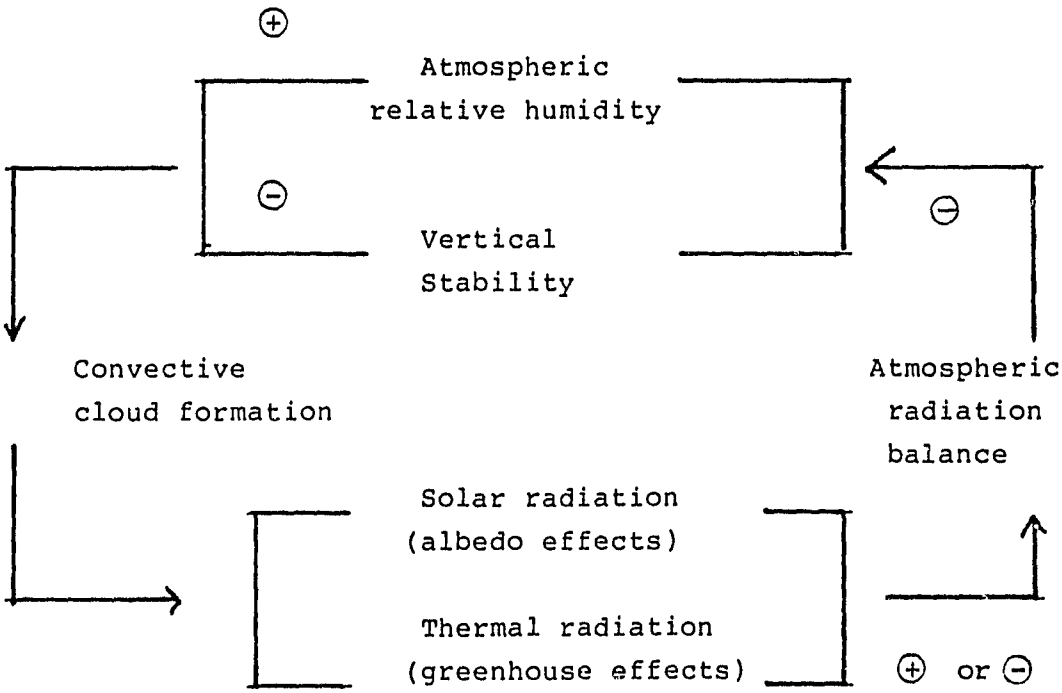

As drawn, the sign of the feedback loop depends on the relative roles of the albedo and greenhouse effects. If the albedo effect dominates,then the loop is positive, and decreasing the radiation balance becomes favorable for further cloud development. The changes in cloud frequency for convective and supersaturation clouds are shown in Figures 10 and 11. The increase in cloud frequency due to albedo effects clearly dominates the decrease due to greenhouse effects for supersaturation clouds. The differences are harder to discern for convective clouds.

Convective clouds over land tend to increase (or decrease) as the net radiation at the surface increases (or decreases) because of the strong dependency of the evaporation and sensible heat exchange on the net radiation at the surface. These clouds in a sense participate in a negative feedback loop since their occurrence causes the surface energy balance to change in a direction that is unfavorable for their further development or maintenance. This interaction can be summarized by the following feedback loop.

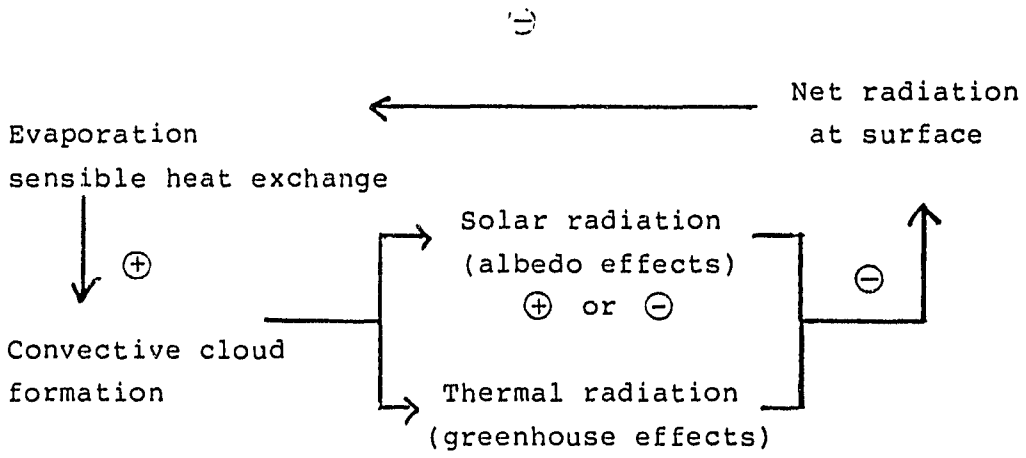

As drawn, the sense of the complete feedback loop again depends on the relative influence of the albedo and greenhouse effects on the surface radiation balance. Here we have assumed that the albedo effect dominates. This behavior is illustrated in Fig. 12, although there is much scatter to the data.

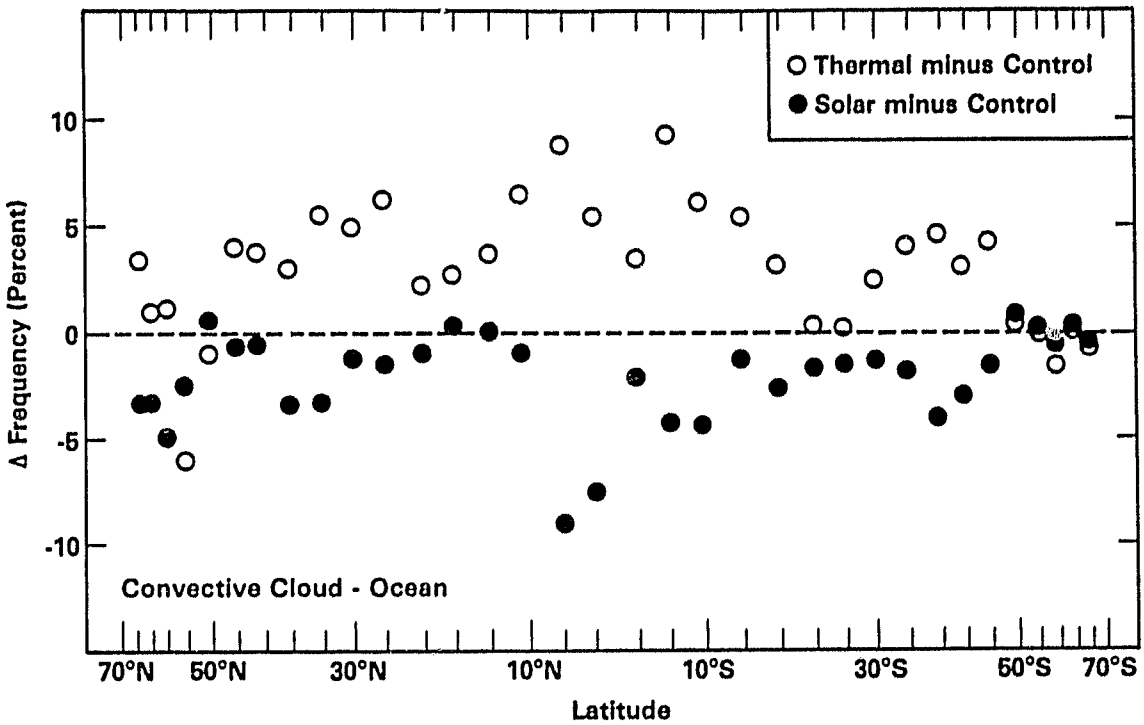

Figure 10. Differences in convective cloud frequency over water for control and transparent simulation.

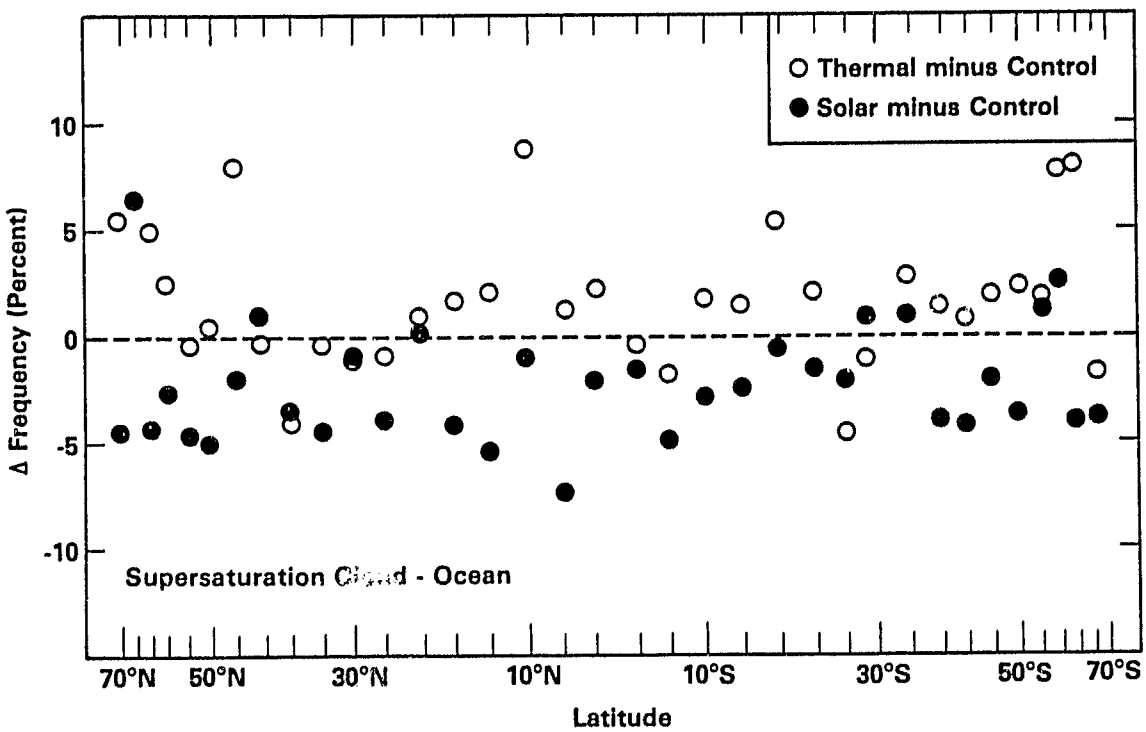

Figure 11. Same as Figure 10, except for supersaturation cloud.

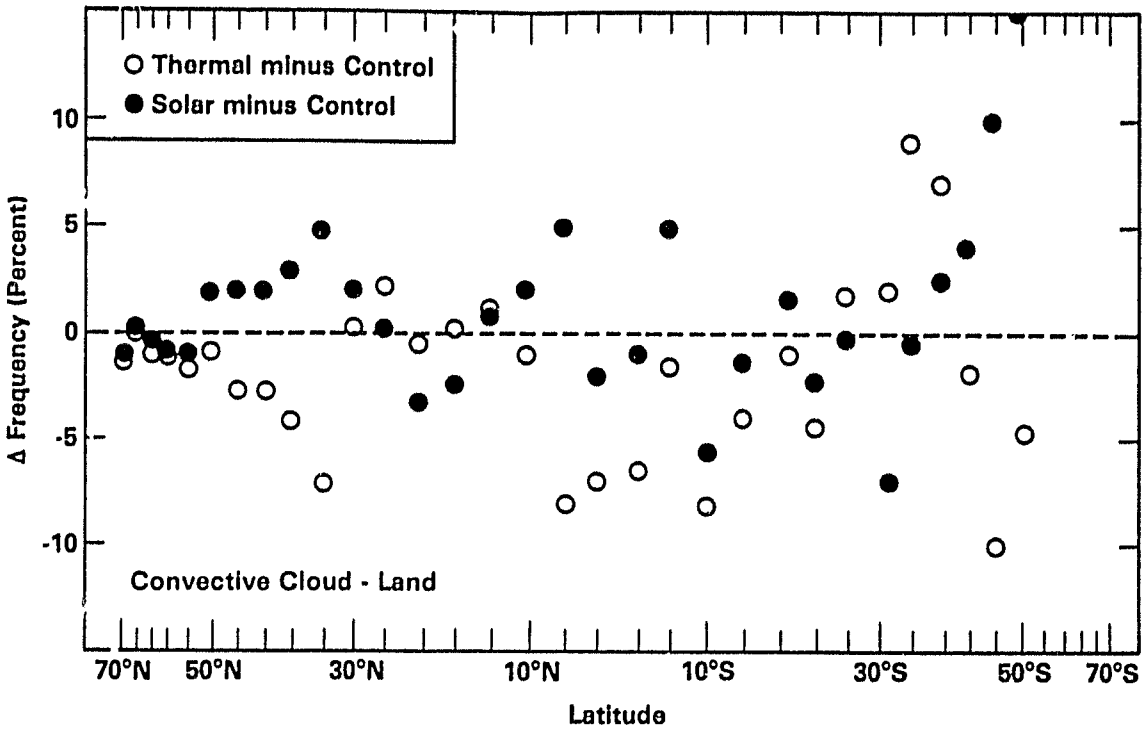

Figure 12. Same as Figure 10, except over land.

c. Fixed clouds vs. variable clouds.

It has sometimes been suggested (e.g., Hunt, 1978) that the general circulation may be adequately modelled with cloud fields that are specified according to a predetermined climatology, and which do not change or adjust their distribution to be consistent with other aspects of the model's dynamics. Some of the consequences of constraining the global cloud distribution to remain invariant were were demonstrated in GCM experiments (see Shukla and Sud, 1980) conducted with variable cloud fields produced by the GCM, and compared with those based on stationary, pre-computed cloud fields. The largest differences in cloud distribution generally occured in the tropical and subtropical regions, where fixed loci of convective clouds replaced the nearly-randomly occurring convective clouds of the GCM. One major consequence of the fixed cloud distribution was that stationary sources and sinks of radiative energy were introduced in low latitudes, replacing the smoother distribution that resulted from the variable occurrence of clouds. These differences were largest in the tropical western Pacific, and in

the peripheral Antarctic oceans, where the monthly-averaged fixed cloud frequencies were 10-20% greater than in the control. Relatively large differences were obtained between the low-latitude hydrologic cycle of the two runs. The zonally-averaged evaporation in the variable cloud control was significantly greater than in the fixed cloud run. (see Figure 13)

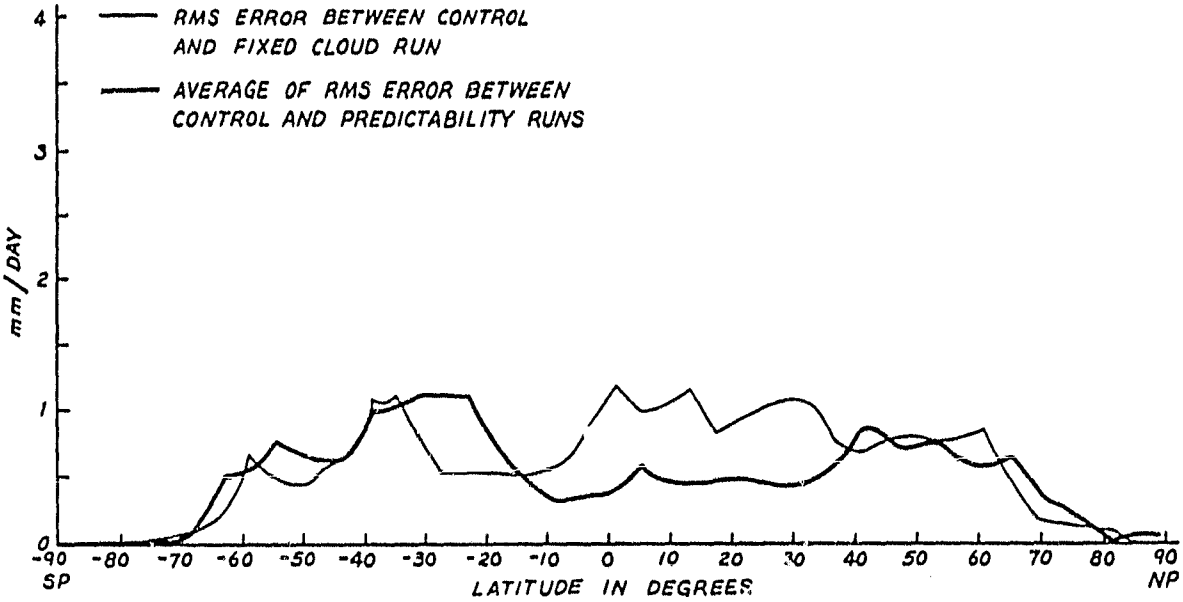

Figure 13. Difference in evaporation rate between fixed and variable cloud experiments, and differences in evaporation caused by random perturbations of initial conditions.

This result is easy to understand in view of the discussion in Section 5b. Since cloudiness over the oceans was greater in the fixed cloud run, low level atmospheric temperatures increased through greenhouse-type mechanisms, and evaporation was suppressed since the prescribed ocean surface temperatures could not respond to the changing cloud conditions. In mid-and high latitudes the differences were insignificant as compared with the inherent variability of the model.

It has thus far proved difficult to isolate the differences between specific meterological features in the fixed and variable cloud runs. One difference however, is easy to deduce: The generation of eddy available potential energy (EAPE) depends upon the correlation of diabatic heating and temperature around a latitude circle, and its storage upon the variance of temperature. To the extent that the localized heat source effect of the fixed clouds increases

temperature differences around latitude circles, EAPE will be increased. This behavior is, in fact, borne out in the model results for the Northern Hemisphere (see Table 4). The changes in the other terms in the energy cycle are generally insignificant.

Table 4

N. HEMISPHERE

ENERGY CYCLE

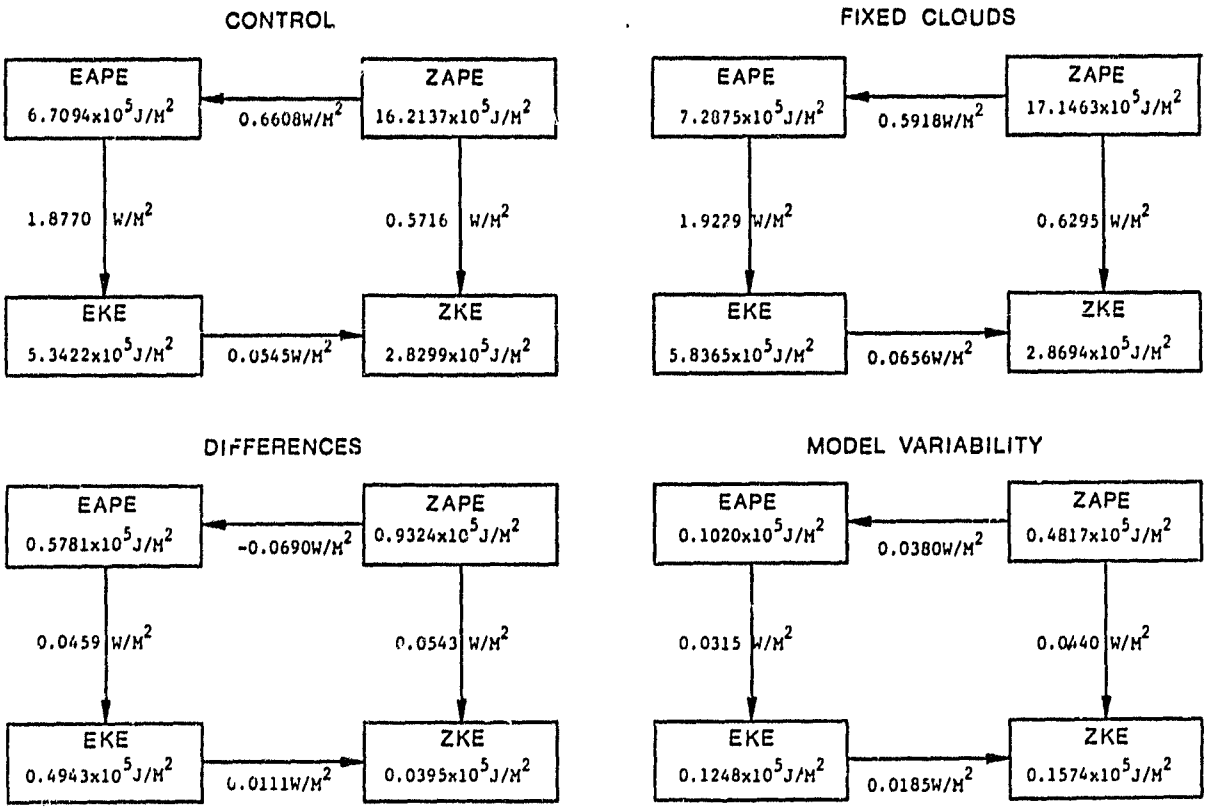

d. Dynamics of the Siberian High.

A chronic deficiency of many major GCM's, including the GLAS model, has been the inability to simulate accurately either the breadth or the intensity of the wintertime Asiatic high pressure regime. The Siberian high in nature is extensive, and covers a broad region of the Soviet Union from the Caspian Sea to northeastern Siberia. Mean monthly sea level pressures in the core of the anticyclone exceed 1032 mb, while daily station reports frequently exceed 1060 mb (Lydolf, 1977). The winterime Siberian high has been poorly

developed in recent versions of the GLAS GCM, with maximum sea level pressures of 1024 mb confined to a small region of northeast Siberia.

In view of the unrealistically high frequency of supersaturation clouds produced by the GCM over Siberia, and the resultant error that this feature has introduced into the model's radiation balance (see Section 4), it was reasonable to suspect that the failure of the high to develop may be due to a radiative mechanism.

A salient characteristic of the Siberian region is its extremely large radiative deficit at the surface and at the top of the atmosphere during the winter. The Siberian anticyclone owes its existence to this deficit in a number of ways: first, by maintaining local surface temperatures that are significantly colder than those in any of the surrounding regions (e.g., the central Arctic, Tibetian plateau, western USSR, or Sea of Okhotsk), a direct thermal circulation is established which results in large-scale subsidence and low-level divergence. Thus, through a mechanism analogous to that in Charney's desert-albedo feedback theory, a radiative deficit at the surface sustains itself by generating anticyclonic vorticity and inhibiting cloud formation. At the same time the extremely cold ground temperatures stabilize the planetary boundary layer, and minimize the turbulent exchange of momentum, heat, and moisture. Thus, convection and evaporation are suppressed, and, as postulated by Y. Mintz, so is frictional convergence and the generation of cyclonic vorticity through Ekman pumping mechanisms.

A possible way of illustrating these mechanisms might be:

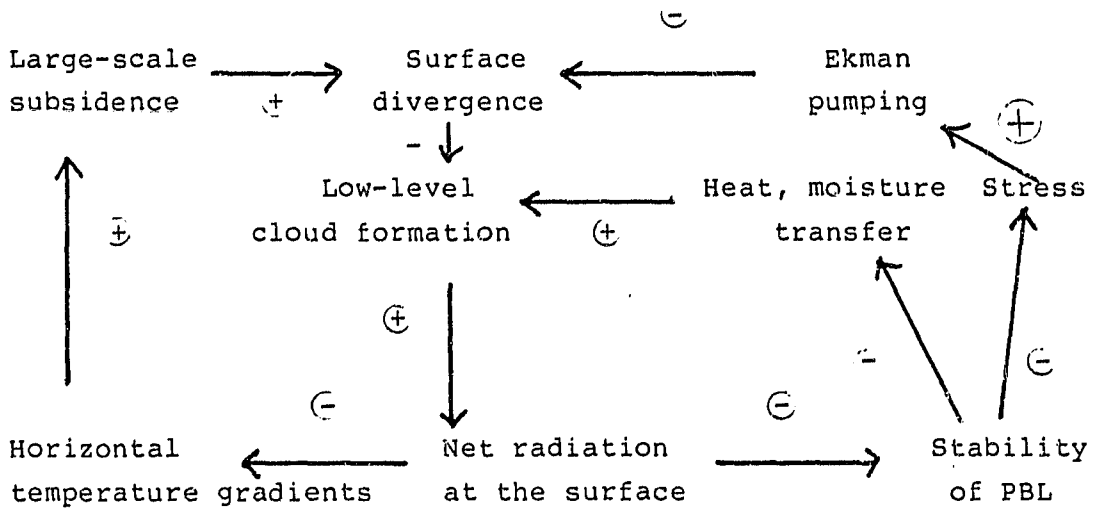

All of the feedback loops shown are stable, and suggest that the Siberian high is a self-perpetuating phenomena, mainly through the modes by which the radiative deficit at the surface limits low-level cloud formation, and perpetuates the excessive infrared loss.

It is thus possible to understand the GCM's problems over Siberia: If the clouds that form in the model are more opaque and more extensive than those in nature, then the surface radiation budget will be enhanced through the greenhouse effect, and anticyclogenesis will be inhibited. Similarly, if the PBL parameterization does not provide a sufficient damping of turbulence under stable conditions, then the generation of cyclonic vorticity will be favored, as will the heat and water vapor transfers. (We have, of course, excluded advection from this discussion, together with the influence of topography and finite differencing schemes on the cylonic vorticity advected into the Siberian region. Differences between sea level pressure reduction techniques used in the GCM and in the observations may also play a role).

The role of longwave radiation in the development of the high is clearly evident from the results of the transparent cloud experiments. In the control (Fig.14) only a weak region of high pressure forms near the Arctic coast, and low pressure from eastern Europe expands throughout Central Asia. In the simulation in which the model's clouds are transparent to thermal radiation, (Fig.15) the Siberian high is extensive and well-developed.

6. SUMMARY AND CONCLUSIONS

There are several implications regarding the problems of cloud effects and cloud feedback that follow from the results presented here.

First, the disposition of longwave radiation in this version of the GLAS model is unrealistic, and this is due principally to the problems of treating cloud fraction and variable cloud emissivity. The problem of determining a realistic distribution of cloudiness on the sub-grid scale clearly is substantial. At present it is not possible to prescribe the fractional distribution of cloudiness since there has been no comprehensive data based study that provides the distribution of cloud geometry and phase on scales required for

modeling studies. At the same time there is no satisfactory theory yet available for predicting fractional cloudiness from internally-generated model variables, although some encouragement can be drawn from the cumulus parameterizations being developed by Arakawa, Schubert and others.

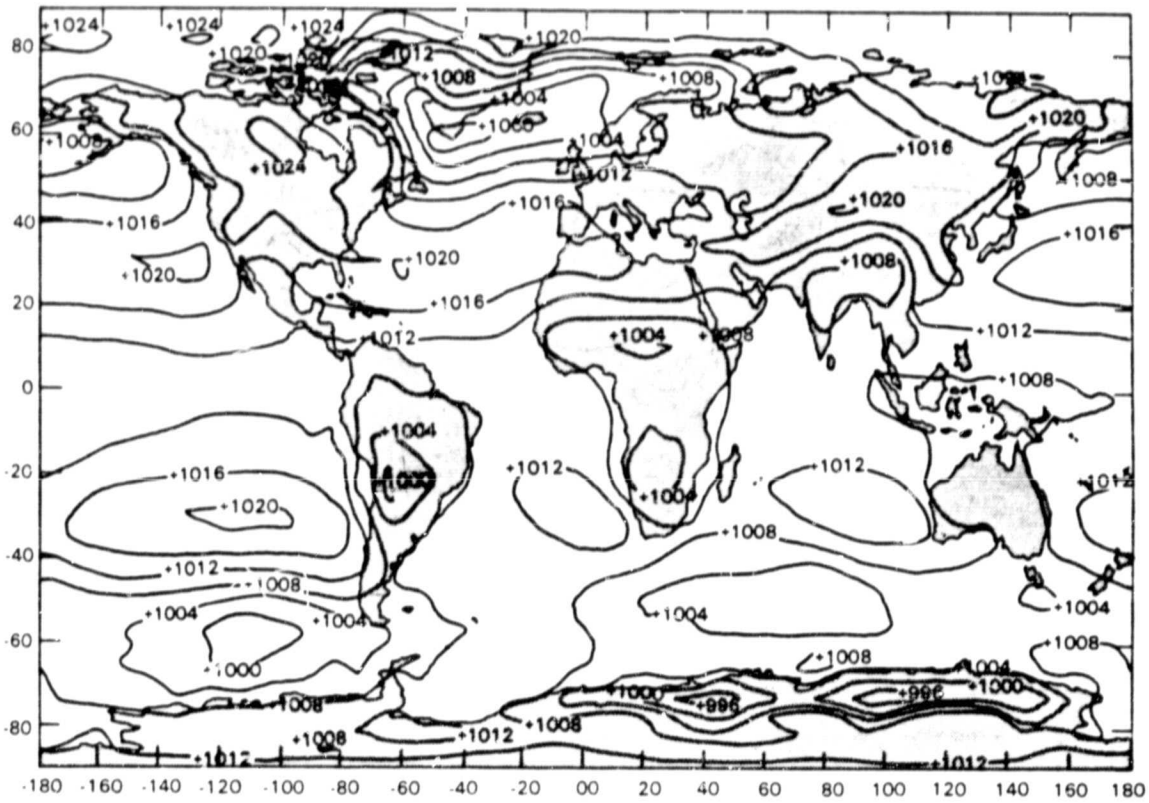

Figure 14. Sea level pressure (mb) for winter control.

The disposition of solar radiation is likewise as dependent on cloud fraction, cloud distribution and cloud optical properties. The calculation of solar absorption with currently available radiative transfer models is dependent to a critical degree on difficult-to-measure parameters such as single scatter albedo and particle phase function. It clearly is important that a hierarchy of carefully-controlled GCM experiments be conducted in order to demonstrate the sensitivity of the simulated climate to these uncertain parameters.

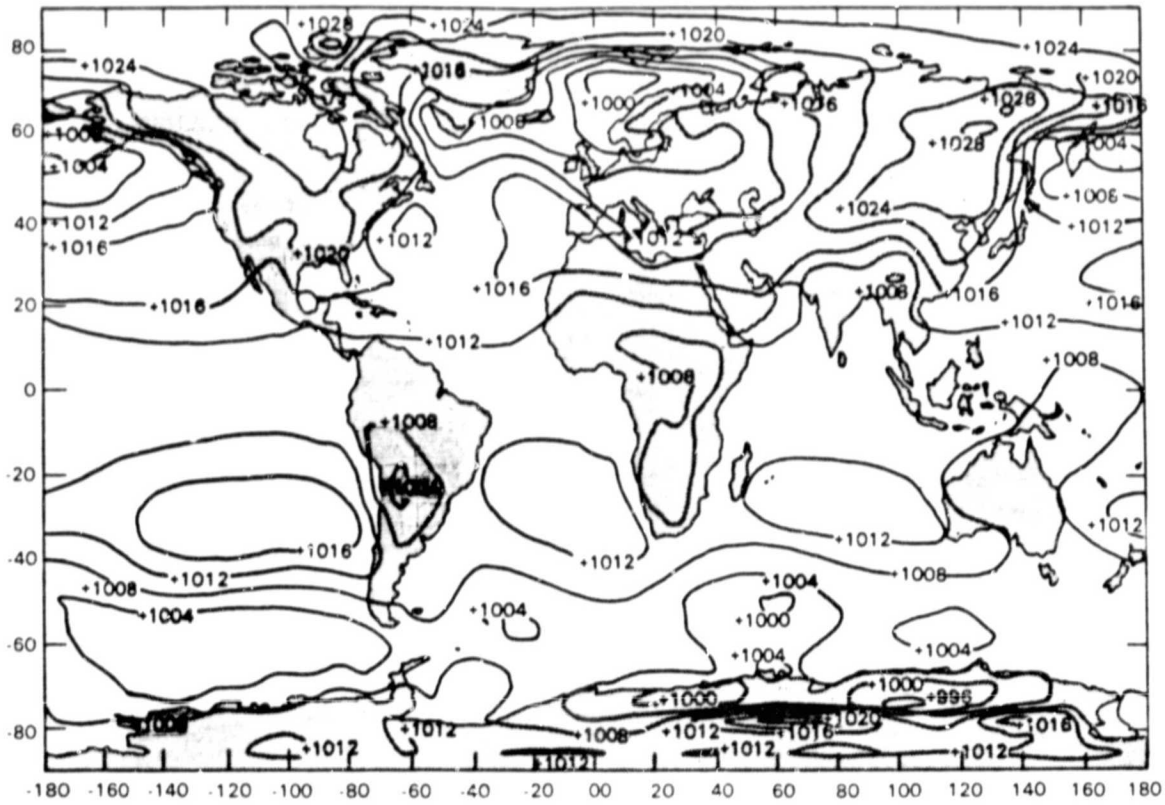

Figure 15. Same as Figure 15, except for clouds transparent to longwave radiation.

Several potential "feedbacks" between cloudiness and the general circulation have been illustrated. The question still remains, however, as to what constitutes a significant feedback. The systematic cloud frequency changes reported here were generally on the order of 5%, and these resulted from very large perturbations of the solar and infrared radiation budgets. While the changes are above the level of inherent model variability, the question still remains as to whether or not the resultant perturbations in the radiation field would result in significant changes in the atmospheric circulation. Some local features, such as the development of the Siberian high, clearly depend on the proper simulation of cloud feedback processes. On the other hand, Wetherald and Manabe (1980) suggest that the result of variable solar constant experiments were essentially independent of cloud feedback in the model. Clearly, a variety of well-planned GCM experiments needs to be conducted to elucidate these questions further.

7. ACKNOWLEDGEMENTS.

I am indebted to Dr. Halem and and the Staff of the GLAS Modeling and Simulation Facility for providing the support and resources for these analyses. Discussion with Drs. Y. Mintz, E. Kalnay-Rivas, and J. Shukla are gratefully acknowledged. Programming support was provided by W. Johnson and C. Long. Support for this research was provided by NASA grant NSG-5152 to the University of Wisconsin.

References

Berlyand, T. G. and L. A. Strokina, 1975: Seasonal cycle of tropospheric cloudiness, Trans. Voekova, Main Geophy. Obs., 338.

Berlyand, T. G. and L. A. Strokina, 1980: Global Distribution of a Cumulative Number of Clouds. Leningrad: Gidrometeoizdat.

Charney, J. G., and W. J. Quirk, S. H. Chow, and J. Kornfield, 1977: A comparative study of the effects of albedo change on drought in semiarid regions. J. Atmos. Sci., 34, 1366-1385.

Charney, J. G., 1975: Dynamics of deserts and droughts in the Sahel. Quart, J. R. Met. Soc., 101, 193-202.

Davies, R., 1980: Absorption of solar radiation in a general circulation model: The effect of solar zenith angle. Preprint Volume. Atm. Rad. Symp., Fort Collins.

Ellis, J. S., 1978: Cloudiness, the planetary radiation budget, and climate. Ph.D. Thesis, Colorado State University 129 pp.

Gates, W. L. and M. E. Schlesinger, 1977: Numerical simulation of the January and July global climate with a two-level atmospheric model. J. Atmos. Sci., 34, 36-76.

Halem, M., J. Shukla, Y. Mintz, M. L. Wu, R. Godbole, G. Herman, and Y. Sud, 1979: Comparison of observed seasonal climate features with a winter and summer numerical simulation produced with the GLAS general circulation model. World Meteorological Organization, GARP Publication Series, No. 22 pp 207-253.

Helfand, H. M., 1979: The effect of cumulus friction on the simulation of the January Hadley circulation by the GLAS model of the general circulation. J. Atmos. Sci., 36,. 1827-1843.

Herman, G. F. and W. T. Johnson, 1978: The sensitivity of the general circulation to Arctic sea ice boundaries. Mon. Wea. Rev., 106, 1649-1664.

Herman, G. F., M. L. Wu, and W. T. Johnson 1980: The effect of clouds on the earth's solar and infrared radiation budgets. J. Atmos. Sci., 37, 1251-1261.

Herman, G. F. and V. Krishnamurthy, 1981: Fractional cloudiness and variable cloud emissivity in the GLAS GCM. NASA GLAS Modeling and Simulation Facility, Annual Review.

Herman, G. F. and W. T. Johnson, 1980: Arctic and Antarctic climatology of the GLAS GCM. Monthly Weather Rev., 108, pp. 1974-1991.

Hunt, G. E., 1978: On the general circulation of the atmosphere without clouds. Quart, J. R. Met. Soc., 104, 91-102.

Lacis, A. A. and J. E. Hansen, 1974: A parameterization for the absorption of solar radiation in the earth's atmosphere. J. Atmos. Sci., 31, 118-133.

Lydolph, P. E., 1977: Climates of the Soviet Union. In: World Survey of Climatology, Vol. 7. New York: Elsevier, 443 pp.

Rodgers, C. D. and C. D. Walshaw, 1966: The computation of infrared cooling rate in planetary atmospheres. Quart J.R. Met. Soc., 92, 67-92.

Shukla, J. and V. Bangaru, 1979: Effect of a Pacific sea surface temperature anomaly on the circulation over North America: A numerical experiment with the GLAS model. WMO GARP Publication Series, 22, 501-518.

Shukla, J. and Y. Sud, 1980: Effect of cloud-radiation feedback on the climate of a general circulation model. Manuscript submitted to J. Atmos. Sci.

Somerville, R. C. J., P. H. Stone, M. Halem, J. E. Hansen, J. S. Hogan, L. M. Druyan, G. Russell, A. A. Lacis, W. J. Quirk, and J. Tennebaum, 1974: The GISS model of the global atmosphere. J. Atmos. Sci., 31, 84-117.

Stone, P. H., S. Chow, and W. J. Quirk, 1977: The July climate and a comparison of the January and July climates simulated by the GISS general circulation model. Mon. Wea. Rev., 105, 170-194.

Wetherald, R. T., and S. Manabe, 1980: Cloud cover and climate sensitivity J. Atmos. Sci., 37, 1485-1510.

Winston, J. S., A. Gruber, T. I. Gray, M. S. Varnadore, C. L. Earnest, L. P. Mannello, 1979: Earth-atmosphere radiation budget analyses derived from NOAA satellite data, June 1974-February, 1978. U. S. Dept. of Commerce, National Oceanic and Atmospheric Administration. Vols. I and II.

Wu, M. L., L. D. Kaplan, and R. Godbole, 1978: Influence of systematic radiation differences on the dynamics of a model atmosphere. Preprint Volume, Third Conf. on Atmospheric Radiation, Davis CA. pp. 293-302.

Wu, M. L., 1980: The exchange of infrared radiative energy in the troposphere. J. Geophys. Res., 85, 4084-4090.

Yamamoto, G., 1962: Direct absorption of solar radiation by atmospheric water vapor, carbon dioxide, and molecular oxygen. J. Atmos. Sci., 19, 182-188.

FRACTIONAL CLOUDINESS AND VARIABLE CLOUD EMISSIVITY IN THE GLAS GCM

(G. F. Herman and V. Krishnamurthy)

The recent analysis of cloud-radiation experiments conducted with the GLAS GCM (cf. Herman et al., 1980) clearly pointed to the fact that the average infrared opacity of the GLAS model atmosphere was too large. This is attributed to two factors: First, since all model clouds, including those which are intended to represent cirrus clouds in nature, are assumed to have unit emissivity (zero transmissivity), the model did not transmit enough long wave radiation to space. Secondly, all model clouds, including those intended to represent subgrid scale cumulus convection, were assumed in the radiation calculation to occupy the entire 4° latitude by 5° longitude grid area. The net result of both of these features of the radiation calculation was to maintain an excessively positive global radiation balance, and possibly have a detrimental effect on such dynamical processes as the formation of the Siberian anticyclone.

If the spectra of atmospheric absorbers, namely water vapor and cloud droplets, are uncorrelated (cf. Goody, 1964, p. 123), then a particularly simple treatment of both variable cloud emissivity and fractional cloudiness follows from the so-called multiplicative property.

Suppose that f is the fraction of a grid square that contains any cloud at any level, and also that f is constant with respect to height. Then the flux, $\overline{F_c}$, at any height, z, in this cloudy region is

$$F_c(z) = \overline{T}_c(0,z)\,\pi(B(0) - B_g) - \int_0^\infty \overline{T}_c(z,z')\,\pi\frac{dB(z')}{dz'}\,dz' \quad , \tag{1}$$

where T_c is the frequency-averaged transmittance that includes the presence of the cloud droplets, B is the Planck intensity, and B_g corresponds to the temperature of the ground.

For cloud-free regions of the atmosphere, the net flux due to gaseous absorption, F_g, is

$$F_g(z) = \overline{T}_g(0,z)\,\pi(B(0) - B_g) - \int_0^\infty \overline{T}_g(z,z')\,\pi\frac{dB(z')}{dz'}\,dz' \quad , \tag{2}$$

where the mean transmittance, $\overline{T}_g$, accounts only for gaseous absorption. We define the average flux, F, of the partially cloudy region as the weighted mean,

$$F = fF_c + (1-f)F_g \quad . \tag{3}$$

Then from (1) and (2)

$$F = \pi(B(0) - B_g)\,[f\bar{T}_c\,(0,z) + (1-f)\bar{T}_g(0,z)] - \int_0^\infty \pi\frac{dB(z')}{dz'}dz'\,[f\bar{T}_c(z,z') + (1-f)\bar{T}_g(z,z')] \quad . \tag{4}$$

The bracketed term $[f\bar{T}_c + (1-f)\bar{T}_g]$ represents the average transmittance of the partially cloudy regions.

Using the multiplicative property, the mean transmittance, $\bar{T}$, of the cloud-plus-gas mixture is

$$\bar{T}(z,z') = \bar{T}_g(z,z') \times \bar{T}_c(z,z') \quad . \tag{5}$$

The <u>effective</u> transmittance, $\bar{T}_e$, of the partially clouded region is thus

$$\bar{T}_e = \bar{T}_g(1-f+f\bar{T}_c) \quad . \tag{6}$$

Equation (4) becomes simply

$$F = \pi(B(0) - B_g)\bar{T}_e - \int_0^\infty dB(z')\,\bar{T}_e(z,z') \quad . \tag{7}$$

Equation (7), as derived, applies only to the situation where cloud fraction does not vary with height. However, it is readily generalized to account for cloud fractions that may vary from layer to layer.

The transmittance of the cloud may thus be adjusted directly in the term $\bar{T}_c$. Note that the cloud fraction and cloud transmissivity occur as a product; the average opacity of the atmosphere may be adjusted by alternatively varying the cloud fraction or the cloud emissivity.

Table 1 illustrates the effect that variable cloud fraction and cloud transmissivity have on fluxes and cooling rates. Here f denotes the fractions of a grid square that contains any cloud, and T_c the cloud transmissivity. Thus, f=0 corresponds to a completely clear grid, while f=1.0 corresponds to a complete overcast. Similarly $\bar{T}_c$=0 corresponds to a completely transparent cloud, while $\bar{T}_c$=1.0 denotes a cloud that is perfectly opaque. For illustration it is assumed that a single cloud layer is found in layer 5. The effect of the cloud on the fluxes is shown in upper section of Table 1. As the average opacity increases due to either increasing the fraction or decreasing the transmittance, the net flux beneath the cloud layer decreases monotonically, which is due to the enhanced downward flux. The flux <u>above</u>

the cloud layer also diminishes with increasing opacity because the upward radiation is less intense, having originated at comparably colder temperatures.

The effect on cooling rates is illustrated in the lower section of Table 1. Cooling below the cloud is smaller as the opacity increases because of the decreased importance of cooling to space. Cooling at and above the cloud increases with increasing opacity. These dependencies are illustrated in Fig. 1.

When introduced to the GLAS GCM, the cloud fraction, f, will likely be a parameter to which the model's radiation and dynamics are very sensitive. Clearly, a major problem will be in determining the most realistic value of this parameter.

Reference

Goody, R. M., 1964: Atmospheric Radiation. Oxford University Press.

Herman, G. F., M. L. Wu, and W. T. Johnson, 1980: The effect of clouds on the earth's solar and infrared radiation budgets. To appear in J. Atmos. Sci.

Table 1. Clouds in layer 5. Latitude = 46°, Day = 1 February.

Level	Pressure (mb)	Flux(W m^{-2})				
		Cloudless $f=0.0, \overline{T}_c=1.0$	$f=0.25, \overline{T}_c=0.0$ or $f=1.0, \overline{T}_c=0.75$	$f=0.5, \overline{T}_c=0.0$ or $f=1.0, \overline{T}_c=0.5$	$f=0.75, \overline{T}_c=0.0$ or $f_c=1.0, \overline{T}_c=0.25$	$f=1.0$ $\overline{T}_c=0.0$
1	10	211	195	179	164	148
2	120	205	189	173	157	141
3	230	197	181	164	148	131
4	340	187	170	153	136	119
5	450	170	152	134	116	98
6	560	151	126	100	75	49
7	670	134	113	92	72	51
8	780	118	101	83	66	48
9	890	104	89	74	59	44
10	1000	90	77	64	51	39

Layer	Pressure at Center of Layer (mb)	Cooling Rate (°C/Day)				
		Cloudless $f=0.0, \overline{T}_c=1.0$	$f=0.25, \overline{T}_c=0.0$ or $f=1.0, \overline{T}_c=0.75$	$f=0.5, \overline{T}_c=0.0$ or $f=1.0, \overline{T}_c=0.5$	$f=0.75, \overline{T}_c=0.0$ or $f=1.0, \overline{T}_c=0.25$	$f=1.0$ $\overline{T}_c=0.0$
1	65	0.4	0.5	0.5	0.5	0.6
2	175	0.6	0.6	0.7	0.7	0.7
3	285	0.8	0.9	0.9	0.9	0.9
4	395	1.3	1.4	1.4	1.5	1.6
5	505	1.4	2.0	2.6	3.2	3.8
6	615	1.3	1.0	0.6	0.2	-0.2
7	725	1.2	1.0	0.7	0.5	0.2
8	835	1.1	0.9	0.7	0.5	0.3
9	945	1.1	0.9	0.8	0.6	0.4

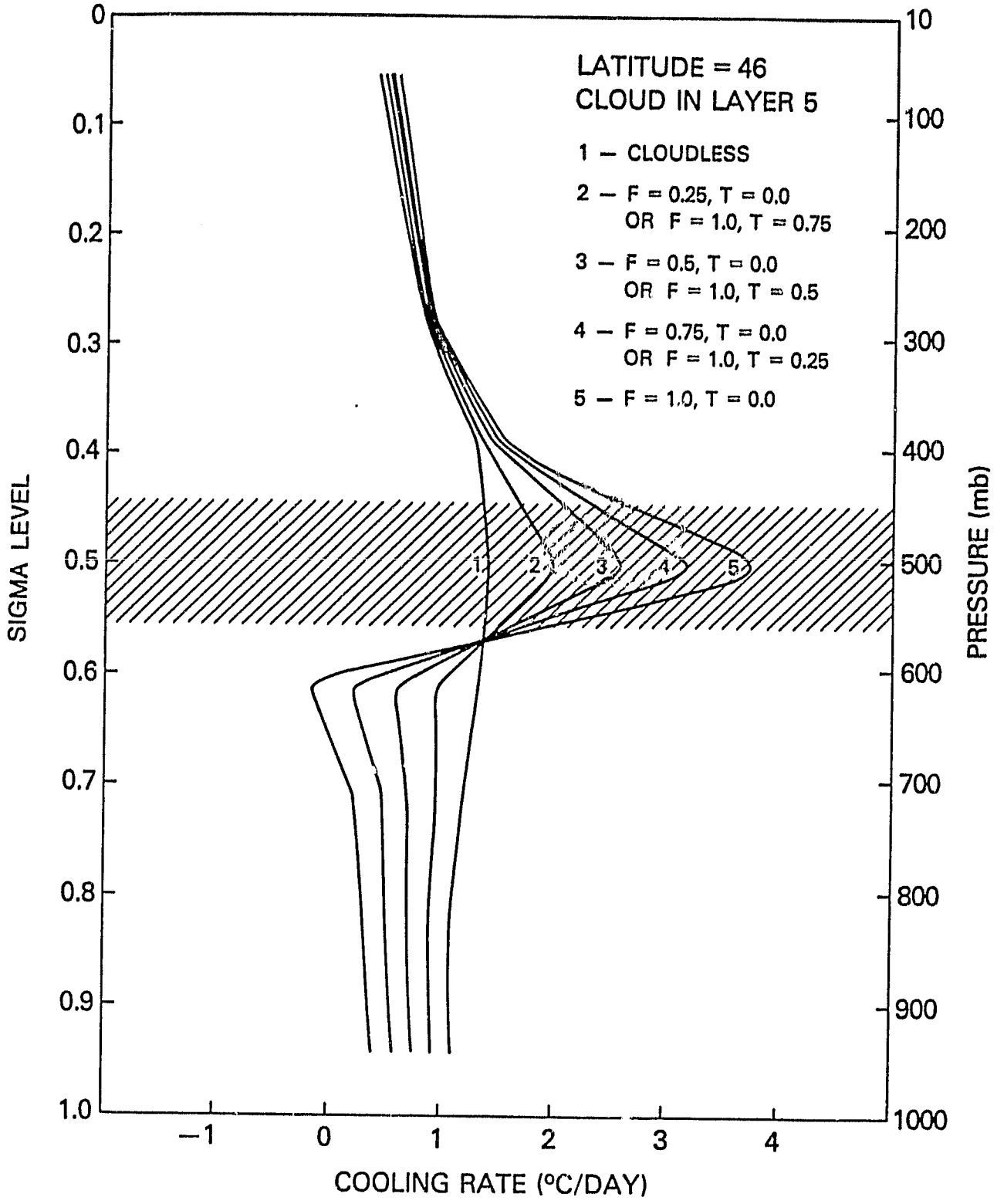
LATITUDE = 46
CLOUD IN LAYER 5
1 — CLOUDLESS
2 — F = 0.25, T = 0.0
OR F = 1.0, T = 0.75
3 — F = 0.5, T = 0.0
OR F = 1.0, T = 0.5
4 — F = 0.75, T = 0.0
OR F = 1.0, T = 0.25
5 — F = 1.0, T = 0.0
SIGMA LEVEL
PRESSURE (mb)
COOLING RATE (°C/DAY)
0
0.1
0.2
0.3
0.4
0.5
0.6
0.7
0.8
0.9
1.0
10
100
200
300
400
500
600
700
800
900
1000
−1
0
1
2
3
4

Fig. 1.